New features in solution derived $La_{0.7}Sr_{0.3}MnO_3$ thin films : spontaneous outcropping and nanoscale reversible resistive switching

Dissertation presented in candidacy for the degree of Doctorate of Philosophy in Material Science by

César Moreno Sierra

Departament de Física, Facultat de Ciències
Universitat Autònoma de Barcelona

Supervisors: *Prof. X. Obradors i Prof. C. Ocal*

Tutor: *Prof. Alvar Sanchez*

January 15, 2010

Carmen Ocal Garcia i **Xavier Obradors i Berenguer**, ambdós investigadors del CSIC a l'Institut de Ciència de Materials de Barcelona,

CERTIFIQUEN

Que **César Moreno Sierra**, llicenciat en Ciències Físiques, ha dut a terme sota la nostra direcció el treball que porta per títol *"New features in solution derived $La_{0.7}Sr_{0.3}MnO_3$ thin films : spontaneous outcropping and nanoscale reversible resistive switching"*, i queda recollit en aquesta memòria per optar al grau de Doctor en Ciència de Materials.

I perquè així consti, signen el present certificat.

Prof. Carmen Ocal Garcia **Prof. Xavier Obradors i Berenguer**

Bellaterra, ... de .... de ....

A mis padres, a mis hermanos, a Zaira

Abstract

This dissertation describes the basic structural, electronic transport and magnetic properties of epitaxial $La_{0.7}Sr_{0.3}MnO_3$ (LSMO) thin films on single crystalline substrates grown by chemical solution deposition. In addition, new features such as spontaneous outcropping of insulating nanodots on the LSMO surface and nanoscale reversible resistive switching have also been addressed.

The thesis is organized in the following way: first, a short introduction to manganites is given. In the second chapter, a study of the new mechanism for the creation of self-assembled insulating epitaxial nanostructures in a LSMO film surface is presented. These two crystalline phases, LSMO thin film and insulating nanodots, are investigated by transmission electron microscopy (TEM), displaying a coherently strained structure, even though the strain state and the lattice symmetry of the LSMO film underneath the islands have been modified. Insulating islands induce an isotropic strain to the LSMO film underneath the island which decreases the magnetoelastic contribution to the magnetic anisotropy. It is shown that the size and concentration of the nanodots can be tuned by means of growth kinetics and through modification of the La excess in the precursor chemical solution. Furthermore, nanoscale electrical analysis was performed by C-SFM in order to determine the insulating behavior of the nanodots.

In the third chapter, we report our efforts to give some insight into the role that interfacial strain generation and interfacial strain accommodation play on the thin film properties. On this account, the dependence of the LSMO films magnetoelectronic properties on the film thickness is scrutinized. The changes of the magnetoelectronic properties have been examined assuming a magnetoelastic model and we found that these changes on magnetoelectronic properties cannot be explained merely by the film strain state. Instead, the Curie and metal to insulator transition temperatures are also influenced by other factors, such as chemical inhomogeneities and structural disorder in the film.

In the fourth chapter, in order to elucidate the intrinsic or extrinsic origin of the Joule heating effect in the resistance bistability of LSMO thin films we accomplish a detailed study of the heating sources. We report macroscopic transport measurements and local electrical behavior at the nanoscale, obtained by conducting Scanning Force Microscopy (C-SFM). We have demonstrated that, under adequate measuring conditions, a regime of bistable resistivity in LSMO thin films is not achieved at $T = 300$ K. We otherwise suggest that this phenomenon would only occur in LSMO films when measuring at temperatures below $T \backsim 250$ K.

In the fifth chapter, a new stable resistive switching based methodology capable to program,

store and read out multiple levels in a nanoscale regions were performed modifying the intrinsic properties of the LSMO film. We demonstrate that the number of distinguishable resistance levels can readily reach 10 and even higher. We overcome the main handicaps of resistive random-access memory (RRAM) approaches, except for unclear driven mechanism of resistive switching, namely scalability, low cost, high area density of storage data and spatial uniformity of resistive switching process.

The experimental techniques and procedures used in this thesis are summarized in chapter 7. The growth technique of epitaxial thin film, chemical solution deposition, and the synthesis of samples are described. Also different chemical characterization, structural, electronic transport and magnetic techniques are presented. In addition, the optical lithography process employed for electronic transport measurements is explained in this chapter.

Resumen

Esta disertación describe las propiedades estructurales, de transporte electrónico y magnéticas básicas de películas delgadas de $La_{0.7}Sr_{0.3}MnO_3$ (LSMO) crecidas por depósito de soluciones químicas en substratos monocristalinos. Además, nuevas características, tales como, el afloramiento espontáneo de puntos nanométricos aislantes en la superficie de la película de LSMO e interruptores resistivos reversibles a la nano escala han sido abordados.

Esta tesis está organizada del siguiente modo: primero, se da una breve introducción sobre manganitas. En el segundo capítulo, el estudio de un nuevo mecanismo para generar estructuras aislantes y nanométricas auto-ensambladas en la superficie de la película de LSMO es presentado. Estas dos fases cristalinas, la película delgada de LSMO y los puntos aislantes, son investigados por microscopía electrónica de transmisión (TEM), mostrando una estructura coherentemente tensionada, si bien el estado de tensión y la simetría de la red de la capa de LSMO debajo de los puntos ha sido modificada. Estas islas aislantes provocan una tensión isotrópica a la película debajo de las mismas, lo cual, hace disminuir la contribución magneto-elástica en la anisotropía magnética. Se muestra que el tamaño y la concentración de las islas puede ser modificado a través de la cinética del crecimiento y modificando la cantidad de exceso de La en la solución precursora inicial.

En el tercer capítulo, se intenta poner en evidencia el papel que juega la generación de tensión en las interficies así como su acomodación cuando se cambian las propiedades de la película delgada. Por este motivo, la dependencia de la propiedades de magneto transporte han sido analizadas. Los cambios de estas propiedades han sido examinados en el marco de un modelo magneto elástico, encontrando que dichos cambios no pueden ser justificados solamente con el estado de tensión. Sino que, la temperatura de transición de Curie y metal-aislante están influenciadas por otros factores como pueden ser inhomogeneidades químicas y desorden estructural presente en la película delgada.

En el cuarto capitulo, con el fin de dilucidar el origen del calentamiento debido a efecto Joule, si se trata de un efecto intrínseco o extrínseco, en la biestabilidad resistiva de las películas delgadas de LSMO hemos llevado a cabo un estudio detallado del origen de este calentamiento. Presentamos medidas del transporte electrónico macroscópicas y locales obtenidas con un microscopio de sonda local en modo detección de corriente (C-SFM). Demostramos que, bajo adecuadas condiciones de medida, el régimen de resistencia biestable no puede ser conseguido a una temperatura de 300K. Además, sugerimos que este fenómeno sólo podría ser alcanzado en películas delgadas de LSMO a temperaturas entorno a 250K.

En el quinto capítulo, una nueva metodología basada en la generación de estados resistivos estables, capaz de programar, almacenar y leer múltiples niveles de información en regiones nanométricas fue llevada a cabo modificando las propiedades resistivas intrínsecas de las películas delgadas de LSMO. Demostramos que el número de estos diferentes niveles puede llegar al menos a 10 pudiendo ser incluso mayor. Con este concepto de memoria resolvemos algunos de los principales escollos de la memorias resistivas de acceso aleatorio (RRAM), salvo en el conocimiento del mecanismo que gobierna, como son la escalabilidad, el bajo coste de producción, una alta densidad de almacenaje de datos y la uniformidad espacial del interruptor resistivo.

Las técnicas y procedimientos experimentales usados en esta tesis son presentados en el capítulo 7. Tanto la técnica de crecimiento de las películas epitaxiales, depósito de soluciones químicas, como la síntesis de las muestras es descrita. También se explican las diferentes técnicas utilizadas para la caracterización química, estructural, de transporte eléctrico y propiedades magnéticas. Además, el proceso de litografía óptica empleado para las medidas de transporte electrónico se explica en este capítulo.

Motivation

Materials science has been at the frontier of technological development since the bronze and iron ages. The ability to fabricate functional structures and performing devices in different materials is central to the production of microelectronic devices, data-storage systems, and many other basic products of the actual society.

Within the class of inorganic materials, oxides display perhaps the most diverse range of properties. Oxides exhibit the full spectrum of electronic and magnetic behavior: insulating, semiconducting, metallic, superconducting, ferroelectric, piezoelectric, ferromagnetic and multiferroic effects. In the case of manganese oxides, electronic transport and magnetic properties and crystal lattice can be controlled by utilizing the interaction between charge, orbital, spin, and lattice degrees of freedom that cause drastic changes in these properties. These compounds are thus part of the strongly correlated electron systems. The strong coupling between the electrons and the lattice brings about that a small change in the chemical composition, can induce large changes in the physical properties. A similar change can occur due to external effects, such as a magnetic or electric field, a hydrostatic pressure, irradiation effects or the temperature. The most immediate excitement with manganites could be their ability to display electrically controlled memory effects for resistive random-access memory (RRAM). Among of manganite family compounds, with a high Curie temperature T_c of 370 K and with almost 100% spin polarization, $La_{0.7}Sr_{0.3}MnO_3$ manganite appears an attractive material for applications at room temperature and it is also considered as one of the most prototypical compounds.

Owing to the dependence of these properties on crystal structure , it is often optimal to grow epitaxial oxides. While polycrystalline oxide films may have sufficient properties for some applications and studies, the superior properties of highly crystalline epitaxial films are most attractive both for applications and fundamental studies of material and surface properties. In this concern, among the different deposition techniques, chemical solution deposition method is considered to be one of the most promising approaches for cost-effective production of thin films.

For the commented reasons above, the study and the properties control of epitaxial $La_{0.7}Sr_{0.3}$-MnO_3 thin films grown by chemical deposition methods are very interesting both from an applied and from a fundamental point of view.

Contents

List of Figures

List of Tables

Symbols and Abbreviations

2D	Two-dimensional
3D	Three-dimensional
CCD camera	Charge-coupled device camera
CSD	Chemical solution deposition
DRAM	Dynamic random-access memory
EDS	Energy dispersive X-ray Spectroscopy
EDX	Energy dispersive X-ray analysis
EELS	Electron energy loss analysis
EFTEM	Energy filtering transmission electron microscopy
FFT	fast Fourier transform
FM	Ferromagnetic-metallic
FWHM	Full width at half maximum
HREM	High-resolution electron microscope
ICP	Inductively coupled plasma
MBE	Molecular beam epitaxy
MFM	Magnetic force microscopy
MOCVD	Metallorganic chemical vapour deposition
MR	Magnetorresistencia
MRAM	Magnetic random access memory
PLD	Pulsed laser deposition
RAM	Random-Access Memory
RMS	Root mean square
rpm	Revoluciones per minute
RRAM	Resistive random access memory
RSM	Reciprocal space map
SAED	Selected area electron diffraction
SEM	Scanning electron microscopy
SFM	Scanning force microscopy
STM	Scanning tunneling microscopy
STO	Strontium titanate, $SrTiO_3$
TEM	Transmission electron microscopy

TOF-SIMS	Time-of-flight secondary ion mass spectrometry
UV	Ultraviolet
XRD	X-ray diffraction

Chapter 1

Lanthanum manganites background

This introductory chapter explains the historical and fundamental background of the manganites concerned with the present thesis. More specific introductions on the topic covered in each chapter of the thesis will be given throughout the corresponding chapters.

1.1 Introduction

The term manganites refers to a whole range of perovskite manganese oxide compounds of the generic formula $A_{1-x}B_xMnO_3$ where A and B can be a trivalent or divalent element, mostly rare earth (e.g., La, Nd, Pr, Sm) or alkaline earth (e.g, Sr, Ca, Ba, Pb)[*]. The doping parameter x is equal to the density of carriers. Originally, the interest in manganites stemmed from the discovery of their ferromagnetism and its correlation with electrical conductivity by *Jonker and van Santen*[89].

In order to account for the simultaneous appearance of ferromagnetism and metallicity in the mixed-valence manganites, *Zener*[184] first proposed the double-exchange mechanism. It consists of an electron hopping from Mn^{3+} to a neighbouring oxygen and simultaneously a second electron hopping from the oxygen to a neighbouring Mn^{4+}. The model was developed later by *Anderson and Hasegawa*[5] and then extended by *de Gennes*[43].

These models allowed for the understanding of many of the properties of manganites at the time and the interest in these materials subsided as they were thought to be completely understood. But the discovery of a magnetoresistance effect in manganites[174], epitomized by *Jin et al.* as the "colossal magnetorresistance" (CMR) (observed in the vicinity of the Curie temperature (T_c) as well as the

---

[*] Depending on the special context, one also finds the terms *rare-earth manganites, CMR manganites, or mixed-valence manganites.*

metal-insulator transition temperature) associated with metal-insulator transition and granular magnetoresistance in the 1990's[78,86], sparked a renewed interest in these compounds for their potential technological applications and for the fundamental theoretical questions they gave rise to.

1.2 Crystal structure

$\chi\phi_1$ τ σ $\rho\pi_3$ has a perovskite structure with a rhombohedral distortion. In the pseudocubic description, the unit cell angle and the lattice parameter of LSMO are $90\,26$ and $3\,873\nu$ [102] respectively. Because of this small deviation from the cubic symmetry, it is convenient to adopt the pseudocubic notation for crystallographic planes. In figure 1.1, pseudocubic crystal structures of two unit cells of perovskites, $\tau\mu\lambda\pi_3$ and $\chi\phi_1$ τ σ $\rho\pi_3$, are shown.

In LSMO, the large sized $\chi\phi^{3+}$ trivalent ions and τ^{2+} divalent ions occupy the A-site with 12-fold oxygen coordination. The smaller σ ρ-ions in the mixed-valence state σ ρ^{3+} σ ρ^{4+} are located at the centre of an oxygen octahedron, the B-site with 6-fold coordination. For the stoichiometric oxide, the proportions of σ ρ ions in the valence states (3+) and (4+) are, respectively (1) and ( ).

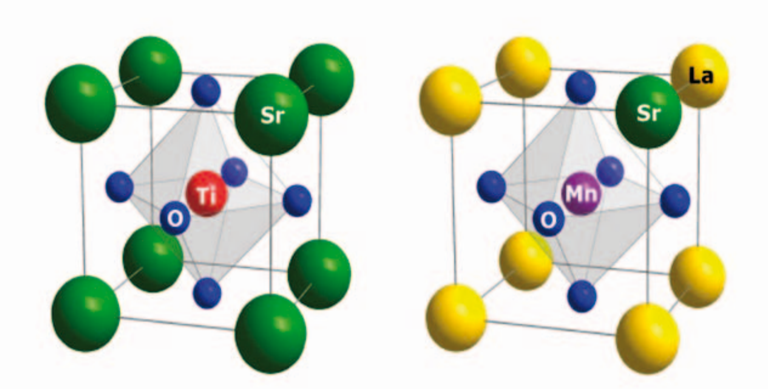

Fig. 1.1: *Schematic crystal structure of the perovskite unit cell for* $\tau\mu\lambda\pi_3$ *(STO) and* $\chi\phi_1$ τ σ $\rho\pi_3$ *(LSMO). Sr or La/Sr, and Ti or Mn occupy the A- and B-sites, respectively. The unit cell contains a Mn(Ti)-ion surrounded by an oxygen octahedron and bounded in a simple cubic structure of A-site elements.*

STO is a cubic perovskite that has a parameter $\phi \quad = 3\,905\nu$, larger than that of LSMO by $0\,83\%$. If the STO substrate is (001) oriented, then the STO and LSMO perovskite unit cells have the following correspondences: the octahedral site receives μ λ in STO and σ ρ in LSMO, while the other cation site receives τ in the former and $\chi\phi_1$ τ in the latter.

The eponymous mineral $_3$ is named after a village in Russia.

Films of LSMO grow epitaxially [‡] with (001) orientation on (001) oriented STO substrates due to the cubic symmetry and constraints imposed by epitaxy. However, the small lattice mismatch between the LSMO film and these substrates cannot be released easily and built-in stresses that might produce effects on transport and magnetic properties.

To understand the relationship between structural and electrical properties of manganite films, *Hwang et al.*[79] investigated structural-electrical correlation of CMR manganite films using T_c and the Goldschmidt tolerance factor (TF) given by:

$$TF = \frac{d_{(A_{0.7}A'_{0.3})-O}}{\sqrt{2}d_{Mn-O}} \tag{1.1}$$

where $d_{(A_{0.7}A'_{0.3})-O}$ is the distance between A site ($A_{0.7}A'_{0.3}$) and oxygen (O) ions and d_{Mn-O} is the distance between Mn and O ions. The Curie temperature (T_c) is maximum around $x = 0.3$ (Fig.1.2) and for $< r_A > \approx 1.24\mathring{A}$ which is for $La_{0.7}Sr_{0.3}MnO_3$. The reduction of $< r_A >$ from this optimum value leads to an increase in distortion of the crystallographic structure which weakens the ferromagnetic double exchange and increases the tendency to localize the charge carriers[79].

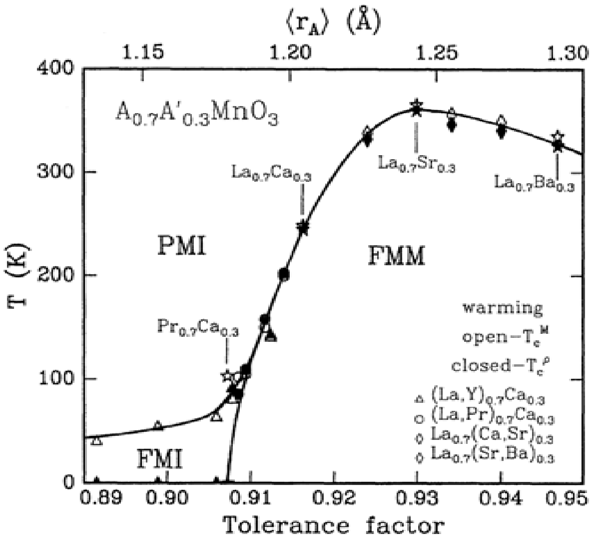

Fig. 1.2: *Phase diagram of temperature versus tolerance factor for* $A_{0.7}A'_{0.3}MnO_3$ *(after*[79]*).*

Similar conclusions are reached by *Maignan et al.*[101] and *Fontcuberta et al*[51]. They report that changes of the lattice constant and thus the one-electron bandwidth, by varying the radius of the A

[‡] The term "epitaxy" describe the phenomenon of the oriented growth of crystals of one substance on the crystal surface of another substance. The term has been generalized to thin crystalline films grown in a well-defined orientation on a single crystal substrate. The term epitaxy comes from the Greek roots *epi*, meaning "above", and *taxis*, meaning "in ordered manner".

cation, τ , in ν π_3 formula, the metal to insulator transition temperature can be controlled. They conclude that the narrowing of the electronic bandwidth is the fundamental parameter controlling the observed CMR.

1.3 Electronic structure and magnetic exchange

The physics of manganites is mainly determined by the mixed valency of the manganese ions. A first valuable step in understanding the mixed-valence manganites is to imagine a simple ionic scheme as depicted in figure 1.3. σ ρ^{2+}, σ ρ^{3+}, and σ ρ^{4+} valence states, which can all occur in manganites depending on the composition, have 5, 4, or 3 electrons in the 3d shell, all with parallel spins according to Hund's first rule.

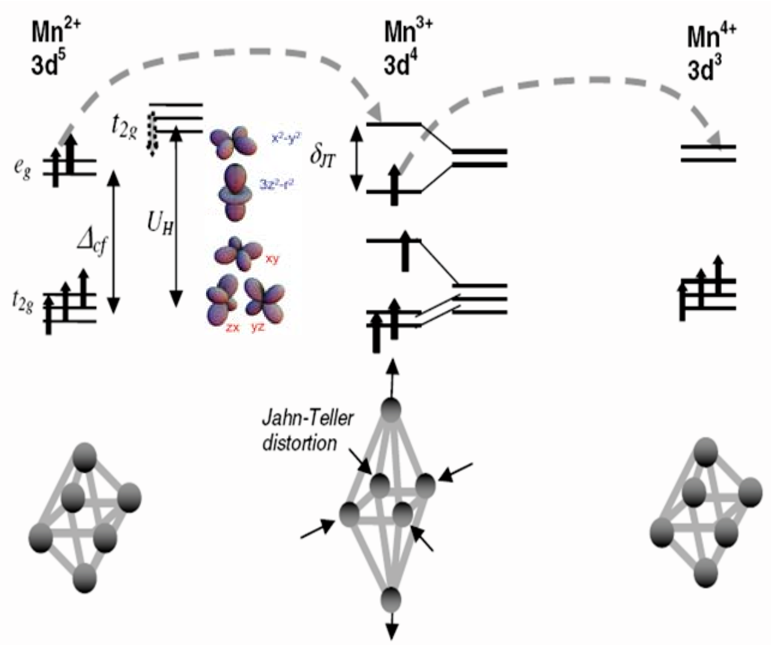

Fig. 1.3: *Scheme of 3d electronic states and orbitals in σ ρ^{2+}, σ ρ^{3+} and σ ρ^{4+} ions in perovskite manganites in octahedral coordination. The effect of a tetragonal distortion is lowering the energy of σ ρ^{3+} by θ , while the others remain unchanged. Abbreviations denote octahedral crystal field splitting, Hund's rule onsite coupling energy, θ Jahn-Teller splitting energy resulting from distortion of the oxygen octahedron. Large dashed arrows indicate spin-conservative electron transfer between Mn ions which proceeds via intermediate O 2p orbitals. (Adapted from Dörr[47]).*

In the cubic environment of the octahedron, hybridisation and electrostatic interaction of the manganese with oxygen ϵ electrons will create a crystal field for the outer 3 electrons in σ ρ^{3+}. This field lifts the 5-fold degeneracy of electrons present in free σ ρ^{3+} ions by splitting the energy levels and forming lower lying triply degenerate t_{2g} states and a higher doublet of e_g states, as shown in figure 1.3. The t_{2g} triplet consists of the d_{xy}, d_{xz} and d_{yz}-orbitals, while the e_g doublet contains the $d_{x^2-y^2}$ and $d_{3z^2-r^2}$ orbitals. The filling of these levels follows Hund's first rule where parallel spins are energetically favorable due to minimisation of Coulomb repulsion energy. The minority (antiparallel) spin levels are very high in energy. This implies that only majority spins conduct. For this reason, manganites are called half-metallic ferromagnet. This is illustrated in Fig.1.4 where the electron levels are sketched in the vicinity of the Fermi level E_F.

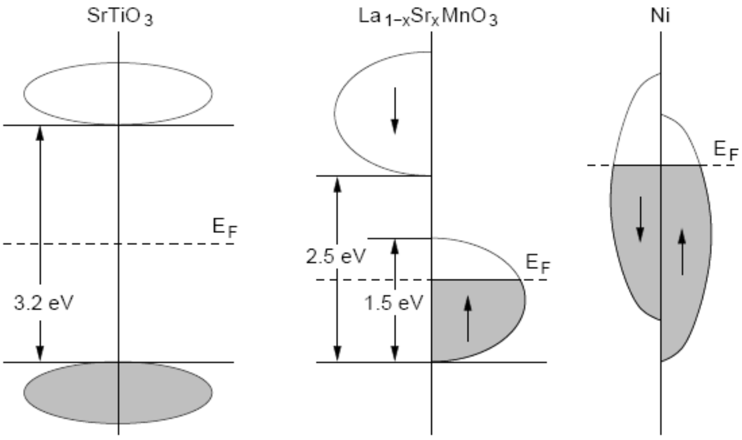

Fig. 1.4: *Schematic of the electronic band structures of* $SrTiO_3$ *(left),* $La_{1-x}Sr_xMnO_3$ *(middle) and, for comparison, Ni (right). Dark bands are filled, white bands empty,* E_F *denotes the Fermi energy, and the arrows indicate the electron spins. STO is a band gap insulator. LSMO is a half-metallic ferromagnet*[122] *where one electron spin (here up) shows metallic and the other (down) insulating behavior in coexistence. Ni, on the other hand, is a conventional ferromagnetic metal with simultaneously occupied up and down spin states.*

The divalent ion Mn^{2+} has a very stable $3d^5$ configuration, a half-filled shell $t_{2g}^{3\uparrow}e_g^{2\uparrow}$ with $S = \frac{5}{2}$ and a spherically symmetric electron density. Trivalent manganese is $3d^4$, $t_{2g}^{3\uparrow}e_g^{\uparrow}$ with $S = 2$, whereas quadrivalent manganese is $3d^3$, $t_{2g}^{3\uparrow}$ with $S = \frac{3}{2}$. The spin-only moments of these ions are $5\mu_B$, $4\mu_B$ and $3\mu_B$, where μ_B is the Bohr magneton, respectively.

For the particular case of $La_{1-x}Sr_xMnO_3$, the Mn site has a mixed valence state of x Mn^{4+} (holes) and $(1-x)$ Mn^{3+}. For $x < 0.5$ carriers are holes while for $x > 0.5$ the carriers are electrons with concentration $1-x$. The ferromagnetic phase is stabilized by the double exchange mechanism[184], in which two simultaneous electron hopping processes are assumed. One electron is transferred from Mn^{3+} to a neighbouring oxygen $2p$ orbital, and a second electron from this oxygen $2p$ orbital to an adjacent Mn^{4+} ion, with the initial and final states being degenerate and consequently coexisting and coupling the Mn spins ferromagnetically. In general one could say that double exchange means the magnetic interaction mediated by itinerant spin-polarized d electrons which couple to the localized core moments according to Hund's rule.

The above explanations provide a phenomenological understanding of the ferromagnetic and conductive ground state, but the origin of the magnetoresistance effect needs further considerations. In a semiclassical approach the double-exchange model yields a certain relation between the electron transfer probability between the two Mn ions and the angle Θ between their magnetic moments. The transfer probability is proportional to $cos(\Theta/2)$. If an external magnetic field is strong enough to align the Mn moments parallel to each other ($\Theta = 0^o$), the transfer probability becomes unity and the resistance drops dramatically. The magnitude of the MR[§] is usually defined as:

$$MR = \frac{\rho(0) - \rho(H)}{\rho(0)} \tag{1.2}$$

where $\rho(0)$ and $\rho(H)$ designate resistance in the zero field and in the applied field, respectively. In normal ferromagnetic materials the magnetoresistance effect is just a few percent. But the manganese perovskites have shown magnetoresistance values close to 100% in magnetic fields of a few Teslas. This colossal magnetoresistance is generally observed close to the Curie temperature.

The physics of the CMR in the manganites is obviously more complex. Many important factors other than the above simple double-exchange scenario, such as electron-lattice interaction, antiferromagnetic superexchange interaction between the t_{2g} local spins, intersite exchange interaction between the e_g orbitals, intrasite and intersite Coulomb repulsion interactions among the e_g electrons, etc., are necessary to interpret important experimental results.

1.4 Phase diagram

Phase diagrams of the mixed valence perovskite manganites are rich in different magnetic, transport as well as structural phases. The phase diagram of manganite $La_{1-x}Sr_xMnO_3$ is depicted in Fig.1.5 where it can be seen that it has an anti-ferromagnetic and insulating behavior at high and low doping concentration (x) values and a ferromagnetic metallic behavior in a certain range of concentrations centered around $x \approx 0.33$ with highest curie temperature ($T_c = 370K$)[166]. This is the reason why it is considered as a good candidate for room temperature applications.

[§] Different definitions of the magnetorresistance ratio appear in the literature, including $[\rho(0) - \rho(H)]/\rho(0)$, $\rho(H) - \rho(0)]/\rho(H)$ and $\rho(0)/\rho(H)$.

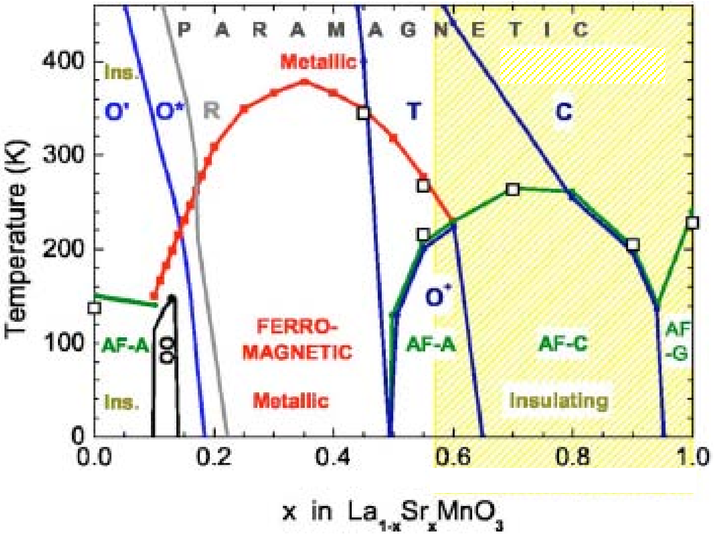

Fig. 1.5: *$La_{1-x}Sr_xMnO_3$ phase diagram system for $0 \leq x \leq 1.0$ (from Szewczyk et al.[156]). C, T, R, O^*, $O^{'}$, and O^+ denote, respectively, the cubic $Pm\bar{3}m$, tetragonal $I4/mcm$, rhombohedral $R\bar{3}c$, two orthorhombic $Pbnm$, and orthorhombic $Fmmm$ structural phases. AF-A, AF-C, and AF-G stand for the antiferromagnetic phases of the A,C, and G type, respectively. OO denotes the region of stability of the orbitally and charge ordered, insulating, ferromagnetic phase. "Ins." stands for "insulating".*

In addition to the ferromagnetic ordering, LSMO exhibits different antiferromagnetic spin arrangements at low temperatures, from 200 K and below. These are $A-$, $C-$, or $G-$type antiferromagnetism. In an $A-$type lattice spins in the individual layers are ferromagnetically ordered but antiferromagnetically ordered to the spins in the adjacent layers. $C-$type is characterized by ferromagnetic ordering to the sites above and below but antiferromagnetic to the four nearest neighbours in the plane. When all of the six nearest neighbours are antiferromagnetic, the arrangement is called $G-$type. The end-members are paramagnetic at room temperature.

At lower temperatures with $x = 0.1$ doping the LSMO present charge ordering. In order to reduce the Coulomb repulsion, electrons in a solid having ionic character may become localized in such a way that a lattice with an ordered arrangement of cations with different valences are formed. The localization of the charges renders the material insulating and also promotes antiferromagnetism. Thus charge ordering and double exchange are competing phenomena.

The end member of the phase diagram $SrMnO_3$ ($x = 1$) crystallizes in a simple cubic $Pm\bar{3}m$ structure. This cubic structure extends to lower values of x, with a transformation to a tetragonal $I4/mcm$ phase around $x = 0.7$ at room temperature and increasingly higher values of x at lower temperature. Upon decreasing temperature in the approximate composition range $0.5 - 0.6$, the tetragonal structure transforms to an orthorhombic $\delta\ \gamma\ \gamma\ \gamma$ structure. With further decrease of , one observes at room temperature the structural transformations from the tetragonal to the rhombohedral $\beta\bar{3}\alpha$phase, which is stable for $0\ 17 < \quad < 0\ 45$, and then to the two forms of the orthorhombic $\rho\gamma$ structure π for $0\ 115 < \quad < 0\ 17$ and π for $0 < \quad < 0\ 115$.

1.5 Electronic transport

The temperature behavior of the electrical resistivity depends strongly on the doping level (Fig. 1.6). As the temperature decreases, $\mu < 0$ is observed, corresponding to the metallic phase; on the other hand above μ we have $\mu > 0$.

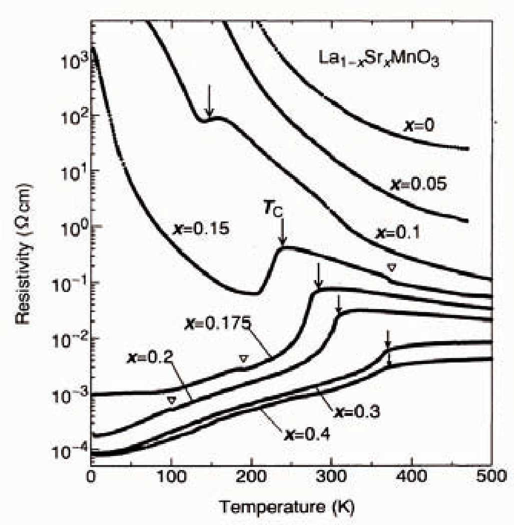

Fig. 1.6: *Temperature dependence of the resistivity in zero field for* $\chi\phi_1 \quad \tau\ \sigma\ \rho\pi_3$. *Arrows indicate the critical temperature for the ferromagnetic transition. Open triangles represent structural transitions. (From Urushibara et al.*[166]*)*

At low doping, LSMO is insulator at 300 K and above. One of the remarkable features of this compound is that the metallic behavior can be induced by increasing the relative amount of $\sigma\ \rho^{4+}$. This is done by substitutional doping, i.e. $\chi\phi^{3+}$ are partly replaced with τ^{2+}. From close to $= 0\ 2$ and up to $= 0\ 4$ of $\sigma\ \rho^{4+}$, the materials are metallic at room temperature.

1.6 Applications of manganites in devices

Perovskite manganites, demonstrated a large potential for applications based on their various physical and chemical properties[37,47,67,173]. The magnetic field sensitivity of the transport properties, the strong metal insulator transition at the Curie temperature, the electric field polarizability of the material and its subsequent effect on the transport properties, the half metallicity of the electronic bands, etc, could possibly be exploited in a variety of devices, few of them are described below.

- The magnetoresistance of manganites might be used in magnetic sensors; magnetoresistive read heads and magnetoresistive random access memories. Magnetic sensors can be made from either thin films or single crystals and can be used to sense the magnitude of a magnetic field in one or several directions by choosing the right crystal form and demagnetizing factor. A good low field magnetoresistive response, however, can be obtained in manganite samples with a high density of grain boundaries and in tunnel spin valve structures. A simple prototype position sensor based on a thin film with permanent magnet bias has been already developed[9,10].
- The electric field effect has also been observed in manganites. Here the top layer can be paramagnetic, such as STO, or a ferroelectric layer, such as PZT ($PbZr_{0.2}Ti_{0.8}O_3$), and the bottom layer is a CMR material, but the changes are more profound in the case of PZT, where only 3% change in the channel resistance is measured over a period of 45 min at room temperature, which makes this material attractive for non-volatile ferroelectric field effect device applications.
- The large temperature coefficient of resistance (TCR, calculated as $(1/R)(dR/dT)$) just below the resistivity peak makes these CMR materials interesting for use in bolometric detectors used for detecting and measuring radiation.
- At low temperature, the combination of high-T_c superconducting cuprates thin films and CMR manganites could lead to new spin-injection devices[55].
- Chemical applications include catalysis, such as catalysts for automobile exhausts, oxygen sensors and solid electrolytes in fuel cells. The catalytic activity is associated with the $Mn^{3+} - Mn^{4+}$ mixed valence and the possibility of forming oxygen vacancies in the solid.
- Resistive memory (RRAM) is one of the strong emerging technologies in the modern memory field. This type of memories has the potential to replace several current memory types.

However, for a great number of these possible applications, these materials have to be prepared in thin film form and because of this reason many research work has been carried out to get the best structural and physical properties of these thin films. Composition of thin films, oxygen content, film thickness, lattice strains induced by the lattice mismatch, among others, play a crucial role in determining its magnetic and transport properties.

1.7 Literature review

Obviously, the above introduction to the physics of doped lanthanum manganites is far from being complete, thus the section will be closed by a chronological listing of some review articles on the field. The very different approaches of the corresponding authors are another indicator of the extreme complexity of the topic.

- The article of *Ramirez*[129] is entitled *Colossal magnetoresistance* and considers not only the mixed-valence manganites, but also other compounds that show the CMR effect, such as certain spinels and pyrochlores.

- One of the most complete compilations of knowledge on mixed-valence manganites can be found in the paper by *Coey et al.*[37]. The authors tackle the topic from the materials science point of view. A profound base of knowledge concerning the historical results on manganites, fundamental magnetic interactions in solids, magnetic semiconductors in general, as well as bulk and thin-film preparation is given. The electronic structure is discussed in the ionic picture as well as in the band picture, and the most important results from measurements of magnetic properties, electronic and thermal transport, and of the optical response are summarized.

- *Moreo and Dagotto et al.*[42,110] (1999-2001) strongly stress the importance of phase separation scenarios in theory and experiment.

- The article of *Tokura and Tomioka*[164] (1999) makes an overview in the light of the mechanism of the colossal magnetoresistance.

- *Nagaev*[113] (2001) reports experimental and theoretical interpretation for CMR materials putting in evidence similarities between the transport and magnetotransport properties of the ferromagnetic semiconductors and manganites.

- *Prellier et al.*[127] (2001) reviews the different experimental techniques and the effects of the deposition procedure of the manganite thin films, as well as the relationship between the structural and the physical properties.

- The article by *Salamon et al.*[138] (2001) points out the significance of the manganites as a model system for modern solid-state theory due to the many degrees of freedom, and emphasizes the role of theory for a complete understanding of those compounds. The key feature of the paper is that listings of the most important phenomenological facts in manganite physics are given for different temperature regimes, since manganite behavior is very different above and below T_c.
- The review papers of *Haghiri-Gosnet et al.*[67] (2003) and *Dörr*[47] (2006) lay a special focus on manganite thin films and possible device structures. Besides summaries of general manganite physics, the role of epitaxial strain in thin films is discussed as an additional and controllable degree of freedom.
- *Van Tendeloo et al.*[170] (2004) review the microstructural changes through a transmission electron microscopy study of bulk as well as thin film colossal magnetoresistance materials.
- *Tokura*[163] (2006) discusses the modifications in the electronic phase diagram as well as in the magnetoelectronic properties near the bicritical point that is formed by such a competition of the two phases.

Chapter 2

Spontaneous Outcropping of Self-Assembled Insulating Nanodots in $La_{0.7}Sr_{0.3}MnO_3$ thin films

> *"Knowledge is in the end based on acknowledgement."*
> Ludwig Wittgenstein

2.1 Introduction

Nanoscale manipulation of functional materials is generating a very broad interest in many fields such as electronics, optics, magnetism, ferroelectricity, or superconductivity owing to the capability of modifying the fundamental properties or even to generate dramatically new functionalities. Nanomagnetism has become a very rich arena where new phenomena are being discovered with many potential applications in magnetic recording, spintronics, sensors, biomedicine, etc[133,185]. Also, it has been shown that vortex pinning centers can be generated in superconducting films grown on top of surface nanotemplates[50], similarly to nanocomposite films[65].

Two general approaches, lithography and self-assembling, have been already found to be extremely successful in metallic and semiconducting nanostructure generation in surfaces[12,149,158,185]. Complex oxides, instead, have only recently become an object of intense study. The formation of self-assembled oxide nanostructures by vapor deposition techniques have been found to follow either the Volmer-Weber or Stranski-Krastanov mechanisms, similarly to semiconductor systems[158], while chemical solution deposition (CSD) (see sec.7.1) has been only recently started to be used as a powerful bottom-up nanofabrication methodology[58,59]. Three-dimensional self-organized nanocomposite films have also very recently appeared as promising candidates for the generation of new physical phenomena, such as multiferroic behavior[186], but also to tune their physical properties, such as magnetoresistance in a percolative transport system[112].

Among the complex oxides, rare-earth manganites of the type $Ln_{1-x}A_xMnO_3$ (Ln is a rare earth,A is a alkaline earth) have become an extremely rich family of compounds displaying a wide variety of behavior, such as ferromagnetism, metallic conductivity, antiferromagnetism, colossal magnetoresistance, charge order, phase separation, insulating states, etc.[37,138,163] Additionally, a strong link between these states can be induced, either by modified composition, oxygen stoichiometry or strain state, or by several types of external parameters, such as temperature, pressure, magnetic, and electric fields, X-ray irradiation, etc. The metallic ferromagnetic phase $La_{1-x}Sr_xMnO_3$ with $x = 0.3 - 0.4$ has been found to be one of the most robust manganites and hence it is often selected as a model system to investigate nanoscale phenomena.

2.2 Results and discussion

In the present chapter, a new strategy is proposed to generate self-assembled nanostructures from a nanocomposite film which can be explained by the classical Stranski-Krastanov growth mechanism. We propose that the same elastic strain energy, behaving as driving force for the formation of nanodots over a wetting layer, controls the topological arrangement of a phase segregated nanocomposite system consisting of a wetting layer with nanodots on its surface. The crystalline phase, having the higher interfacial misfit, will outcrop as self-assembled nanodots at the surface of the strained film.

2.2.1 Evolution of surface morphology

The surface morphology of the CSD-LSMO films was found to strongly depend on thermal annealing conditions. While at 900°C a granular structure (epitaxial grains with a grain size of a few tens of nm) is observed in the scanning force microscope (SFM) images (Fig. 2.1(a)), at 1000°C for 1h a change in the morphology occurs, and flat square grains (with local roughness $\sim 1nm$) are formed (Fig. 2.1(b)). These terraces have a typical size of about $200nm^2$. In spite of an atomically flat grain surface, the global roughness, $5.5nm$, has not improved, mainly due to the presence of intergranular parallelepipedic pinholes, probably crossing the whole film. A grain coalescence process occurs and these flat terraces are further extended forming a quasi continuous flat surface. In this case, atomically flat surfaces are developed over more than 90% of the surface area[74].

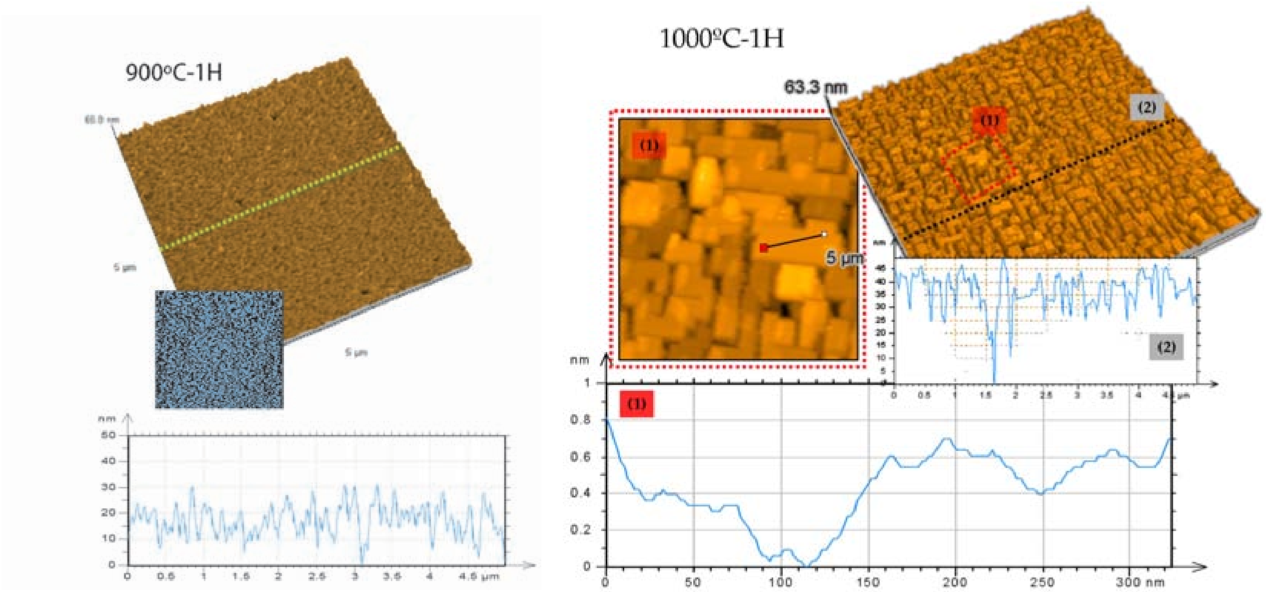

(a)

(b)

Fig. 2.1: *Topographic SFM images ($5\mu m \times 5\mu m$), LSMO films grown during 1 h on an STO substrate at 900ºC and 1000ºC, respectively.*

Strikingly, however, annealing the films at 1000ºC for extended periods (several hours) leads to the spontaneous formation of self-assembled nanodots at the film surface. Figure 2.2(a-c) displays three typical SFM images, with the corresponding profiles, obtained on films with different island sizes developed on atomically flat LSMO films. As it is seen, polyhedral nanodots with heights up to $\backsim$ 50 nm and a fairly narrow size distribution outcrop on the atomically flat LSMO surface. The annealing conditions (temperature and time), together with the metal concentration in La-Mn ratio, allow tuning the size and concentration of the polyhedral nanodots. For instance, the equivalent diameter (D), mean height (h), concentration (N) of the nanodots, and total volume of the outcropped nanodots per unit surface (V) seen in figure 2.2(a-c) were estimated to be: a) $D \approx 60 \pm 20nm$, $h \approx 4 \pm 3nm$, $N = 14dots/\mu m^2$, $V \approx 0.45 \times 10^3 nm^3/\mu m^2$; b) $D \approx 336 \pm 56nm$, $h \approx 40 \pm 10nm$,$N = 2dots/\mu m^2$, $V \approx 45.2 \times 10^3 nm^3/\mu m^2$; c) $D \approx 270 \pm 60nm$, $h \approx 50 \pm 20nm$, $N = 8dots/\mu m^2$, $V \approx 114.5 \times 10^3 nm^3/\mu m^2$

The increase of the nanodot volume with annealing time suggests that the outcropping process is kinetically limited while the reduction of the nanodot concentration N with the annealing time

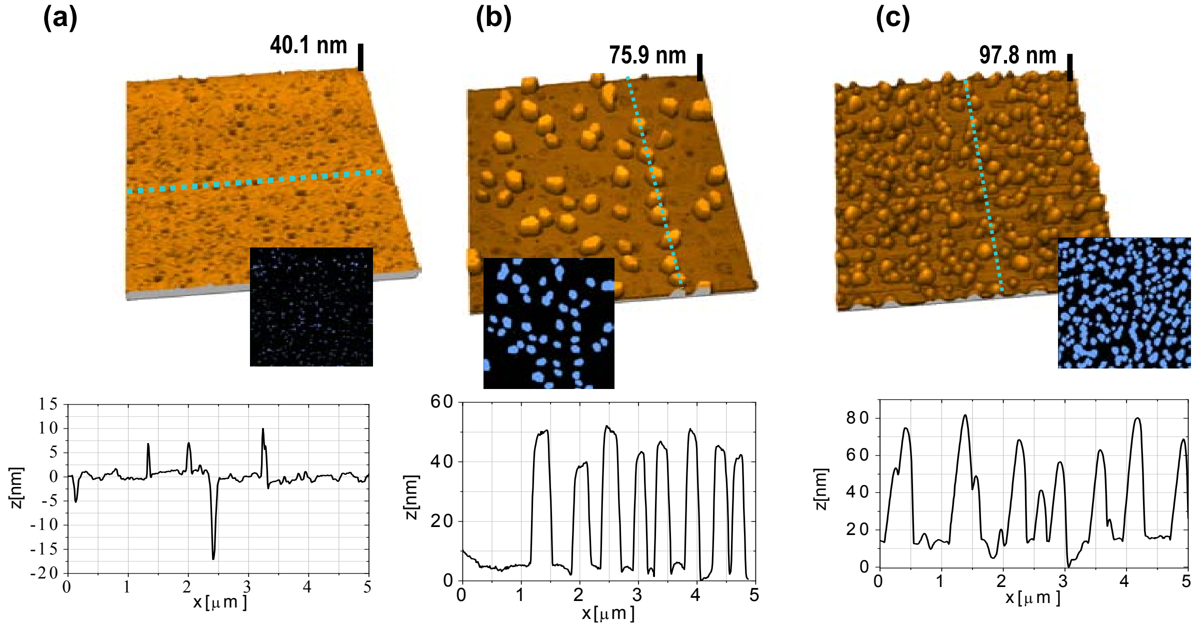

Fig. 2.2: *Topographic SFM images ($5\mu m \times 5\mu m$), binarized area and profile across several nanodots of LSMO films with different concentrations and size of LSO nanodots. a,b) Stoichiometric LSMO films grown at 1000ºC on an STO substrate during 8 and 12 h, respectively; c) LSMO film grown at 1000ºC during 12 h on STO with 20 mol % excess of La propionates precursor content in the starting solution.*

indicates that coarsening occurs simultaneously pointing out the importance of surface diffusion. On the other hand, the strong increase in the total nanoislands volume for samples with La excess (Fig. 2.2c) clearly demonstrates that the nanodot size and concentration can be tuned through the initial composition and annealing process. A high resolution TEM cross-section investigation was therefore carried out to investigate the structure of the film and the possible influence of the phase segregation process on the film physical properties.

2.2.2 Structural analysis

Heteroepitaxial growth of LSMO films was confirmed by XRD analysis (Fig. 2.3), indicating a cube-on-cube orientation relationship (100)LSMO//(100)STO (pseudo-cubic indexation for LSMO will be used throughout for simplicity). No peaks corresponding to secondary phases or organic contaminants were found in these diffraction patterns. Similar results have been obtained in all samples for different thermal treatments.

Figure 2.4 presents typical reciprocal space maps scanned around the (103) reflections of STO and LSMO. The coordinates system is oriented with the horizontal axis, $Q_x//[100]$, parallel to the

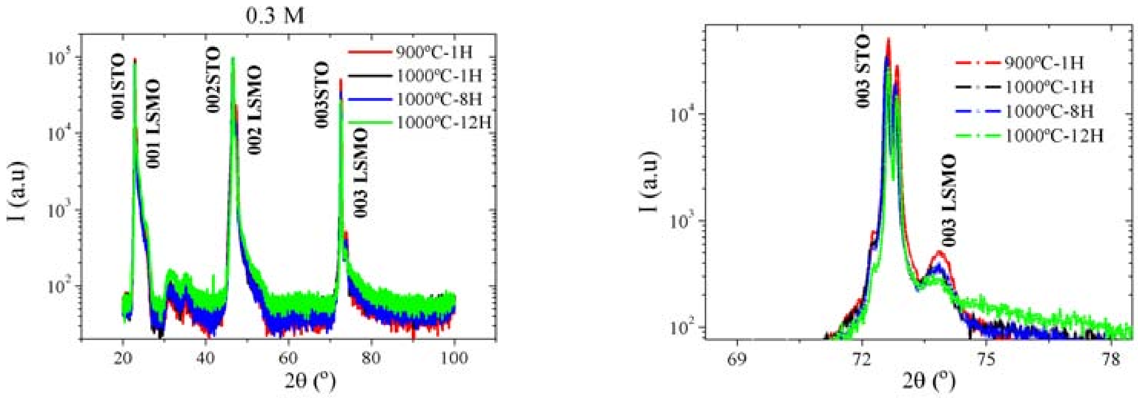

(a) X-ray diffraction pattern overwiew displaying (00l) LSMO and STO reflexions.

(b) Zoom around (003) LSMO reflexion.

Fig. 2.3: *Typical $\theta - 2\theta$ x-ray diffraction patterns for a $La_{0.7}Sr_{0.3}MnO_3$ film grown by chemical solution deposition on $SrTiO_3$ substrate for different thermal treatments.*

substrate interface and the vertical axis, $Q_y//[010]$, perpendicular to the substrate. In figure 2.4, rlu means "reciprocal lattice units" and $1\ rlu = 2/\lambda$ with $\lambda = 1.54184\ \AA$. Figure 2.4 clearly reveals that the in-plane component Q_x of (103)LSMO matches perfectly with the STO lattice parameter in the three cases, indicating that the films are fully strained (in the case of 1000°C-12h $a_{//} = 3.905\ \AA$, the same value to the STO lattice parameter $3.905\ \AA$[20]), while a compressive strain occurs perpendicular to the substrate with values around $a_{\perp} = 3.851\ \AA$.

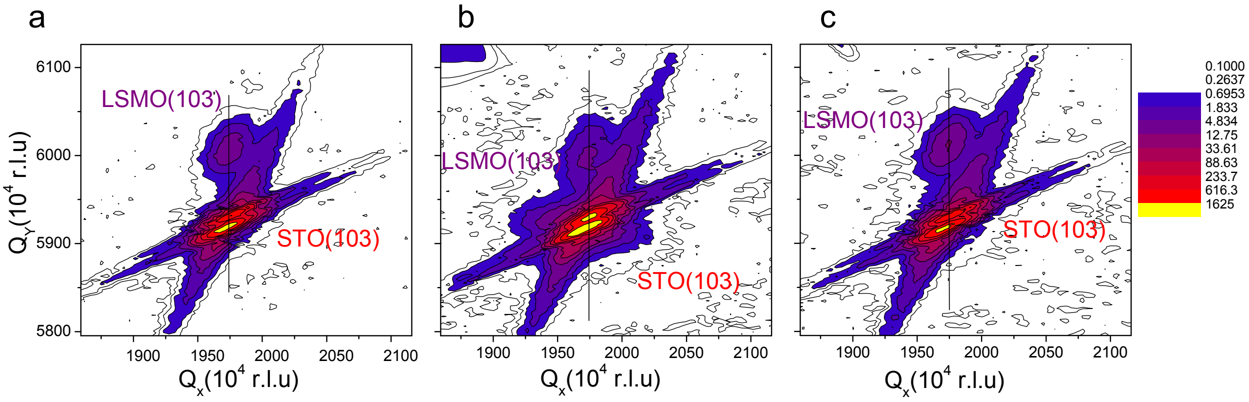

Fig. 2.4: *Strain states of thin films. XRD reciprocal space maps around the LSMO($\bar{1}03$) reflection from the films grown on STO(0 0 1) for 900°C-1 hour (a), 1000°C- 1 hour (b) and 1000°C-12 hours (c). According to the data, the lattice constant of in-plane ($-\lambda/2Q_x$) and out-of-plane ($3\lambda/2Q_y$) can be deduced.*

The diffraction averaged in-plane and out-of-plane strains of the LSMO films are therefore tensile,

$\epsilon_{//} = (a_{//} - a_{bulk})/a_{bulk} = +0.826\%$, and compressive, $\epsilon_{\perp} = (a_{\perp} - a_{bulk})/a_{bulk} = -0.568\%$, respectively, where $a_{bulk} = 3.873\ \mathring{A}$[71]. The fully strained structure was found to exist independently of the thermal treatment and is consistent with the fact that critical film thickness is below the critical value for misfit dislocation formation measured for PLD-LSMO to be > 100 nm[102]. We note that this fully strained state is not usually observed in films grown by CSD[23,125].

Lattice parameters derived from both reciprocal space maps and $\theta - 2\theta$ scans are represented in table2.1.

Thermal treatment	$a(\mathring{A})$	$c(\mathring{A})$	$\epsilon_{//}(\%)$	$\epsilon_{\perp}(\%)$	$c_{\theta-2\theta}(\mathring{A})$
$900^oC, 1H, 0.3M$	3.902	3.851	0.749	−0.568	3.852
$1000^oC, 1H, 0.3M$	3.904	3.852	0.800	−0.542	3.856
$1000^oC, 8H, 0.3M$					3.854
$1000^oC, 12H, 0.3M$	3.905	3.851	0.826	−0.568	3.850

Tab. 2.1: *In-plane ($a = -\lambda/2Q_x$) and out-of-plane ($c = -3\lambda/2Q_y$) cell parameters derived from the reciprocal space maps displayed in Fig. 2.4. Out-of-plane $c_{\theta-2\theta}$ from $\theta - 2\theta$ X-ray diffraction pattern.*

2.2.3 Microstructural analysis

A typical low magnification image of a 12 h annealed stoichiometric film, viewed along [010] is shown in figure 2.5a. The LSMO film thickness was found to change smoothly from one observed area to another with values comprised between $\backsim$ 20 and $\backsim$ 26nm. The image clearly shows flat islands with lateral facets and sizes in the range $20 - 55nm$ in height and $90 - 280nm$ in length. The nanodots facets are found to form an apparent angle of about 45° with the substrate surface. It is furthermore observed that the nanodots penetrate into the LSMO film, which is therefore thinner below the nanodots which in some cases reduce considerably its thickness.

EELS analysis were performed across the nanodot-film and film-substrate interfaces. Results are shown in figure 2.5b. The set of spectra were taken every $3.5nm$ using an electron probe with a beam diameter of $0.5nm$. The positions of the starting and final spectra are indicated by 1 (substrate) and 2 (nanodot), as indicated in inset and plot. As expected, the O-K edge peak at 532 eV is observed through the whole profile. It is also clearly observed that the La $M_{5,4}$ edge persists across the film-nanodot interface while the Mn $L_{3,2}$ line is confined within the LSMO layer. This indicates that the nanodots have a significant content in La and lack of Mn. EELS did not yield reliable information about Sr because of the unfavorable energies associated to its edges[175]. However, energy dispersive

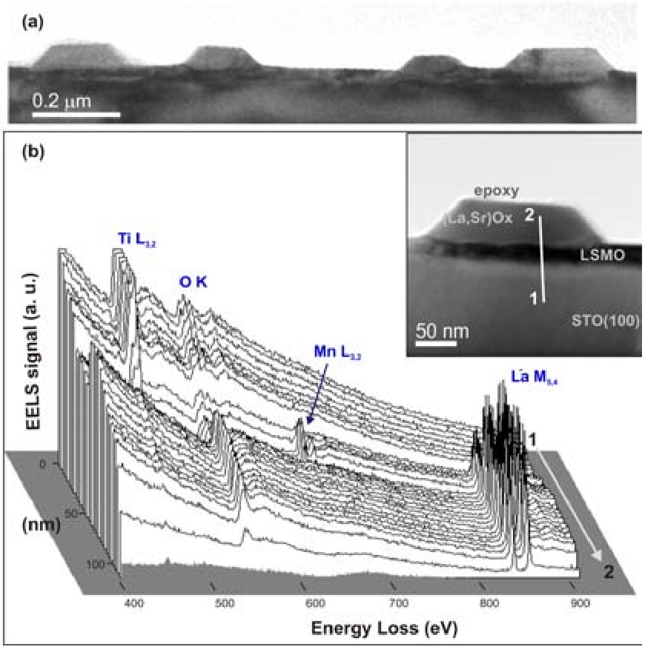

Fig. 2.5: *TEM-EELS analysis of an LSMO film grown on an STO substrate during 12 h at 1000ºC. a) Low magnification cross-sectional TEM image showing a general view of the system; b) EELS line scan across the interfaces nanodot-film and film-substrate, as shown in the inset. The scan was performed from 1 to 2.*

X-ray spectroscopy (EDS) results gave significant amounts of Sr ($20 - 30wt\%$).

In addition to the outcropped LSO islands, TEM observations revealed the occurrence of rounded inclusions, about $10 - 20nm$ in diameter, embedded within the LSMO film. Figure 2.6a is a low magnification cross-section image including an LSO island and such an inclusion, labeled Ruddelsden-Popper[*] (R-P). In order to gather high spatial resolution chemical information from such inclusions, energy filtered imaging was carried out using a Cs corrected electron microscope operated at 200 kV, enabling a spatial resolution of 1 nm. To that purpose, an inclusion in contact with the roots of an LSO island was selected enabling direct comparison between both phases. Figure 2.6b and c presents the conventional elastic-electron image corresponding to the analyzed area, and the La-$M_{5,4}$-edge distribution map, respectively. Clearly, the island appears La-rich while the inclusion exhibits a contrast even darker than the surrounding LSMO matrix, as expected from stoichiometric balance considerations.

In the analyzed LSMO [010] zone axis images, such inclusions typically exhibit either cubic-like or

---

[*] The Ruddlesden-Popper phases of the manganites are characterized by the general formula $(RE, M)_{n+1}Mn_nO_{3n+1}$. They consist of n connected layers of vertex-sharing MnO_6 octahedra separated by rock-salt type layers $(RE, M)O$; $n = \infty$ corresponds to the usual three-dimensional perovskite.[136]

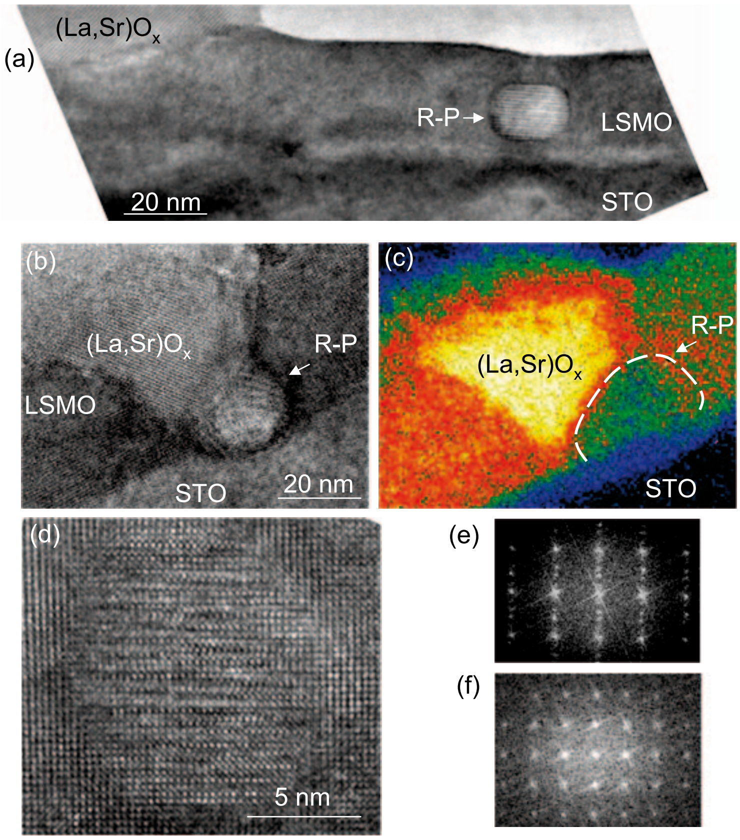

Fig. 2.6: *TEM cross-section analysis of inclusions embedded within the film. (a) Low magnification magnification image showing the three-phases building the epitaxial system: An* $(\chi\phi \quad \tau) \qquad \lambda$ *island, an embedded R-P type inclusion, and the LSMO film; (b,c) correspond to the elastic electron and* $\chi\phi$ σ $_{5\ 4}$ *edge filtered images, respectively, of an area including an* $(\chi\phi \quad \tau) \qquad \lambda$ *island and a neighboring* β *type inclusion; (d) high resolution image of an* β *inclusion viewed along its [100] zone axis; (e) FFT spectrum corresponding to (d); (f) [001] zone axis FFT spectrum corresponding to an* β *type inclusion different from (d) (not shown).*

tetragonal-like structural projections. As an example, figure 2.6d and e shows a high resolution TEM image of an [100] oriented inclusion and its corresponding FFT (fast Fourier transform) spectrum (e), respectively. Figure 2.6f is a [001] zone axis FFT spectrum corresponding to a different inclusion. This indicates that these inclusions hold an epitaxial relationship with the surrounding LSMO matrix. Considering that the observed two types of projection correspond to two major zone axis, namely [001] and [100] or [010], the lattice parameters derived from the FFT spectra yield lattice parameters 3 8 and 19 7 ν , which fit with the $\rho = 2$ R-P structure[136](S.G. I4/mmm, ϕ ϕ , α 20 ν)[148]. Thus, the epitaxial relation is given by (001)[100]R-P//(001)[100]LSMO. This structure is formed by the insertion of a rock-salt-like unit, $\tau\pi$, every $\rho (= 2)$ perovskite-type blocks, $\tau\sigma \ \rho\pi_3$.

The Sr cations can in fact be replaced by La, resulting in an increase of the lattice parameters[148]. As a general behavior, [001] images exhibit rather perfect crystallinity, while [100] or [010] ones feature strong disorder, both in the stacking sequence and in the lateral continuity of atomic layers. In fact, stacking disorder is common in these phases[147]. Thus, it is likely that both, structural mismatch and cationic balance are further accommodated through structural and chemical disorder (mostly in the form of stacking faults and lateral discontinuity of atomic layers) in addition to elastic strains within the inclusions.

Figure 2.7a and c compares high resolution cross-sectional TEM images corresponding to an island partly embedded in the film, with an island free film region. Strain contrasts can be observed associated to the root of the island, while the free-film exhibits a high structural perfection. The most significant lattice spacings obtained from the high resolution image of the island are: 8.37 and 5.41 $\AA$, which, to the authors knowledge, do not correspond neither to the sesquioxide $Sr_{0.2}La_{1.8}O_{2.97}$[49], nor to any other Sr-La-O reported phase, namely: $Sr_3La_4O_9$[143], La_4SrO_7[52], $La_2Sr_2O_5$[53], and La_2SrO_x[54]. A structural determination of these nanodots falls beyond the scope of the present study. However, careful analysis of the buried roots of the island reveal that they sustain an epitaxial relationship both perpendicularly and parallel the film. This is indicated in figure 2.7c showing a SAD (Selective Area Diffraction) pattern taken across the island-film interface, where the coincident lattice is marked by a dashed line. Matching distances are found to be $d_{//} = 4.055\ \AA$ and $d_{\perp} = 4.048\ \AA$, parallel and perpendicular to the interface, respectively, yielding misfit strains $\epsilon_{//} = 4.7\%$ and $\epsilon_{\perp} = 4.5\%$. Spot splitting between both diffraction patterns are better observed for higher order reflections, as for instance between the (002)LSMO and (-200)LSMO spots and those labeled 1 and 2 for the island, respectively.

In order to investigate the interaction of mismatch strains originated at the island interface with those originated at the substrate, SAD patterns containing the LSMO-STO interface beneath and far from the islands were compared. The SAD pattern shown in figure 2.7b corresponds to the island free region. The solid square indicates spots due to the STO substrate while the dashed square shows the spots coming from the LSMO film. The pattern is consistent with the rhombohedral structure of LSMO (S.G. R-3c) and indicates a cube-on-cube epitaxial relationship. Spots contributed by both, STO and LSMO, appear more intense and are elongated along [001], perpendicular to the interface. Careful inspection of higher order spots reveals splitting in that direction, as demonstrated in the magnified view of the (-103) STO and LSMO reflections. On the other hand, within experimental resolution, the pattern indicates complete matching between film and substrate parallel to the interface,

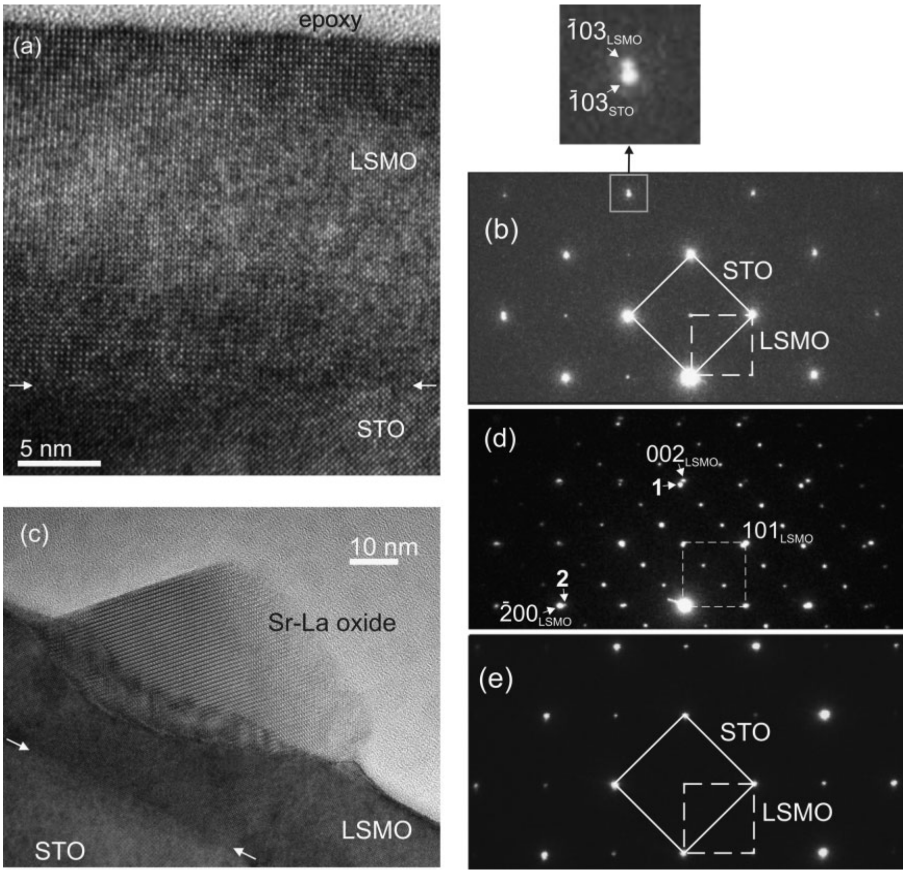

Fig. 2.7: *(a) Cross-sectional HRTEM image of the LSMO film and STO/LSMO interface in an area far away from the LSO nanodots influence; (b) electron diffraction pattern of a selected area displayed in (a) covering STO substrate and LSMO film; (c) HRTEM image of the LSMO film under a nanodot showing the STO/LSMO and LSMO/island interfaces; (d) SAD pattern taken across the island-LSMO interface illustrating the matching distances between both phases. 1 and 2 mark spots originated by the island; (e) electron diffraction pattern taken at an area covering LSMO film under a nanodot and the STO substrate.*

i.e., $a_{//}(LSMO) \backsim a_{//}(STO) = 3.905\ \mathring{A}$. Thus, LSMO film regions not affected by the interaction with nanodots appear under an in-plane tensile stress and the corresponding compression perpendicular to the substrate, in agreement with the averaged view provided by X-ray diffraction (Fig. 2.4). When $\nu = 1/2$, the unit cell volume is preserved under strain, otherwise, it changes. The strain values determined for the LSMO regions not affected by the interaction with the nanodots are $\epsilon_{//} = +0.83\%$ and $\epsilon_{\perp} = -1.03\%$. These values yield a Poisson ratio $\nu = \epsilon_{\perp}/(\epsilon_{\perp} - 2\epsilon_{//})$ of 0.38, close to that determined by Maurice et al.[102] for a $La_{2/3}Sr_{1/3}MnO_3$ film, $\nu = 0.34$, thus signaling that the unit cell volume of these strained films was increased compared to the bulk value.

Figure 2.7e corresponds to the SAD pattern obtained across the LSMO/STO interface in the region beneath an LSO nanodot. Again, the diffraction spots due to the STO and LSMO structures are connected by solid and dashed squares, respectively. In this region, the film also corresponds to a rhombohedral LSMO phase. However, careful inspection of the pattern did not reveal any signature of spot splitting or even elongation in any direction, i.e., diffraction spots coming from the two different lattices are apparently fully coincident. Thus, within our experimental accuracy, comparison between the SAD patterns obtained from regions far from and below the nanodots, does not reveal any apparent difference concerning the in-plane lattice parameters. However, the c-axis parameter of the LSMO film becomes tensile stretched below the LSO nanodots by $\backsim +0.83\%$, resulting in an expanded LSMO unit cell volume $\Delta V/V \backsim +2.5\%$, as compared to the bulk LSMO unit cell.

2.2.4 Discussion

The results reported above indicate that a complex chemical segregation phenomenon lies at the root of the new mechanism of surface nanodot formation. The observation of a coarsening effect, enhanced by temperature, and a higher La concentration suggest that the LSO nanodots arise as a consequence of a kinetically limited surface outcropping process, probably cooperatively driven by the thermodynamic instability leading the simultaneous formation of the outcropped LSO islands and the $Sr_3Mn_2O_7$ embedded inclusions, and a reduction of the total elastic energy of the resulting three phase nanostructure. The observed topological distribution of segregated phases is governed by the energy cost associated with the creation of new interface and surface area. In this sense, it is worth noting that the n=2 R-P structure consists the alternation of two perovskite layers with a single rock-salt-type layer[171]. Therefore, there exists a favorable structural compatibility between this structure and the LSMO and STO ones, that would explain why this phase remains typically embedded in the film and occasionally in contact with the STO surface (Fig. 2.6a), while the LSO phase tends to minimize its interface area with the film. Thus, to a first approximation the contribution of the R-P inclusions to the elastic energy of the coherently strained LSMO film can be neglected. In this way, the elastic energy per unit surface can be approximated by $E_{el}(LSMO) \propto \epsilon^2 t$, where ϵ is the lattice misfit and t the film thickness. This energy is the driving force for defining a critical thickness for misfit dislocation formation. If a coherently strained LSMO/LSO nanocomposite film would be formed with the same epitaxial order described above, and with respective surface occupancies $(1-x)/x$, the total elastic strain energy per unit area E_{el}^{nc} could be written as:

$$E_{el}^{nc} = (1-x)E_{el}(LSMO) + xE_{el}(LSO) + E_{int} \tag{2.1}$$

where E_{el}(LSO) is the corresponding elastic energy of an epitaxial LSO film growing on STO, which is higher than E_{el}(LSMO) due to the enhanced misfit strain and E_{int} is the elastic strain energy associated to the LSMO/LSO interfaces, which would depend on the geometrical arrangement of the two phases within the nanocomposite film. In the present case, due to the high lattice misfit of LSO with both the STO substrate and the LSMO phase, it is anticipated that E_{el}^{nc} will be high. Previous investigations of nanocomposite epitaxial films, such as LCMO/MgO or LSMO/ZnO,[90,112] showed that a columnar phase separated structure could be formed with stress accommodation through a structural phase transition of LCMO. The main difference in the present system is that both phases of the nanocomposite are elastically strained while in LCMO/MgO nanocomposites, one of the phases (MgO) was not strained because the substrate was also MgO. Our observation of an outcropping phenomenon should be driven then by a decrease in the total elastic energy of the nanocomposite film in a way which can be considered somehow similar to that described in the Stranski-Krastanov growth mechanism for films with a single composition. In the present case, a generalized theoretical analysis would require consideration of the complex equilibrium phenomena revealed by the observed chemical segregation.

In the Stranski-Krastanov nanodot formation mechanism[149,159], a strained wetting layer persists while coherently strained nanodots are formed at the surface driven by an elastic relaxation term (negative energy term), even if an extra surface is formed (generally contributing with a positive energy term). The more complex problem of morphological evolution of nanocomposite films still lacks of theoretical analysis and so there is no prediction of the novel outstanding behavior reported here for the LSMO/LSO system: the spontaneous formation of nanodots at the surface with a composition La-Sr-O naturally selected on the basis of minimization of the elastic energy of the nanocomposite film. The remaining wetting layer keeps the composition having the lowest elastic energy with the substrate, i.e., LSMO. A thermodynamic analysis of the new self-assembled nanostructure could be made where the increase of the energy of the self-assembled island/LSMO nanodot-film E^{sa}, as compared to an equivalent LSMO/LSO nanocomposite film (Eq. (2.1)), can be then written as:

$$E^{sa} = x\left[E_{el}(LSMO) - E_{el}(LSO)\right] - E_{int} + E_{s}^{nd} + E_{el}^{nd} \tag{2.2}$$

Where E_{s}^{nd} is a positive term including the extra surface and interface energies associated to the nanodots formation, E_{el}^{nd} is the elastic relaxation energy of the LSO nanodots and the other terms are defined in (Eq. (2.1)). For a parallepipedic nanodot with dimensions $a \times b \times h$, E_s^{nd} can be written as[116,149]:

$$E_s^{nd} = \gamma_1 \left(\frac{h}{t} - 1\right) ab - \Gamma_1 (a+b)h \tag{2.3}$$

where $\gamma_1 = u_s - u_i - u_t$ and $\Gamma_1 = u_t cos\theta + u_s cot\theta - u_i cot\theta - 2u_e csc\theta$. The u terms correspond to surface energies (per unit area) of substrate, of the island's top and edge side facets and the dot-substrate interface, respectively, h is the dot height, u is the angle of the lateral surfaces with the substrate, and t is the thickness of the equivalent flat film.

The third term E_{el}^{nd} in (Eq. (2.2)) is the elastic relaxation energy of the epitaxial nanodots associated to a non-uniform strain distribution within the island and it can be written for 3D islands as[116]:

$$E_{el}^{nd} = -\Lambda h^2 \left[b \ln\left(\frac{\alpha}{\Theta h} + \ln\left(\frac{b}{\Theta h}\right)\right)\right] \tag{2.4}$$

Λ is defined as $\Lambda = f^2(1-\nu)/\pi\mu$, where μ is the shear modulus, ν is Poisson's ratio, $f = (\sigma_a + \sigma_b)/2$ is the elastic force monopole along the island edge induced by the lattice mismatch, σ_i are the diagonal island stress tensor components and $\Theta = \epsilon^{\beta-3/2}$, where β is a numerical factor[116]. The spontaneous occurrence of outcropping means that the self-assembled phase-separated state has a lower energy $E^{sa} < E_{el}^{nc}$. In Equation ((2.2)), the only term that it is usually positive is E_s^{nd}, while the other three are negative, and hence in the present LSMO/LSO nanocomposite films they are dominant. We can then conclude that the outcropping process is enhanced when the in-plane stresses between the island and the wetting layer is large.

2.2.5 Macroscopic physical properties

We turn now to the analysis of the consequences of the new self-assembled nanostructures on the local properties of the LSMO films.We first measured, however, the macroscopic magnetic and transport properties of the films through magnetic hysteresis loop measurements, including the anisotropic magnetic behavior, and the temperature dependent magnetoresistance.

The dependence of the magnetization with the temperature was measured under 5mT in all the samples and we found that a sharp ferromagnetic to paramagnetic transition occurs with a Curie temperature $T_c \backsim 365K$ and high field magnetization measurements at 10K indicated a saturation magnetization $\mu_0 M_s \backsim 590mT$, a value very close to that of bulk LSMO[138,162,166], see figure 2.8a. The temperature dependence of the resistivity measured at zero magnetic field and under a magnetic

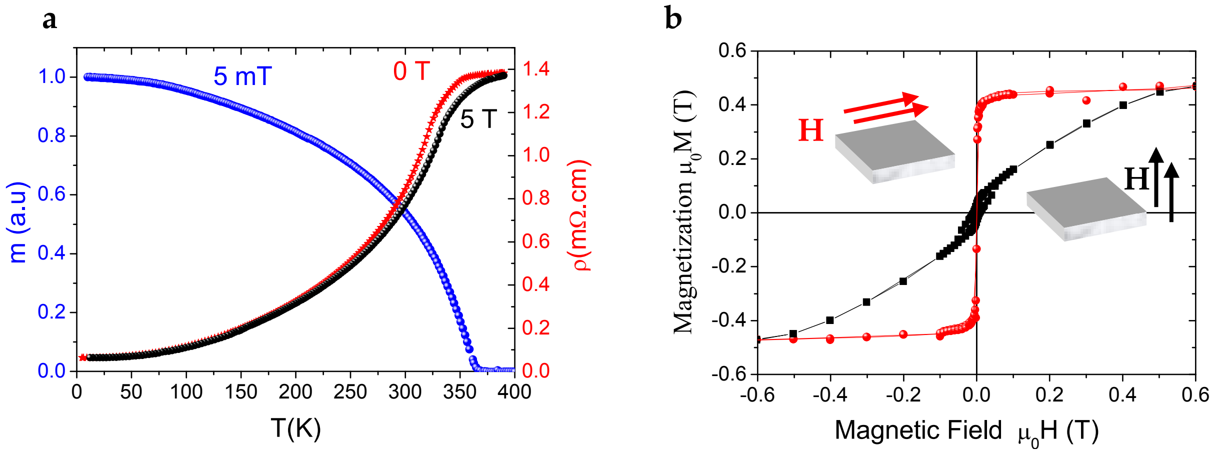

Fig. 2.8: *(a) Temperature dependence of the magnetization measured at 5mT for a typical LSMO film with* $(La, Sr)O_x$ *nanodots and electrical resistivity measured at zero magnetic field and under a magnetic field of 5 T; (b) isothermal magnetic hysteresis loops of an LSMO film measured at 300 K with the magnetic field oriented parallel (bullets) and perpendicular (squares) to the film substrate.*

field of 5T is also displayed in figure 2.8a. The observed resistivity $[\rho(300K) = 8.42 \times 10^{-4}\Omega cm]$ and maximum magnetoresistance ($\Delta R/R \backsim 11\%$) are very typical of those observed in high quality single crystalline thin films[138,162,166].

These results mean that the CSD grown LSMO films exhibit intrinsic macroscopic magnetic parameters (M_s and T_c) and transport properties very close to those of bulk values and that the bare macroscopic behavior of the films is not modified by the additional strain induced by the interfacial LSO nanodots. Isothermal magnetization loops revealed the macroscopic anisotropy of the films. Figure 2.8b displays typical loops measured at 300 K under in-plane and out-of-plane configurations. The magnetization curves reveal that the macroscopic behavior corresponds to an in-plane easy axis orientation with an anisotropy field $\mu_0 H_K \backsim 500mT$, as deduced from the saturation field on the hard axis magnetization hysteresis loop. This planar easy magnetic axis is that expected for in-plane tensile LSMO/STO films[68,190] where both the shape anisotropy energy ($E_S = \frac{1}{2}\mu_0 M_S^2$) and the magnetoelastic coupling contribute to the in-plane easy axis magnetic anisotropy. Magnetoelastic energy can also contribute to the magnetic anisotropy. This term can be written for strained thin films as ($E_{me} = -\frac{3}{2}\lambda\left[\sigma_\perp cos^2(\theta) + \sigma_\parallel sin^2(\theta)\right]$) where θ is the angle between the strain and magnetization, λ is the magnetostriction coefficient ($\lambda > 0$), and σ_i is the stresses along the two mutually perpendicular directions ($\sigma_i = \frac{3}{2}\epsilon Y$ with Y the Young's modulus, $Y = 5 \times 10^{11} Nm^{-2}$).[41,152]

The observed anisotropy field ($\mu_0 H_K \sim 500mT$) is very close to that estimated from the shape anisotropy ($\mu_0 M_s \sim 465mT$), therefore, we must conclude that the overall in-plane macroscopic magnetic anisotropy of the nanostructured LSMO films is preserved when interfacial Sr-La oxide nanodots are created and it is dominated by shape anisotropy. This is consistent with the estimated ratio of $E_{me}/E_s \sim 0.1$, taking into account that at 300 K, $\lambda \sim 10^{-4}$.[152] Actually, below the self-assembled nanodots the LSMO film has a null magnetoelastic coupling term because $\sigma_\perp = \sigma_\parallel$ and hence $E_{me} = -3/2\lambda(\sigma_\perp cos^2\theta + \sigma_\parallel sin^2\theta) = -3/2\lambda\sigma(cos^2\theta + sin^2\theta) = -3/2\lambda\sigma_i$ which means that, below the islands, this term does not contribute to the magnetic anisotropy (there is no dependence on the orientation of the magnetization).

Nanoscale electrical analysis was performed by C-SFM. By applying a voltage between the LSMO surface and the conducting tip, a current flow is generated. By simultaneously measuring topography and current images, the nanoscale electrical response of the surface is obtained. The measurements were recorded at room temperature, either in a dry nitrogen gas environment or under vacuum conditions (10^{-9} mbar).

Figure 2.9a shows a typical topographic image with its corresponding current map (Fig. 2.9b) obtained at a bias of $2.7V$ scanning at a speed of $0.5\mu ms^{-1}$ and with $50nN$ load. The flat regions in the current profile measured on the LSMO film are due to the saturation of the current amplifier, fixed to $5nA$ in the experimental set up used. Moreover, the current recorded on the LSO islands drastically drops to zero or negligible values, which accounts for a non-conducting nature. In conclusion, this kind of experiments confirm that the LSMO film preserves a conducting character, despite the presence of the LSO nanodots, which otherwise are found to be insulating.

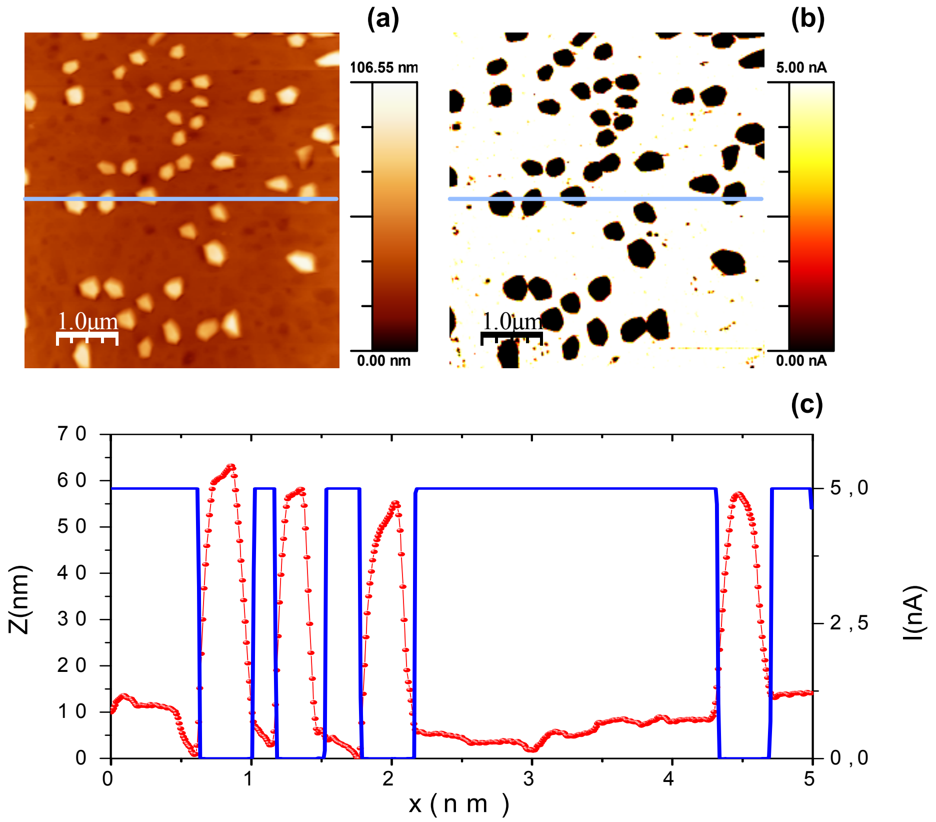

Fig. 2.9: *(a) SFM topography image of an LSMO thin film grown on an STO substrate at 1000ºC during 12 h with the nonmagnetic-insulating* $(La, Sr)O_x$ *nanodots imaged on the surface; (b) C-SFM image corresponding to the same surface displayed in (a) at* $V_{tip} = 2.7V$*; (c) profile following the lines indicated in (a) and (b) of the topography and the current measured with C-SFM. The maximun current detected are limited by the current amplifier, fixed to 5 nA in the experimental set up used.*

2.3 Summary

Summarizing, we have presented a new mechanism for the creation of self-assembled epitaxial nanostructures in a film surface. When an epitaxial nanocomposite film is formed, based on the phase separation of two crystallographic dissimilar structures, diffusion towards the surface of the film of the minoritary phase may occur spontaneously leading to the formation of self-assembled islands. The two crystalline phases investigated here have been LSMO and an unknown insulating LSO phase which appear by TEM to display a coherently strained structure, even though the strain state and the lattice symmetry of the LSMO film underneath the islands have been modified. We have shown that the concentration and size of the insulating nanoislands can be tuned through modification of the initial composition of the chemical solution and growth kinetics control. It is proposed that the driving force for the generation of the nanodots is a partial release of the elastic energy when the nanodots are formed at the surface. This is the same driving force for island formation in the Stranski-Krastanov mechanism and hence the new mechanism reported here can be considered as a generalized case, though the problem is considerably more complex because it also involves compositional separation of two phases. The spontaneous outcropping of self-assembled nanodots on top of an epitaxial wetting layer with a different composition appear then as a new opportunity to modulate at the nanoscale the physical properties of the underlying wetting film or to generate nanotemplates in a film surface.

2.4 Methods

LSMO films with superficial Sr-La oxide nanodots were deposited on (100) $SrTiO_3$ (STO) substrates by spin coating at 6000 rpm for 2 min and annealed at temperatures in the range 900-1000ºC under flowing oxygen gas for different annealing times up to 12 h. Final film thickness was estimated to be in the range $\sim 20 - 26nm$ by SFM in lithographed sample and cross-sectional TEM. X-Ray diffraction reciprocal space maps were obtained using a Bruker D8 Advance difractometer equipped with a four-angle goniometer and a general angle diffraction detection system (GADDS) 2D detector (Cu K_α radiation, no monochromator). The films surface morphology was investigated with a PicoSPM SFM from Molecular Imaging, using intermittent contact mode at room temperature. Statistical analysis of the SFM images were carried out by the software Mountains (Digital Surf). Additionally, current sensing SFM (C-SFM) measurements were performed to analyze the conducting character of the nanostructured films with an Omicron Instruments UHV AFM/STM system by standard contact mode with silicon SFM tips coated with a boron-doped diamond conducting film with $k = 2.8N.m^{-1}$(CDT-FMR, Nanosensors). The analysis of this image were carried out by the software WsXM from Nanotec[114]. TEM investigations were carried out with a 200 kV Jeol JEM-2010F field emission gun microscope equipped with an electron energy loss spectrometer (EELS) with a nominal energy resolution of 0.8 eV, and a Jeol JEM-2011 microscope equipped with an EDS. Energy filtered images were obtained using a 200 kV Cs corrected F20-SACTEM Tecnai microscope fitted with a GIF-Tridiem energy filter. Cross-sectional samples for TEM examination were prepared by the conventional cutting, gluing and grinding procedure, followed by a final Ar milling step down to perforation. Magnetic measurements have been performed using a superconducting quantum interference device (SQUID) magnetometer provided with a 7T magnet to check the properties of the LSMO layers. Electrical resistivity and magnetoresistance were obtained using a physical properties measurement system (PPMS, Quantum Design) equipped with a 9T magnet with a standard four-point probe method.

Chapter 3

Thickness dependence of magnetotransport properties in $La_{0.7}Sr_{0.3}MnO_3$ thin films

"If people never did silly things nothing intelligent would ever get done."
Ludwig Wittgenstein

3.1 Introduction

In heteroepitaxial growth, commonly, a lattice mistmach exists between the growing material and the substrate. In such cases, the first layers conform to the substrate and the film is strained. With increasing film thickness this strain will relax through the appearance of misfit dislocations, and the film properties should approach those of the bulk. A film under strain will have different properties compared to a strain-free film. For the case of manganite films, this behavior is generally correlated with the Mn-O-Mn bond angles and Mn-Mn distance changes. Because the physical properties of thin films are influenced by the mismatch strain between film and single crystal substrate, the control of the internal microstructure is essential in order to understand physical properties variations.

In the past few years, many papers concerning strain effects in manganite films have been published. Most of the reported studies correlate, both tensile and compressed strains, with a degradation in Curie temperature (T_c) of $La_{1-x}Ca_xMnO_3$ manganite thin films[16,81,126,172] and LSMO thin films[3,46,47,67,92,130,165].

In particular for LSMO films, the degradation of magnetoelectronic properties have also been checked following a dynamical way to manipulate macroscopic properties (resistivity and magnetization). Using piezoelectric substrates which allow a variation of the strain state of the film by applying a voltage at the piezoelectric substrate[161,187]. A relationship between the resistance change $\Delta R/R$ and the strain ϵ_{zz} in the LSMO film is derived, indicating that the relative change in the resistance is proportional to the induced strain in the LSMO film.

Similar results have been reported by Thiele et al.[160], using piezoelectric $Pb(Mg_{1/3}Nb_{2/3})_{0.72}Ti_{0.28}O_3$ substrates,where up to 19 K strain-induced shifts of the ferromagnetic Curie temperature T_c were found in $La_{0.7}Sr_{0.3}MnO_3$ ($t = 20nm$).

This interpretation seems to be reasonable and likely to be correct, but the mechanism based on strain alone may not be sufficient to account for all aspects of the experimental results such as the thickness and temperature dependencies of the magnetic and MR properties. In fact, magnetic disorder or loss of oxygen at interfaces, oxygen vacancies, chemical fluctuations or inhomogeneities and structural defects can also play an important role.

Starting from a fully strained $La_{0.7}Sr_{0.3}MnO_3$ thin film displaying almost bulk magnetic properties, and contrary to what has been previously reported, in this chapter we give evidences of a degradation on the magnetic behavior (T_c) of the CSD-LSMO thin films as thickness is increased and a fully relaxed state is approached. We try to give insight into the role that interfacial strain generation and interfacial strain accommodation play when manipulating thin film properties.

3.2 Results and discussion

In this chapter, the dependence of the LSMO films magnetoelectronic properties on the film thickness is presented for the nominal thickness (t) of 15, 24, 35 and 60 nm using the same growth conditions. The changes of the magnetoelectronic properties have been examined assuming a magnetoelastic model. It is found that these changes on magnetoelectronic properties cannot be explained merely by the film strain state.

3.2.1 Surface morphology

Varying the concentration of precursors solution we have obtained thin films with different thickness which were measured by using SFM on resistivity tracks, TEM cross-sectional analysis or SIMS depth profiles. Thus, thin films were deposited on STO substrates from four different solutions with concentrations of 0.2M (15nm expected thickness), 0.3M (24nm) , 0.4M (35nm) and 0.5M (60nm), yielding nominal thickness of 15, 24, 35 and 60 nm respectively (Fig.3.1).

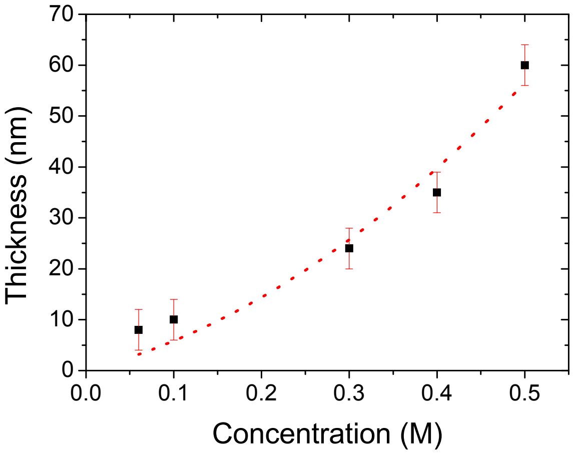

Fig. 3.1: *Thickness of the LSMO thin films as a function of the concentration of the precursor solution concentration.*

The surface morphology were examined by SFM. Fig.3.2 displays different stages of surface morphology evolution as film thickness increases for samples grown at 1000°C during 12h.

As explained in chapter 2, the LSMO film with thickness of 24 nm presents a process of formation of outcropped insulating nanodots on its surface with a size and distribution which can be controlled, see Fig. 3.2(b). Strikingly, for thickness above 35 nm these nanodots disappear from the LSMO surface (Fig.3.2c), leading to a flat surface with granular morphology with a root-mean-square[*](rms) roughness of $2nm$ and some holes which may cross the whole film down to the substrate. The morphology of the thickest film ($t = 60nm$) is shown in figure 3.2d. This film exhibits an enhanced rough surface with a rms roughness of $4nm$ and profuse vertical holes which may arrive down to the substrate as we demonstrate by cross-section TEM images (Fig.3.4). The observed holes are indicative that a dewetting process is happening in this stage. In this regard, we grow LSMO films for more extended processing times (15 hours) and at the same processing temperature. These films display parallepipedic like hole geometries characteristic of the dewetting process (not shown).

But, there are methodological reasons which limit the thickness range under study to 24-60 nm for films grown at 1000°C-12h, namely that for thicknesses lower than 24nm (0.3M), i.e, the films with a expected thickness of 15nm (0.2M) do not fully wet the substrate[40,95,145] (see fig. 3.2a) and for

---

[*] The rms were calculated in a region free of holes.

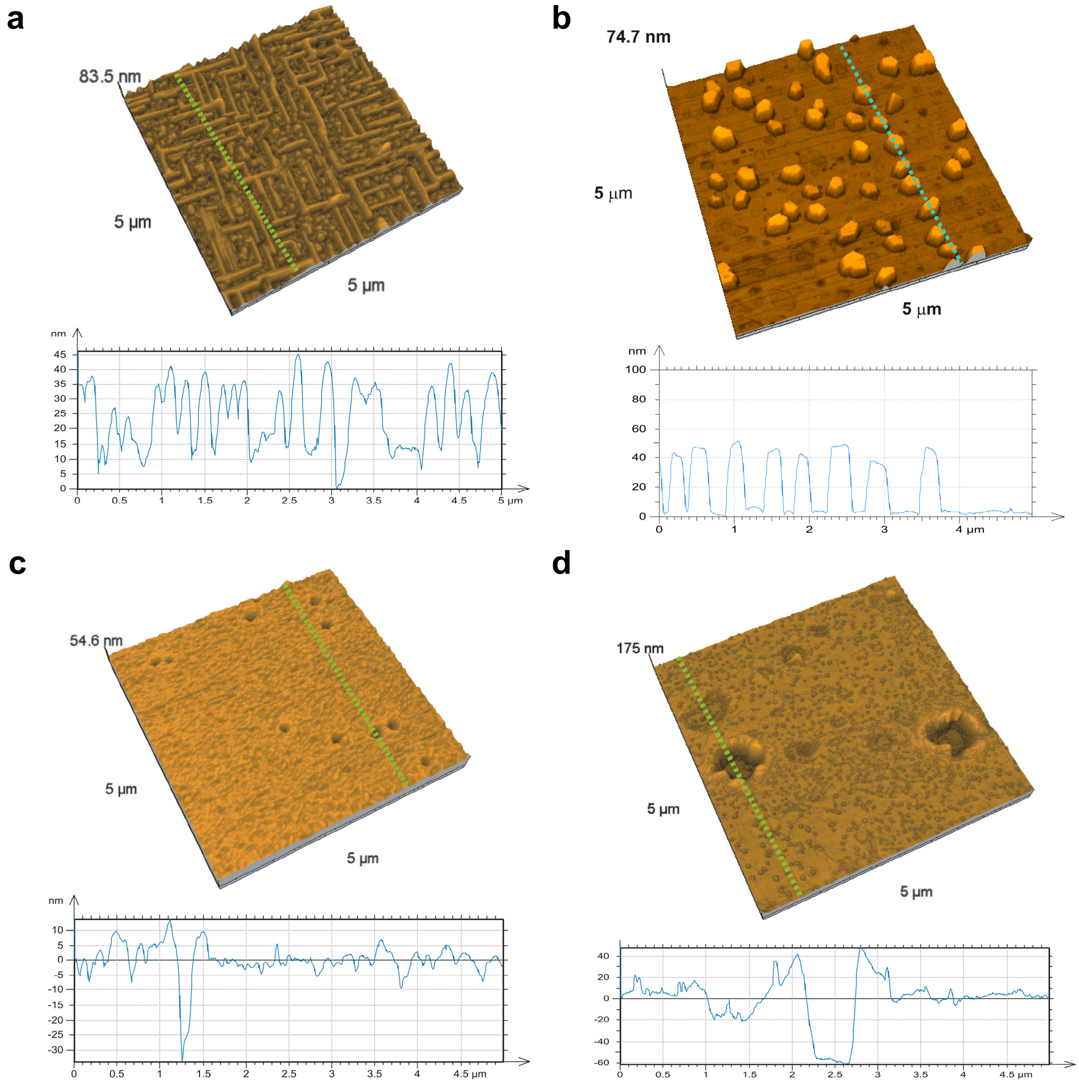

Fig. 3.2: *Surface morphology as a function of film thickness. Topographic ($5\mu m \times 5\mu m$) SFM images of LSMO thin films (1000°C-12h) on STO of different thickness: (a) dewetted film with expected thickness of 15nm, (b) 24 nm, (c) 35 nm and (d) 60 nm. The profiles have been obtained across the dotted line.*

thicknesses over 60 nm a saturation of the precursor solution concentration ($> 0.5M$) occur. In order to overcome the lower limit, i.e, to obtain films with lower thickness a reduced annealing temperature and shorter time were used. In this way, films with thickness of 10nm (0.1M) and 8nm (0.06M) were reached at 900°C during 1h (Fig.3.1).

On the other hand, the formation of holes, could be avoided by suitable thermal treatment of the resulting thin films. Thus, the 10nm and 8nm thick films exhibit a flat surface and free of holes with a rms roughness of 1 and 0.5nm, respectively (Fig.3.3). We note that the islands observed in the 8 nm thick film are not insulating, they remains metallic. This film will be used in chapter 5 where their metallic behavior is evidenced by conductive SFM (Fig.5.9).

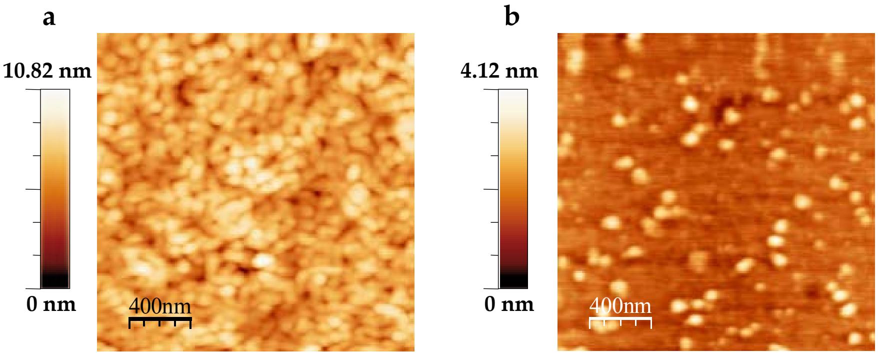

Fig. 3.3: *Topographic SFM images of LSMO thin films (900°C-1h) on STO of different thickness: (a) 8nm and (b)10 nm.*

Figure 3.4(a) and (b) show low magnification cross-sectional TEM images taken from two different areas within the sample where the pinholes observed by SFM are shown. In (a), it is observed that the pinhole gets down to the substrate, while in (b) there is still a certain amount of manganite on the substrates. The areas around the pinholes are a slightly thicker, in agreement with SFM measurements, and may present a high density of inclusions, see (b). The nature of these inclusions have also been studied by TEM and will be discussed later on in this chapter.

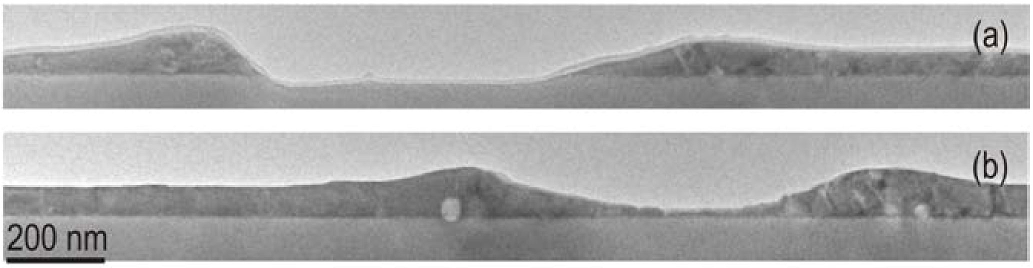

Fig. 3.4: *Low magnification cross-sectional TEM images of LSMO/STO for 60 nm film thickness recorded around two holes. Hole of LSMO film falling down to the substrate (a) and preserving a small thickness of LSMO (b).*

Pinhole formation is a typical feature of thin films grown by CSD which is associated to pyrolysis process of the metal organic precursors. These compounds usually display a coarsening process during high temperature growth, a process driven by the need to minimize the surface energy of the film. At the more advanced stages of the film evolution, the irregular shapes are transformed to parallelepipedic pinholes where the facets having the lowest energy develop clear energy[22,40,74]

3.2.2 Structural analysis

The crystal structure of the films has been investigated for different film thicknesses by using a diffractometer with CuK_α radiation in Bragg-Brentano geometry. Rather narrow rocking curves were measured for out-of-plane reflections of the films (FWHM 0.15°-0.3°). In Fig. 3.5a, we display $\theta - 2\theta$ scans around (003) reflections for several LSMO films for different thickness. We can observe a double peak corresponding with a $K_{\alpha 1}$ and $K_{\alpha 2}$ radiation. A shift of the peak position of the (003) reflection of the LSMO films, towards smaller angles, takes place as the thickness increases. The values of the out-of-plane parameter, c, of the different films as derived from diffraction patterns are plotted in figure 3.5b. The approach to obtain the c values is based in pseudo-voigt function fit (see experimental procedures, sec.7.4). The values obtained are in complete agreement with the values measured by reciprocal space maps (displayed next). Thus, in order to achieve a perpendicular film lattice parameter, $\theta - 2\theta$ scans may be chosen as a fast, simple and accurate method.

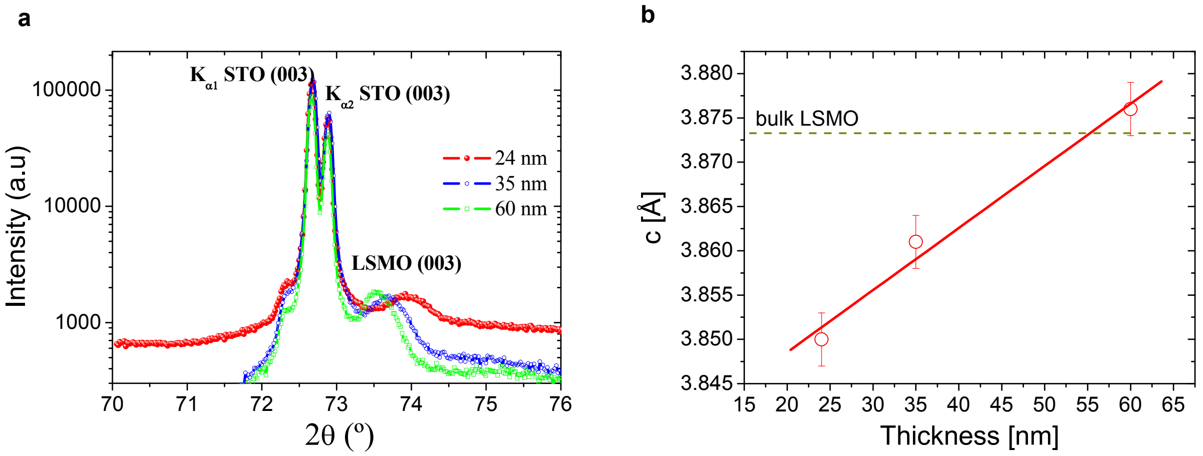

Fig. 3.5: *(a) X-ray diffraction pattern around (003) reflections for several thickness of LSMO films. (b) Plot of perpendicular film lattice parameter derived from $\theta - 2\theta$ scans.*

Since the cell parameter of bulk LSMO is 3.873 $\mathring{A}$[70], the obtained values for c indicate that LSMO films are under compressive strain in the out of plane direction for thick film of 24 nm (fully strained) and for 35 nm (partially relaxed), while for the thickest film ($t = 60nm$) a fully relaxed state is reached. In order to perform a direct measurement of the in-plane lattice parameters of LSMO films, another technique such as reciprocal space mapping is needed.

The reciprocal space maps of (103) LSMO and STO substrate are shown in figure 3.6 for films with different thickness. In-plane parameters are expanded from a value which match perfectly with that of the substrate, fully strained state, to a bulk LSMO film position. As we have obtained with

$\theta - 2\theta$ scans, out-of-plane parameters are reduced in relation to bulk parameter reaching a completely relaxed state for 60 nm thickness film. This very low thickness contrast with the thickness values reported in literature. For instance, *Maurice et al.*[102] report, for $La_{2/3}Sr_{2/3}MnO_3$ films grown on STO by pulsed-laser deposition (PLD), a relaxation above a thickness of $100nm$, while recovery of the parameter never occurs in the thickness range that they explored (up to $432nm$).

In figure 3.6d, we plot the lattice parameter values derived from reciprocal space maps where it is seen that the films evolve from a fully strained state to a fully relaxed state.

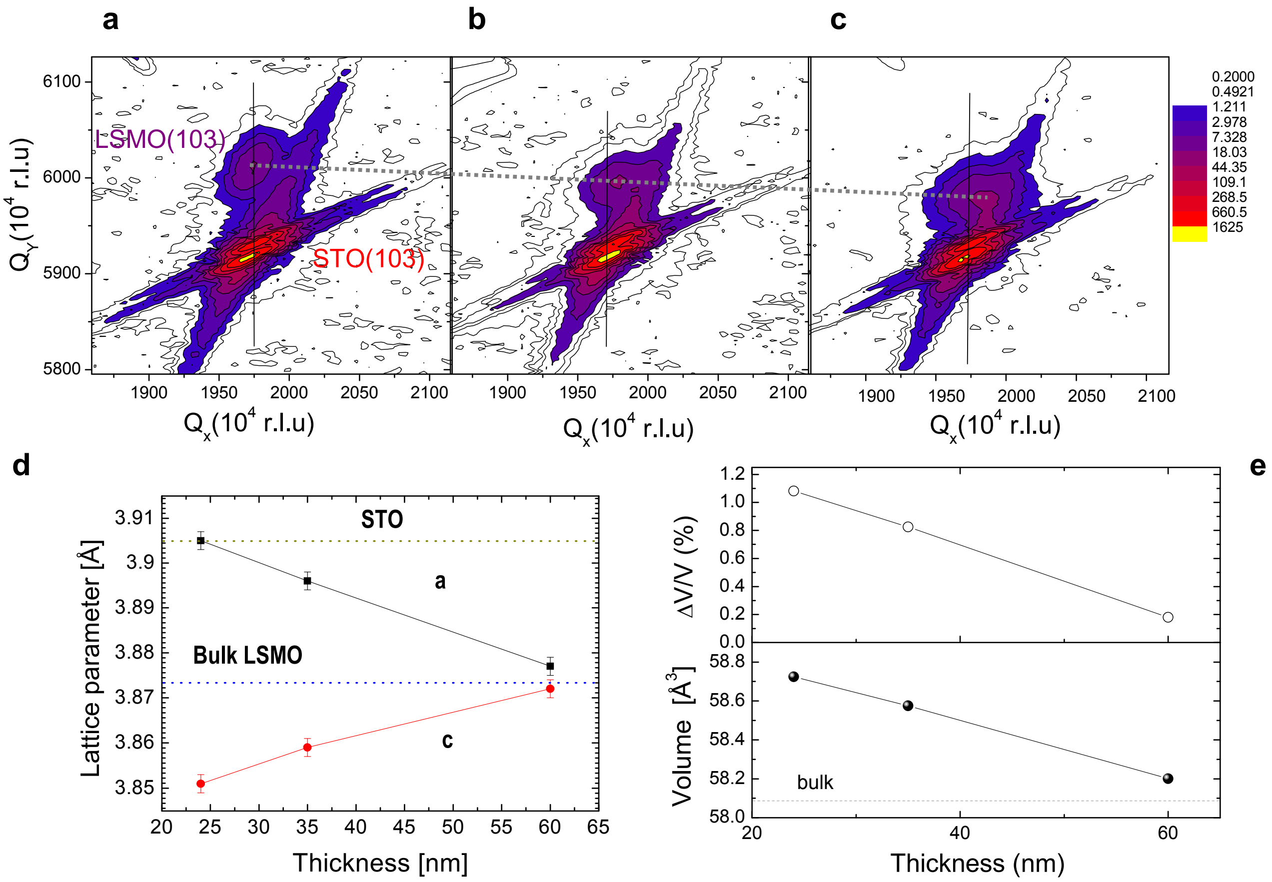

Fig. 3.6: *LSMO films X-ray reciprocal space maps recorded around (103) reflections. Data in (a) correspond to the thinnest film ($t = 24nm$) where the film peaks have the same Q_x value than the substrate, indicating a fully strained state with the substrate. (b) $t = 35nm$ thickness film showing a partially relaxed film state. (c) Thickest film $t = 60nm$ displaying a complete relaxed film state. The observed doublet is due to $K_{\alpha 1}$ and $K_{\alpha 2}$ radiation. According to the data, in-plane ($-\lambda/2Q_x$) and out-of-plane ($3\lambda/2Q_y$) lattice constants can be deduced (d). (e) Variation of unit-cell volume ($\Delta V/V$)(derived using bulk pseudocubic lattice parameter of $3.873\mathring{A}$[102]) and volume as a function of film thickness.*

Usually, the volume of the unit cell is conserved in the pseudomorphic transformation of the epitaxial thin films, as compared to the bulk, but in present case the determination of the variation of the unit cell volume in relationship to the unstrained value as a function of thickness indicates that the unit cell volume is not conserved (Fig. 3.6e). Thus, the thinnest film ($t = 24nm$) display a volume of $\backsim 1\%$ higher than the relaxed film ($t = 60nm$). Similar volume modification have been also reported by *Rao et al.*[131] in epitaxial $La_{0.8}Ca_{0.2}MnO_3$ thin films which varies its unit cell volume with the substrate as well as the film thickness.

3.2.3 Microstructural analysis

The 60 nm thick LSMO film has been investigated by cross-sectional TEM. The mean film thickness measured from the TEM images is 60 nm, which is in good agreement with the SFM measurements. Figures 3.7a and b are low magnification TEM images showing the general features of this sample. First, a high density of inclusions is observed (a rough estimation provides a $\backsim 5-6\%$ of the total area in the cross-sectional image), most of them placed at the LSMO/STO interface. The fact that they place themselves in the film/substrate interface was not observed by TEM for any inclusion in the 24 nm thick films (see chapter 2). The inclusions located at the LSMO/STO interface were well faceted and belong to the $(La,Sr)O_x$ phase. Fig.3.7d and e are HRTEM micrographs where the two different phases are shown. In Fig. 3.7d, a $(La,Sr)O_x$ inclusion, partly buried within the STO substrate is observed. In the image, the LSMO/STO interface has been indicated by arrows. An edge dislocation was found at the $(La,Sr)O_x/LSMO$ interface with Burgers vector[†] $\mathbf{b} = a_{LSMO}[100]$ with the extra plane in the LSMO side, also indicated in the image.

The matching distances of the $(La,Sr)O_x$ structure to the (100) and (001) LSMO planes are significantly smaller here than when located at the film surface. As shown in the inset, the dislocation introduces a slight distortion in the LSMO matrix around it, with a rotation of the (001) LSMO planes around the dislocation line. Rounded inclusions of the Ruddelsden-Popper ($R-P$) phase are also observed and found to be located, as for the case of thinner films, embedded in the LSMO matrix, see figure 3.7e. As expected, the $R-P$ inclusions did not introduce any evident distortion on the LSMO matrix and no dislocations were found in the $R-P/LSMO$ interface, thus, as in the 24nm thick films, they are believed to assist for stoichiometric balance of the system.

We will assume that, as a general trend, the inclusions found in the LSMO/STO interface are related to the formation of dislocations of the $\mathbf{b} = a_{LSMO}[010]$ type, as found for the cases shown in

---

[†] The Burgers vector of a dislocation is a crystal vector, specified by Miller indices, that quantifies the difference between the distorted lattice around the dislocation and the perfect lattice. Equivalently, the Burgers vector denotes the direction and magnitude of the atomic displacement that occurs when a dislocation moves.

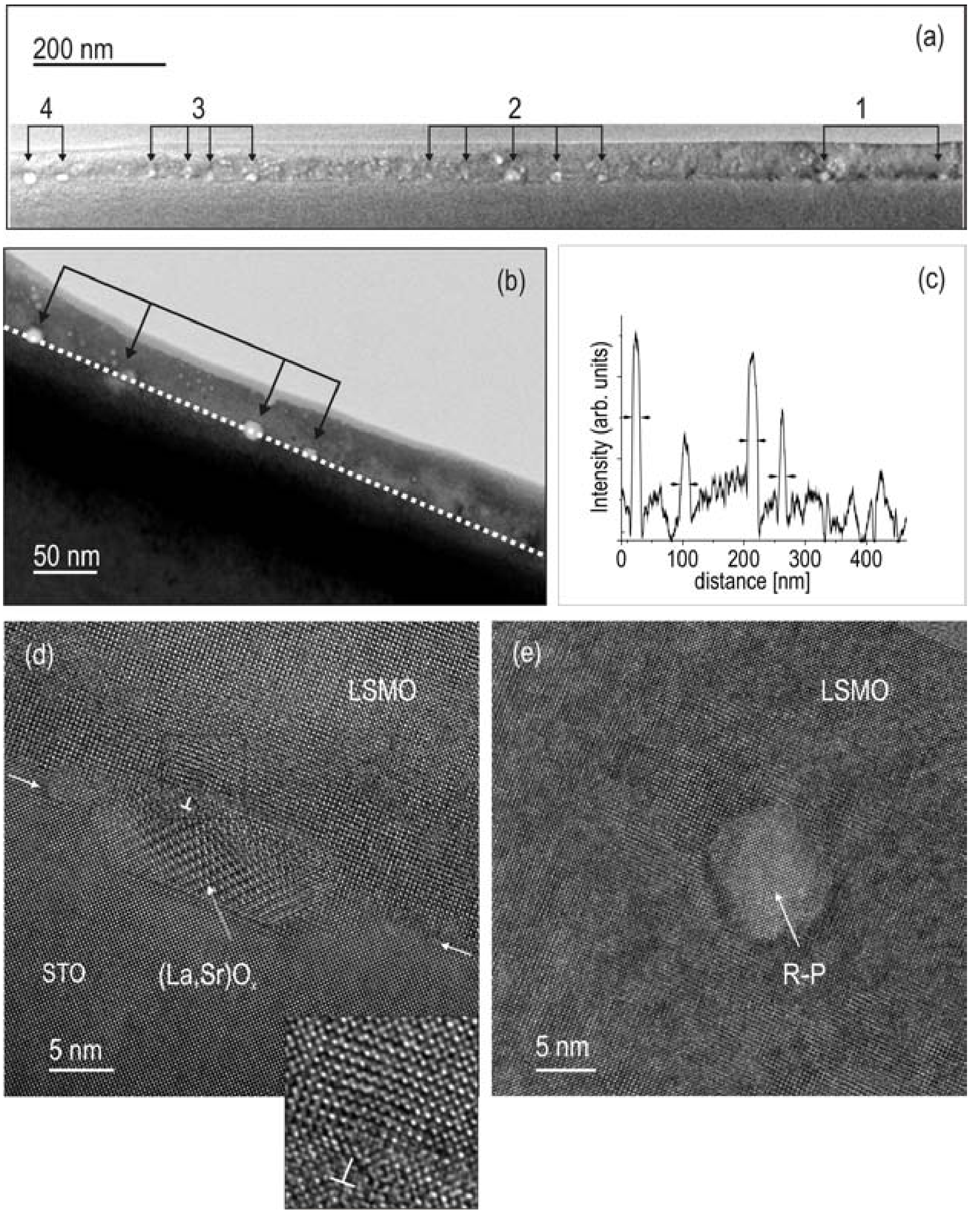

Fig. 3.7: *(a) and (b) are low magnification images of the 60 nm thick LSMO film showing the high density of inclusions. The inclusions located at the LSMO/STO interface, which are susceptible of contributing to the misfit relaxation of the film, are indicated by arrows. The weight of the inclusions in (b) is measured in the intensity profile of image (c). HRTEM images showing the two different types of inclusions are shown in (d) and (e). The interface between film/substrate is indicated with arrows, also the presence of dislocations is indicated, if any. An enlarged view of the distortion introduced in the LSMO lattice parameter by the dislocation with* $\mathbf{b} = a_{LSMO}$*[100] in (d) is shown in the inset.*

figure 3.7d. Then, the calculated distance for full relaxation of the LSMO film between dislocations with such Burgers vectors is $S_{100\%relax} = |b|/\epsilon = 48nm$, where ϵ is the strain in the $LSMO/STO$ interface.

Experimentally, the mean distance between inclusions in the interface can be measured from the areas where inclusions are more clearly observed at this low magnification image, see the sets of inclusions indicated by arrows in figure 3.7a in the areas labeled as 1,2,3 and 4. A measure of the particle dimensions has been performed by looking at the profile of intensities of the bright field images, as in the case of the profile of the interface in (b), shown in (c). The mean distance between inclusions has been measured to be 57nm. This rough calculation indicates that, despite the fact that full relaxation only by this relaxation mechanism has not been proved, a large amount of stress may be released in this way and so, this must be the main strain release mechanism operating in this particular film.

The phenomena of composition fluctuation have been addressed in other manganite compounds. For instance, *Chen at al.*[28] reported formation of Mn_3O_4 in $La_{1-x}MnO_{3\delta}$ films, *Gorbenko*[62] concluded that inclusions of MnO_x formed in the $(La,R)_{1-x}A_xMnO_3$ ($R = Pr, Nd$ and $A = Ca, Sr$ etc.) films with a small excess of Mn, whereas Mn_3O_4 formed with large excess of Mn, *He et al.*[75] also observed MnO phase in stoichiometric $La_{0.7}Ca_{0.3}MnO_3$ films on $SrTiO_3$ and $NdGaO_3$ substrates and *Lu et al.*[99] found two kinds of secondary phases in $La_{0.7}Ca_{0.3}MnO_3$ grown on STO and LAO substrates. However, inhomogeneous structures in the $La_{1-x}Sr_xMnO_3$ thin films are rarely observed. To our knowledge, the unique case reported are based in nano-agglomerates with a large Mn/La ratio embedded in a $La_{0.8}Sr_{0.2}MnO_3$ thin film[188,189] grown by using laser molecular beam epitaxy (laser MBE). Unfortunately in these articles the microstructure-property relationship has not been addressed.

3.2.4 Magnetic properties

The magnetic properties of the LSMO films were measured by SQUID magnetrometry. Magnetization dependent temperature is displayed in figure 3.8a for different thickness of the films. As thickness increases, the Curie temperature (T_c) decreases and the ferromagnetic to paramagnetic transition becomes more abrupt. This is more clearly observed by comparing the positions of minimum and the shape of the derivative of the magnetization, $dM(T)/dT$, shown in the inset in figure 3.8a.

In figure 3.8b, isothermal magnetization curves with a low coercive field, as correspond to thin films, are presented . An estimation of the saturation of magnetization (M_S) has been done from the isothermal magnetization curves by fitting the high field part with the law of approximation to saturation[41]:

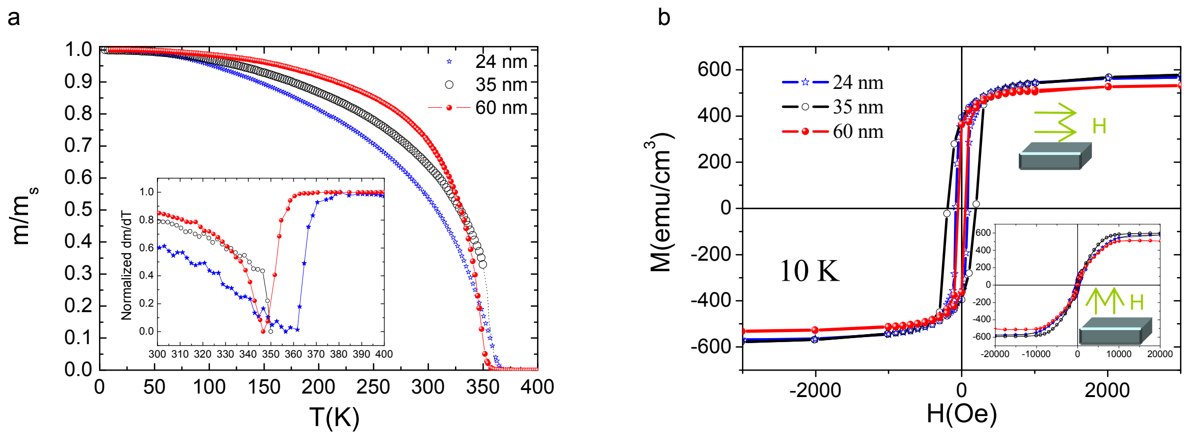

Fig. 3.8: *Thickness dependence of ferromagnetic properties of LSMO thin films on STO. (a) Temperature dependence of the magnetization taken at 0.1T in-plane applied magnetic field. Inset display the derivatives of the magnetization as a function of temperature. (b) Isothermal magnetization curves measured at 10K with magnetic field applied parallel and perpendicular (inset) to the LSMO film. The diamagnetic contribution to magnetization (not shown) has been attributed to the substrate and has been subtracted.*

$$M = M_S\left(1 - \frac{a}{H^2} + \chi H\right) \tag{3.1}$$

Where a is related to the magnetic anisotropy, χ is the high field differential magnetic susceptibility and H is the magnetic field. A decrease of 8% (16%) of in-plane (out-of-plane) saturation magnetic moment is observed for the thickest film ($60nm$) while the thinnest and intermediate thick films preserve the bulk magnetization ($M_s = 590emu.cm^{-3}$). The decrease in M_s of $\backsim 7\%$ can be correlated with the non magnetic inclusions within the LSMO matrix determined by TEM for the 60 nm thick film, which are initially computed in the total volumen of the film.

Thus taking into account the volume of the inclusions, we can conclude that M_s remains invariable with the film thickness. On the other hand, a clear dependence is evidenced between T_c and thickness of the films . This correlation will be discussed in the next subsection.

3.2.5 Analysis of strain dependence of T_c

Commonly, the film strain state can be correlated with T_c. The shift of T_c resulting from an elastic tetragonal deformation of the cubic cell can be expressed according to the Millis model[109] as:

$$T_c(\epsilon_B, \epsilon_{JT}) = T_c(0,0) \times \left[1 - \alpha\epsilon_B - \frac{1}{2}\beta\epsilon_{JT}^2\right] \tag{3.2}$$

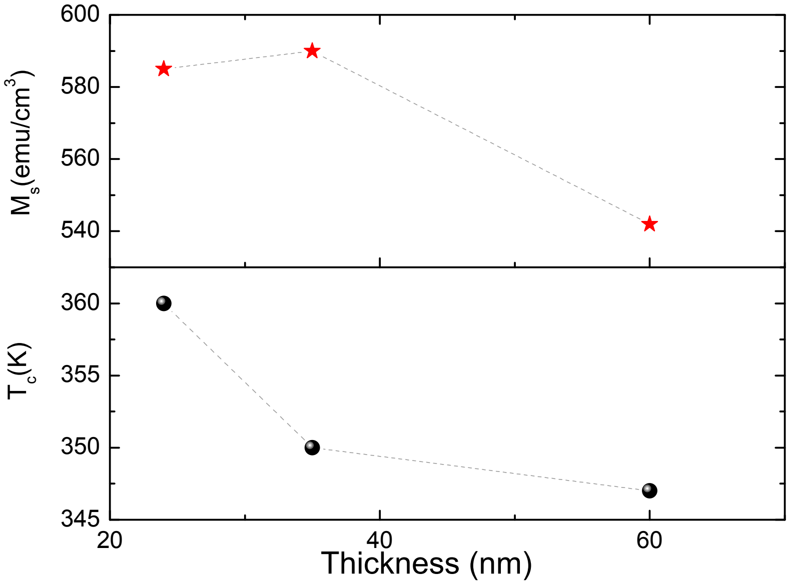

Fig. 3.9: *Thickness dependence of the saturation magnetization (stars) and Curie temperature (bullets).*

where $T_c(0,0) = 370$K is the Curie temperature of bulk LSMO, $\alpha = (1/T_c)[(dT_c)/(d\epsilon_B)]$, $\beta = (1/T_c)[(dT_c^2)/(d\epsilon_{JT}^2)]$, ϵ_B is a bulk strain (the so called hydrostatic term):

$$\epsilon_B = \frac{1}{3}\left(\epsilon_{xx} + \epsilon_{yy} + \epsilon_{zz}\right) \tag{3.3}$$

and ϵ_{JT} being the biaxial strain (Jahn-Teller term):

$$\epsilon_{JT}^2 = \frac{1}{4}\left(\epsilon_{xx} + \epsilon_{yy}\right)^2 + \frac{1}{16}\left(2\epsilon_{zz} - \epsilon_{xx} - \epsilon_{yy}\right)^2 \tag{3.4}$$

ϵ_{xx}, ϵ_{yy}, and ϵ_{zz} denote the relative length changes in x, y and z direction of the film, with z being perpendicular to the film plane. For a cubic lattice ($\epsilon_{xx} = \epsilon_{yy}$), there is no linear term in ϵ_{JT}.

Two these terms have opposite effects upon T_c. Eq.(3.2) implies that whereas the biaxial distortion always leads to a reduction of T_c, this is not the case for the bulk distortion, which can contribute either with a positive or a negative value, depending on the sign of the the bulk strain (ϵ_B) along the different film directions (see also Eq. (3.3)). A hydrostatic compression ($\epsilon_B < 0$) will tend to increase the hopping and thereby reduce the electron-lattice coupling, inducing an increase in both the conduction band width and T_c. While, a biaxial strain increases the energy differences between the e_g levels imposed by the Jahn-Teller which reinforce the electrons tendency to become more localized and thus decreasing T_c[51].

A summary of the strain values determined from the lattice parameters derived from RSMs is reported in table 3.1. As film thickness increases the elastic relaxation is increased recovering the bulk lattice parameters values and an undistorted cell.

Thickness (nm)	$a(\mathring{A})$	$c(\mathring{A})$	$\epsilon_{xx}(\%)$	$\epsilon_{zz}(\%)$	$\epsilon_B(\%)$	$\epsilon_{JT}(\%)$
24	3.905	3.851	0.826	-0.568	1.084	-1.138
35	3.896	3.859	0.594	-0.361	0.827	-0.779
60	3.877	3.872	0.103	-0.026	0.180	-0.105

Tab. 3.1: *In-plane and out-of-plane lattice parameters (a,c) deduced from X-ray reciprocal space maps and* $\theta-2\theta$ *analysis of LSMO films with varying thicknesses from 24 to 60 nm. All films were grown under the same conditions (1000ºC during 12 h). In-plane and out-of-plane strain* (ϵ_{xx},ϵ_{zz}) *were derived using bulk lattice parameter* $a_{LSMO} = 3.873$ Å. *The hydrostatic volume strain* (ϵ_B) *associated to volume conservation and the Jahn-Teller strain* (ϵ_{JT}) *are also indicated.*

In figure 3.10a a three-dimensional plot displaying the changes of T_c with ϵ_B and ϵ^2_{JT} is shown, where ϵ_B and ϵ^2_{JT} parameters were derived from X-ray reciprocal space maps displayed in figure 3.6. A decrease of T_c with hydrostatic volume strain (ϵ_B) and the square of $Jahn-Teller$ strain (ϵ^2_{JT}) is observed. In order to compare these results with those reported in the literature, we have plotted in figure 3.10b the dependence of our experimental values of T_c as a function of film thickness together with the expected T_c values calculated using the magnetoelastic Millis model (Eq.(3.2)), using our experimental ϵ_B and ϵ^2_{JT} parameters and the experimental α and β constants reported in the literature.

Typical values for α and β in manganites have been predicted to be around 6 and 1400, respectively[109]. However a considerable spread of experimental values exists in the literature. For instance, *Tsui et al.*[165] report for $La_{0.7}Sr_{0.3}MnO_3$ films with a thickness of 25 and $50nm$ grown on several types of substrates, the constant values of $\alpha = 2$ and $\beta = 70$, while *Ranno et al.*[130] report $\alpha = 2.2$ and $\beta = 2100$ for films of LSMO on STO and thickness of 30, 60 and $80nm$, finally *Adamo et al.*[3] report $\alpha = 1.55$, $\beta = 1460$ for films $22nm$ thick on different crystalline substrates.

In this way, for the fully strained film ($t = 24nm$) the drop of the T_c in relation to the bulk value, 2.7%, can be due to the strain state of the film. Accordingly with the theoretical magnetoelastic model (for this films $\epsilon_B > 0$), a tensile stress should reduce T_c, as well as almost experimental results[3,46,67,92,130,165] where films under tensile stress show a considerable reduction of T_c.

However, for the partially and fully relaxed films ($t = 35nm$ and $t = 60nm$) we would expect an increase of T_c as compared to the fully strained ($T_c = 360K$) film. Instead, for both of them T_c drops ($350K$ and $347K$, respectively).

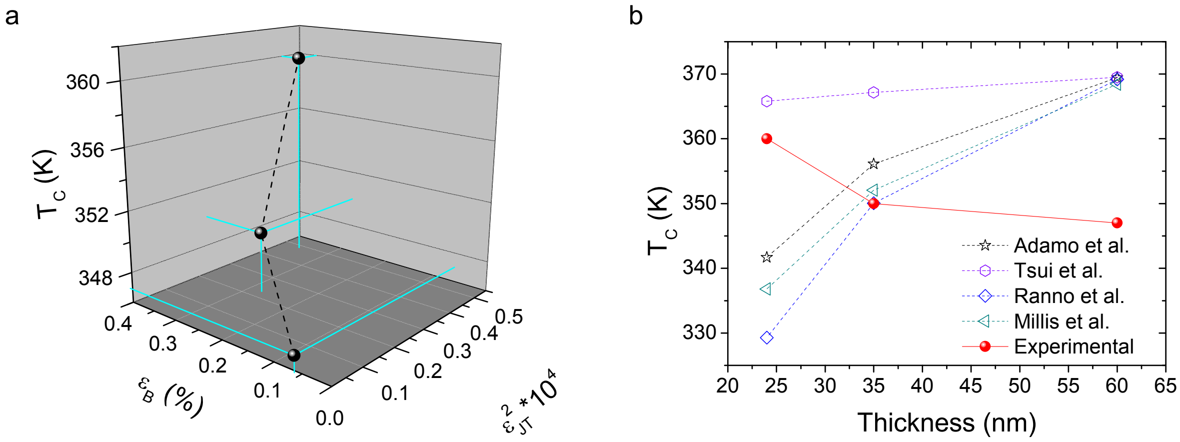

Fig. 3.10: *Strain dependence in temperature of Curie. (a) Experimental values obtained by using SQUID magnetometry as a function of hydrostatic volume strain (ϵ_B) and the square of $Jahn-Teller$ strain (ϵ_{JT}^2). (b) Dependence of T_c as a function of film thickness for our experimental results (bullets) and following the model of Millis*[109] *by using different α and β constants: Tsui et al.*[165]*, Ranno et al.*[130] *and Adamo et al.*[3] *(see text for constant values).*

The analysis of the dependence of the Curie temperature on the elastic deformation of the CSD films has revealed that the elastic deformation of the manganite lattice can describe the response of the fully strained films ($24nm$), whereas for partially and fully relaxed films ($35nm$ and $60nm$) other effects (magnetic disorder or loss of oxygen at interfaces, oxygen vacancies, chemical fluctuations) should be considered for the properties of the strained films. In this regard, *Maurice et al.*[103] suggest the structural disorder as an explanation to the degradation of T_c in relaxed LSMO films. Furthermore, the results showed in this chapter are far from the trends expected from the magnetoeleastic model of Millis using the constants reported experimentally by others authors, an opposite trend is found concerning the variation of T_c with the film strain.

The discrepancy with the magnetoelastic model[109] has been also reported in LCMO thin films[1,16,81] and it has been attributed to chemical or electronic phase separation effects.

To our knowledge, in the case of $La_{0.7}Sr_{0.3}MnO_3$ thin films, which generally does not display appreciable phase separation, the discrepancy with the model of Millis has not been addressed before. A possible explanation of this evolution with thickness could be caused by the existence of structural and chemical disorder originated by the high density of inclusions embedded within the LSMO matrix.

3.2.6 Transport properties

The transport properties were measured in the four point technique using a PPMS setup. The temperature dependence of the resistivity in zero magnetic field for thin LSMO films with variable thicknesses between 24 and 60 nm is given in Fig. 3.11a. The films show a bulklike metallic behavior over the whole temperature regime in agreement with Ioffe-Regel criterion $\rho \leq (2\pi hc)/(4e^2) \approx 8.10^{-3}\Omega.cm$[67], which expresses the fact that the mean free path exceeds the distance between two neighbouring atoms. Taking into account this criterion the metallic behavior is displayed even beyond the metal-insulator transition temperature (T_{MI}). Nevertheless it is called a metal-insulator transition because dR/dT changes its sign. Following the latter criterion we have calculated T_{MI} as the maximum in the differential resistivity $d\rho/dT$ (inset Fig.3.11) which in our case match with the maximum of the magnetorresistance at 5T, displayed in figure 3.11b. The shape of the MR peak narrows and moves to higher temperatures from 322K at 24nm to 358K at 60nm. At the same time the maximum MR value increases from 11% at 24nm to 27% at 60nm.

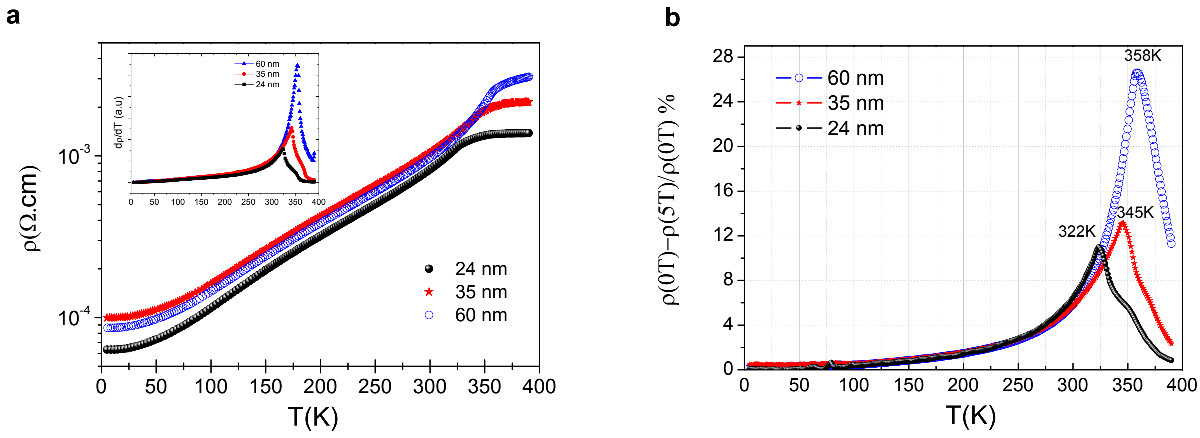

Fig. 3.11: *Transport properties of LSMO films. Temperature dependence of the resistivity (a), of the* $d\rho/dT$ *(inset) and magnetorresistance at 5T (b) for films of different thicknesses.*

This fact can be correlated with the decrease of T_c as a film thickness increase. In general, since the resistivity of the paramagnetic phase strongly increases on decreasing T, whereas that of the ferromagnetic phase decreases, the CMR is larger and larger as T_c is smaller and smaller, at least for a given doping level. For instance, a resistance ratio $R(0)/R(6T) > 10^3$ was observed in a thin film of $La_{0.67}Ca_{0.33}MnO_3$ with $T_c = 80K$[86], whereas in a film with the same composition and $T_c = 260K$ this ratio is only of about 4[150].

The residual resistivity at 5K is for all three films similar to those previously reported for $La_{0.7}$-$Sr_{0.3}MnO_3$ single crystal films[166], i.e, $\rho_{5K} < 10^{-4}\Omega.cm$. But, when the LSMO film thickness increases, the resistivity increases over the whole temperature range, increasing also the meal-insulator temperature and the resistivity around this point.

To summarize, the magnitudes characterizing the transport properties (ρ^{390K}, T_{MI} and MR_{5T}) are displayed in figure 3.12. The plot features the increase of transport properties as the thickness of the LSMO film increases. The increase of ρ^{390K} indicates a increase of the disorder in the film. Because colossal magnetoresistance in these materials is closely related to the observed nanometer- and micrometer-scale inhomogeneities, very likely the enhanced MR can be controlled with these inhomogeneities.

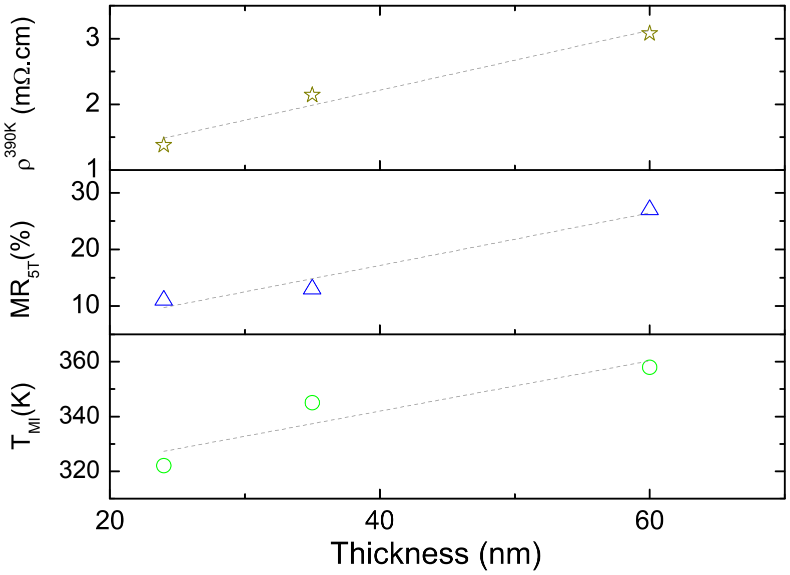

Fig. 3.12: *Thickness dependence of the resistivity at 390K (stars), magnetorresistance at 5K (open triangles) and metal-to-insulator transition temperature (open circles). The 390K temperature resistivity gives an indication of the disorder in the film.*

Similarly to the Curie temperature, the metal-insulating transition temperature (T_{MI}) has been modeled as a function of the strain film[6,100] using the equation:

$$T_{MI}(\epsilon_B, \epsilon_{JT}) = T_{MI}(0,0) \times \left[1 - \alpha\epsilon_B - \frac{1}{2}\beta\epsilon_{JT}^2\right] \tag{3.5}$$

where $T_{MI}(0,0) = 370\text{K}$, $\alpha = (1/T_{MI})[(dT_{MI})/(d\epsilon_B)]$ and $\beta = (1/T_{MI})[(dT_{MI}^2)/(d\epsilon_{JT}^2)]$.

In this way, based on strain arguments, T_{MI} is expected to be lower for $24nm$ than for 35 and $60nm$ thick films, as we can see in figure 3.13, which display the experimental data derived from resistivity curves together with the theoretically expected values following equation(3.5) and the α

and β constants reported by others authors.

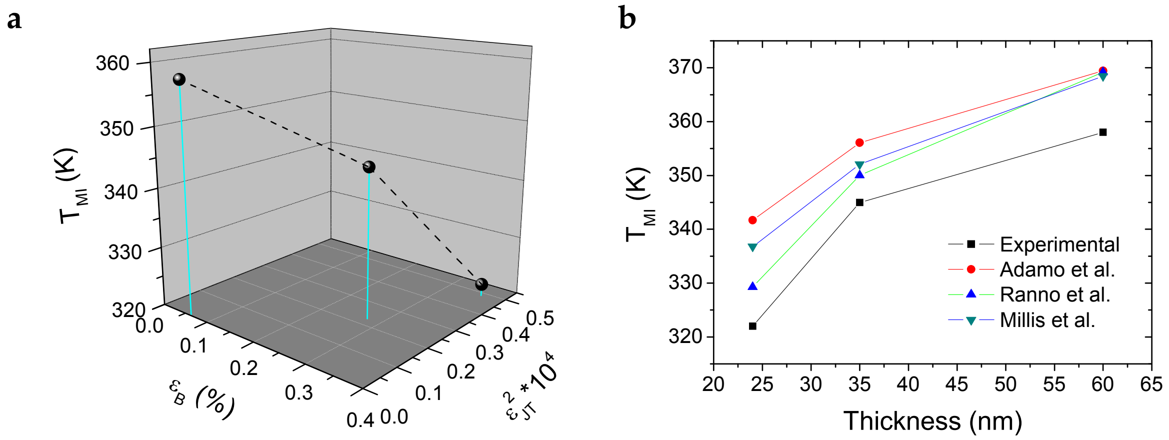

Fig. 3.13: *Strain dependence of the metal-insulator transition temperature. (a) Experimental values obtained derived from resistivity curves as a function of hydrostatic volume strain (ϵ_B) and the square of $Jahn - Teller$ strain (ϵ^2_{JT}). (b) Dependence of T_{MI} as a function of film thickness for our experimental results (bullets) and following the model of Millis*[109] *by using different α and β constants: Angeloni et al.*[6]*, Ranno et al.*[130] *and Adamo et al.*[3]

In this case, and contrary to the trend observed for T_c, T_{MI} decreases with the film strain. This agrees with the experimental results reported by *Rao et al.* in LCMO thin films, who showed that both T_{MI} and strain exhibit a strong thickness dependence, however, no clear correlation between the strain states and T_c could be made[131]. It was suggested that chemical inhomogeneities and disorder in the films were responsible for the lack of correlation. Our microstructural study shows that the secondary phases and the disorder play indeed a role in the transport and magnetic properties of $La_{0.7}Sr_{0.3}MnO_3$ films.

3.3 Summary

In summary, we have studied epitaxial single crystal LSMO thin films on STO substrate grown by CSD method as a function of the LSMO film thickness to evidence the connections between structure, microstructure and physical behavior. X-ray diffraction has shown that for CSD-grown LSMO films the completely relaxed state is achieved at very low thickness ($60nm$). Self-nanostructured LSMO films consisting of $(La, Sr)O_x$ islands and Ruddelsden-Popper inclusions within an epitaxial matrix of high crystalline perfection, are shown to plastically relax the films at these thickness. Curie and metal to insulator transition temperatures show film thickness dependence, but they do not show correlation with strain states. The analysis of the dependence of the Curie temperature on the elastic deformation can only describe the response of the fully strained films ($24nm$), whereas for partially and fully relaxed films ($35nm$ and $60nm$) other effects should be considered. On the other hand, the T_{MI} dependence with thickness could be explained by using lattice parameters arguments alone, while the MR^{5T} and ρ^{390K} evidenced an influence of structural and chemical disorder in the film for the thickest and relaxed films. The lack of a full correlation between the strain state, T_c and T_{MI} suggests that these transition temperatures are influenced in a different way by other factors, such as chemical inhomogeneity and structural disorder in the film.

3.4 Methods

LSMO films were deposited on (100) $SrTiO_3$ (STO) substrates by spin coating at 6000 rpm for 2 min and annealed at temperatures in the range 900-1000°C under flowing oxygen gas for different annealing times up to 12 h. X-Ray diffraction reciprocal space maps were obtained using a Bruker D8 Advance difractometer equipped with a four-angle goniometer and a general angle diffraction detection system (GADDS) 2D detector (Cu K_α radiation, no monochromator). TEM investigations were carried out with a 200 kV Jeol JEM-2010F field emission gun microscope and a Jeol JEM-2011 microscope. Cross-sectional samples for TEM examination were prepared by the conventional cutting, gluing and grinding procedure, followed by a final Ar milling step down to perforation. Magnetic measurements have been performed using a superconducting quantum interference device (SQUID) magnetometer provided with a 7T magnet to check the properties of the LSMO layers. Electrical resistivity and magnetoresistance were obtained using a physical properties measurement system (PPMS, Quantum Design) equipped with a 9T magnet with a standard four-point probe method.

Chapter 4

Heating effects in $La_{0.7}Sr_{0.3}MnO_3$ thin films

> *"Laws were made to be broken."*
>
> Christopher North

4.1 Introduction

Resistive bistable switching can be used as a source of non-volatile resistive random access memories (RRAM) and hence its development has generated a large interest[32,63,104,115,135,157,182].

Several types of oxides, such as $SrTiO_3 : Cr$[84], CuO[29], NiO[25], TiO_2[34,182] and Al_2O_3,[24] have been shown to display electrically switchable resistive properties and multiple microscopic mechanisms have been proposed based either on redox processes involving cation or anion migration[8], on the formation/rupture of conducting nanoscale filaments[36,97,134], oxygen diffusion[115], Mott metal-insulator transition[82,135],variable Schottky barrier[165] or charge trapping at interfacial sites[119].

In manganites the situation is even more complex and conflicting interpretations have been proposed. It has been suggested that bistable resistivity could be an intrinsic phenomenon associated to homogeneous Joule effect self-heating,[63] which would be therefore enhanced in measurements performed at high current densities (J) and which would depend on the sample dimensions and shape (bulk, thin film) because the thermal heating and transfer would be deeply modified.

In order to elucidate the parameters controlling the resistance bistability, several manganite compositions have been investigated.[7,11,19,21,31,33,105,121,137,151,179] However, the influence of composition, intrinsic transport properties and contact heating has not been clarified yet. Bistable resistivity in manganites of different compositions has been claimed to occur for polycrystalline ceramic, single crystal and thin film materials where the self-heating effect and the electrical contacts influence might be very different. The intrinsic or extrinsic origin of the Joule heating effect remains therefore uncertain. In the case of the most robust ferromagnetic metal among the manganite series, $La_{0.7}Sr_{0.3}MnO_3$, which does not display any appreciable phase separation, bistable resistivity has been reported for thin films. However, it has not been clarified if it arises from Joule self-heating[32,80] or it is an interface induced phenomenon.[96,180]

4.2 Determining the heating-free conditions

In the present chapter, we report on macroscopic transport measurements and local electrical behavior at the nanoscale, obtained by conducting Scanning Force Microscopy (C-SFM) under low and high values of dissipative contact power ($DCP = \rho_c \times I^2 = R_c \times A_c \times I^2$), where ρ_c is the contact resistivity, R_c is the contact resistance, A_c is the contact area and I is the current threading the sample. We will show that, while high DCP values induce hysteretic behavior, linear and non-hysteretic E(J) characteristics are obtained up to high J values ($J \backsim 5 \times 10^4 Acm^{-2}$) when low DCP are used. Moreover, beyond this limiting value only a moderate rise in temperature is induced without reaching a bistable resistivity regime. We suggest that to analyze Joule self-heating phenomena and if, eventually, bistable resistivity exists, electrical contact heating should be minimized to avoid any unsuitable nuisance in the thermal transfer process.

We note that to make easier the manuscript reading, throughout the manuscript the experimental data will appear as they are commonly represented, i.e. $E(J)$ characteristics are shown for macroscopic measurements whereas current versus voltage (I-V) curves are used to illustrate the local measurements. The contact resistance in the later is then defined as the inverse slope of the linear region of the I-V curves.

4.2.1 Results and discussion

The quality of the grown LSMO films can be derived from data in Figure 4.1, where the zero and 5 T field resistivity as well as the magnetic moment at 5 mT after a field cooling process are shown. The figure inset displays the corresponding magnetoresistance and the magnetization derivative, dm/dT, with the typical peak at T_c. The values of resistivity, magnetoresistance and T_c are very similar to those observed in LSMO films grown by physical vapour deposition techniques, such as sputtering or pulsed laser deposition, leading us to conclude that a similar epitaxial quality is achieved with films grown by our CSD approach.

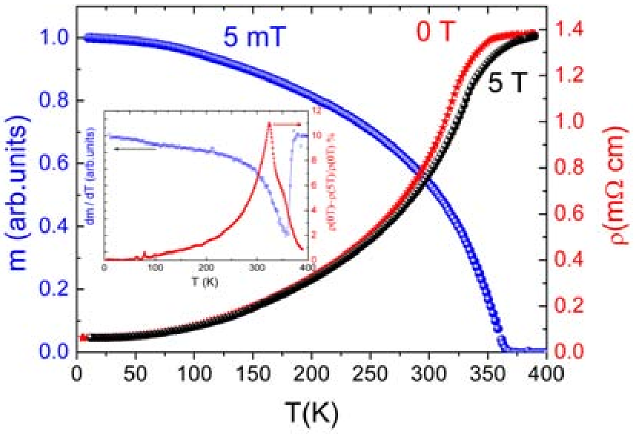

Fig. 4.1: *Main panel: temperature dependence of the resistivity under zero and 5T magnetic fields (right axis) and the magnetization in a magnetic field of 5 mT (left axis). Inset: Temperature dependence of the magnetoresistance at 5 T and the magnetic moment derivative respect temperature dm/dT.*

Joule self-heating as a source of resistance bistability is a phenomenon which has been extensively investigated in normal metals and superconductors[63] and has been shown to result from a unique balance between heat release and heat transfer to the thermal bath. Provided the unit volume heat generation is determined by $Q(T) = \rho(T)J^2$, a bistable resistance of thermal origin can occur only if two particular J values exist for which the corresponding Q(T) values can be properly transferred to the thermal bath (via the anchored substrate) and hence a new isothermal steady state can be reached. Therefore to achieve bistable resistance of thermal origin one should perform electrical transport measurements at enhanced Joule self heating conditions, i.e. at J values as high as possible. This poses the problem of electrical contact optimization which needs to be properly addressed and which deeply differs for thin film and bulk sample measurements. To analyse the importance of the contacts, we have carried out macroscopic transport measurements in LSMO thin films under different current configurations and electrical contact qualities, i.e. contacts with different DCP values.

Figure 4.2(a) presents a typical voltage-current characteristics curve measured in a standard non-lithographed film with a DCP of 17 Wcm^2, a common situation on macroscopic transport studies of manganites. The curves are hysteretic and strongly temperature dependent (not shown). This result reminds the well known behavior observed in critical current measurements of high current density superconducting materials where, in order to obtain reliable measurements and avoid unde-

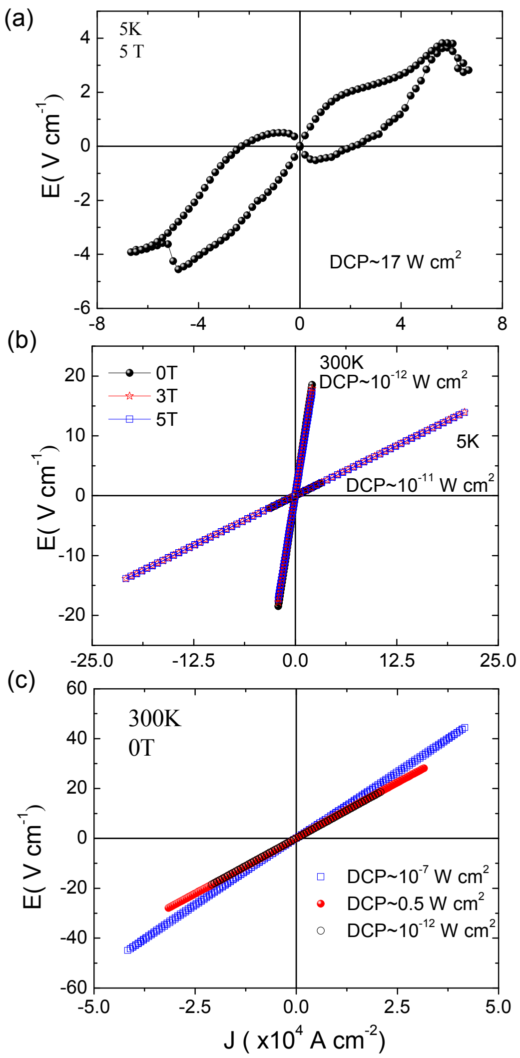

Fig. 4.2: *$E(J)$ characteristic curves measured in a four points configuration for LSMO films with (a) high resistivity contacts (non lithographed film, $DCP \backsim 17\ Wcm^2$); (b) low resistivity contacts at 5K ($DCP \backsim 10^{-11}\ Wcm^2$) and 300K ($DCP \backsim 10^{-12}\ Wcm^2$) in a lithographed film. Note that data for different field values overlap at this scale; (c) for different dissipative contact powers in lithographed ($DCP \backsim 0.5\ Wcm^2$, ● and $DCP \backsim 10^{-12}\ Wcm^2$, ○) and non-lithographed ($DCP \backsim 10^{-7}\ Wcm^2$, □) films. The maximum Joule heating density achieved in these measurements is in the range of $Q \backsim 2 \times 10^{12}\ Jm^{-3}$.*

sired thermal heating, the use of low DCP is mandatory[48,65]. Clarifying if the $E(J)$ characteristics of manganites are as well affected by a low DCP implies further verification. Thus, to discern between the effects of intrinsic film self-heating ($\backsim \rho J^2$) and contact heating ($\backsim DCP = \rho_c \times I^2$) we have increased J while decreasing I across the films by lithographing narrow stripes, presenting well defined widths and ρ_c, as those shown in the optical micrographs of Fig. 4.3(a) and 4.3(b). Simultaneous topographic (Fig.4.3(c)) and C-SFM (Fig.4.3(d)) images taken on one stripe are also shown to illustrate that the conducting character of the LSMO is preserved in the lithographed region. Figure 4.2(b) shows a typical set of $E(J)$ curves for a low contact resistivity ($\rho_c < 0.2\mu\Omega cm^2$) sample measured for two temperatures (5 K and 300 K) at zero magnetic field, 3T and 5T. Remarkably, now the $E(J)$ characteristics, which overlap each other for a specific temperature, do always present a reproducible linear and non hysteretic behavior under all conditions. This behavior was found to be preserved in samples with dissipative contact power up to 0.5 Wcm^2 (Fig. 4.2 (c)). Moreover, the curves were also found to be independent of the current ramp rate employed, up to 0.1mA/s. We note that, in our experiments the J values reached were pretty high ($J \backsim 2 \times 10^5\ Acm^{-2}$), depending on the measuring temperature[32,80,121].

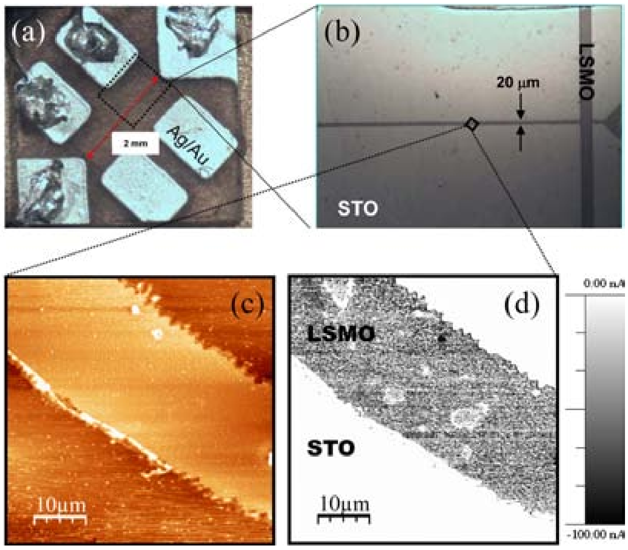

Fig. 4.3: *Top: (a) Optical micrograph of a lithographed sample and (b) magnification of the lithographed tracks. Bottom: SFM images of (c) topography and (d) local conductivity map at* $V_{tip} = -1V$ *measured at the lithographed LSMO bridge. The non-conducting character of the bare STO substrate contrasts with the conducting character observed in the LSMO thin film track. The maximum current response corresponds to saturation of the current amplifier, fixed to 100 nA in the experimental set up used.*

The fact of observing linear $E(J)$ curves without any hysteresis in the LSMO films measured with low DCP values allows us to safely conclude that Joule self-heating in LSMO thin films, up to the high J (and Q) values used in this work (Fig. 4.2) does not induce bistable resistivity. The reason for this can be found through an analysis of the own Joule self-heating and thermal transfer processes. In the adiabatic regime, assuming that Joule self-heating is fully invested in increasing the temperature of the LSMO film, this would be:

$$\Delta T = \frac{\int I \times V dt}{Vol \times C_P} \tag{4.1}$$

Where I is the current through the sample, V the voltage detected, Vol the volume of the sample and C_P the specific heat[38]. This regime results to be a very unrealistic situation because, if it was the case, a rise in temperature of $\Delta T \backsim 10^4$ K would be achieved, in complete disagreement with the observed linear $E(J)$ characteristics. The stationary isothermal limit for the thin film, on the other hand, assumes that the Joule self-heating Q would continuously flow through the substrate towards the thermal bath at which the substrate is thermally anchored. Under this regime no dependence of $E(J)$ on the current ramps should be found, as it is the case in our experiments.

Solving the Fourier equation of thermal transport, including Joule heating of the LSMO film and thermal conduction through the substrate to a thermal bath at fixed temperature T_B, the temperature difference between the LSMO film (T_f) and the base of the substrate (T_B) can be written as:

$$\Delta T = T_f - T_B \sim \frac{Qt_st}{k_s} = \frac{\rho(T)J^2t_st_f}{k_s} \tag{4.2}$$

where t_s and t_f are the substrate and film thickness, respectively, and k_s (0.15 $Wcm^{-1}K^{-1}$) is the thermal conductivity of the substrate[153]. The consequences of such thermal transport are shown in the upper panels of Figure 4.4. The result of estimating T along the $E(J)$ curves is depicted as a color scale.

We first assess the case of maximum $Q = \rho J^2 = EJ$ values ($J \backsim 5 \times 10^4\ Acm^{-2}$, $Q \backsim 2 \times 10^{12}$ Jm^{-3}) resulting from data at $T_B = 300$ K in Figure 4.2(c), and which are higher or similar than most of the commonly used values. The calculated T_f values differ from T_B at most by about $1.5K$. This temperature increase (represented by the color scale in Fig.4.4(a)) induces relative resistivity changes $\Delta\rho(T)/\rho(T) \backsim 2\%$, within the LSMO film and hence linear $E(J)$ curves are measured within this Joule self-heating regime. Now we compare with what happened when the transport measurements at 300K were carried out up to higher J values ($J \backsim 1 \times 10^5 Acm^{-2}$) LSMO thin film and a $DCP \backsim 10^{-7}Wcm^2$. Figure 4.4(b) displays a typical $E(J)$ curve where a volume dissipation $Q \backsim 1{\times}10^{13}Jm^{-3}$ could be reached. It is clearly seen that some non linearity and $E(J)$ hysteresis is induced under these conditions without any transition to a second stable resistance (resistance bistability). Within the scenario described above, i.e. a steady isothermal state for LSMO film with Joule heat flowing through the substrate, the film temperature would increase Eq.((4.2)) by $\Delta T \backsim 11 - 12K$ (see color scale in the figure). This temperature increase induces relative resistivity changes $\Delta\rho(T)/\rho(T) \backsim$

8%, within the LSMO film. The observed resistivity increase in Figure 4.4(b) is consistent with the experimental $\rho(T)$ curve in Figure 4.1, therefore validating the use of this thermal transfer model.

To visualize the stable solutions existing in a LSMO film measured at J and having a firm thermal anchoring, we rewrite Eq.(4.2) in the following way:

$$\rho(T_f) = \frac{k_s}{J^2 t_s t_f}(T_f - T_B) \tag{4.3}$$

For each J, the stable film temperatures (T_f), accordingly to thermal transfer model, can be found by looking for the intersection points of the experimental $\rho(T)$ and the straight lines starting at T_B and with slopes $K_s/J^2 t_s t_f$. In order to show that, the resistivity under zero magnetic field shown in Fig.4.1 is displayed now in Fig. 4.4(c) together with the straight lines corresponding to a series of representative J values used in the $E(J)$ experiments ($T_B = 300K$) for lithographed and non-lithographed samples (details are given in the figure caption). The inset shows a magnification of the 300K region where it is easy to verify the final temperature for the extreme J values. The crossing points with $\rho(T)$ determine the corresponding resistivity, $\rho(T_f)$, and film temperature (T_f) values, which are fully consistent with those determined in the $E(J)$ curves reported in the top and medium panels of the figure.

From the shape of the $\rho(T)$ curve and the corresponding $K_s/J^2 t_s t_f$ lines, it is clearly seen that the straight lines starting at T_B could have two intersection points with $\rho(T)$ when T_B is below $\backsim 250K$. Hence bistable resistivity of thermal origin in LSMO films having a firm thermal anchoring can only be achieved below this temperature. For instance, measurements performed at $T_B = 5K$ in lithographed films would require measuring with $J > 5.2 \times 10^5 Acm^{-2}$ to detect resistance bistability, i.e. intrinsic self-heating bistable resistivity would only occur in LSMO thin films at very high current densities. Our results point therefore to the fact that either contact heating or bad thermal anchoring of the films may have strongly influenced other authors published measurements showing resistance bistability at high temperatures in LSMO thin films.

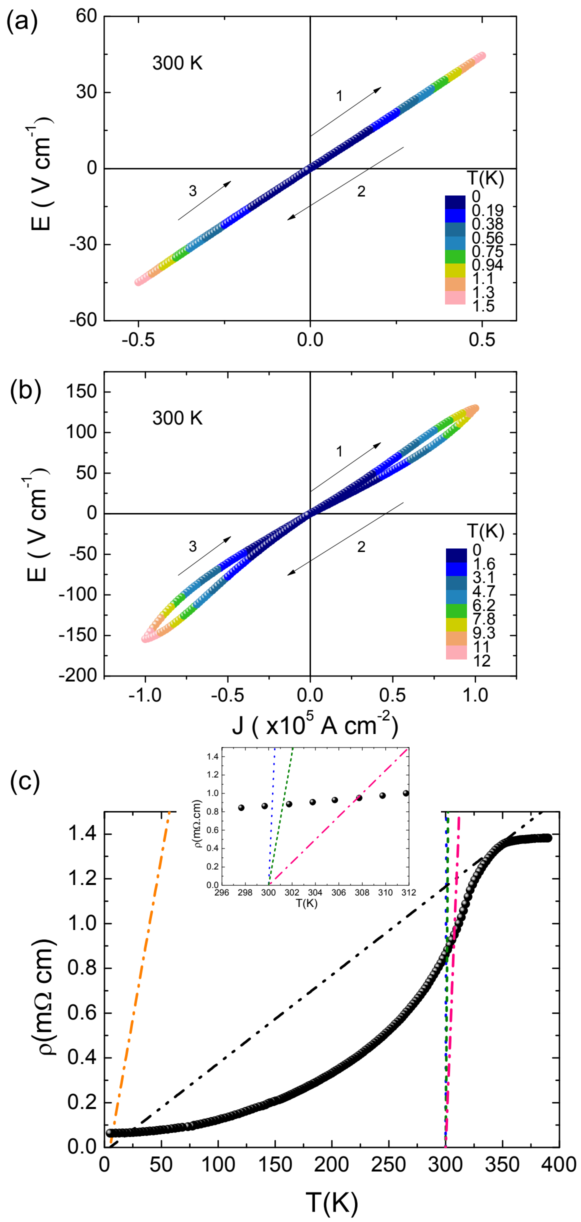

Fig. 4.4: *$E(J)$ curves measured at 300 K and zero magnetic field in non-lithographed LSMO thin films up to $J_{max} = 5 \times 10^4$ Acm^{-2} (a) and $J_{max} = 10^5$ Acm^{-2} (b). The calculated temperature increases based on a steady heat transfer through the substrate is indicated by a color code as indicated. (c) Main panel: Representation of the two members of Eq. (4.3), i.e., the resistivity under zero magnetic field data of Fig. 4.1(●) and $k_s/J^2 t_s t_f (T - T_B)$ for lithographed (blue) and non-lithographed (green and pink) films. For $T_B = 300$K, the three straight lines with decreasing slope, each for the experimental values $J = 2 \times 10^4$ Acm^{-2} (blue), $J = 5 \times 10^4$ Acm^{-2} (green), and $J = 1 \times 10^5$ Acm^{-2} (pink), respectively, were used to obtain the corresponding T_f. The inset is a magnification of the 300 K region to show the small rise in temperature. For comparison, two extreme cases are shown, in the main panel, for $T_B = 5$: the maximum J value employed in the presented experiments ($J = 2 \times 10^5$ Acm^{-2}, large slope line) and a typical J value ($J = 5 \times 10^5$ Acm^{-2}, low slope line) required to have bistability (see text).*

4.3 Determining the heating-free conditions at nanoscale

Aimed by the nowadays increasing interest of applying the bistability performances at miniaturization levels,[30,85,157,183] we have also addressed the influence of the electric contacts quality at the nanometer scale. In order to that, we have performed C-SFM measurements on the same LSMO films onto which Au nanoparticles were dispersed (see experimental methods at the end of this chapter). Figure4.5(a) shows the current map taken at $-0.5V$ where the Au nanodots are clearly visualized.

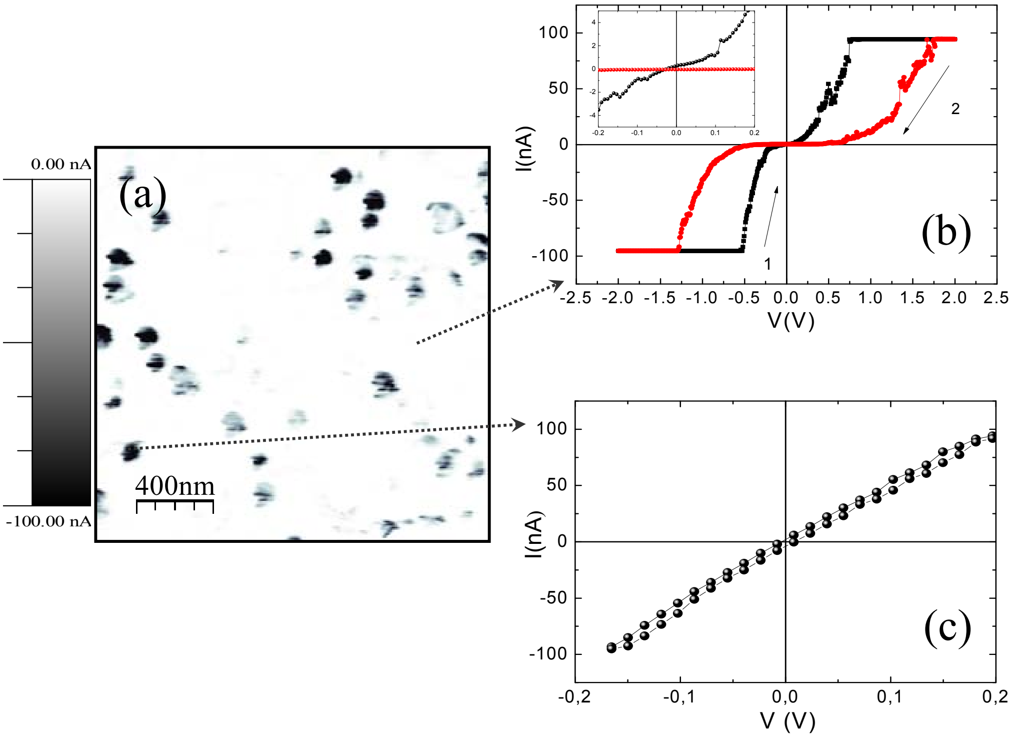

Fig. 4.5: *(a) Current SFM image ($2\mu m \times 2\mu m$) of a LSMO film surface where Au dots have been deposited (see experimental methods for details). The Au dots are easily identified at a small sensing bias ($V_{tip} = -0.5V$). (b) Typical I-V curve measured under direct contact between tip and LSMO surface. (c) Typical I-V curve measured through a contact of the tip on top of the Au nanodots. Flat regions response in the current are due to the saturation of the current amplifier, fixed to 100 nA in the experimental set up used.*

Current versus voltage (I-V) curves (Figure 4.5b) obtained by directly contacting the tip to the LSMO films, i.e. at the bare regions between nanodots, fairly well reproduced the non-linear I-V behavior generally observed so far in this type of measurements. Occasionally, these curves displayed some irreproducible hysteretic shape or instabilities, questioning the quality of the contact. To ensure a good electrical junction (nature and contact area) at the nanoscale dimensions during the I-V measurements, the conductive tip was then placed on top of different Au nanodots. Figure 4.5(c) displays a typical I-V curve in this case. The curves were found to be very reproducible and present a linear and reversible behavior, indicating ohmic contacts between the Au dots and the metallic LSMO films, as well as between the C-SFM tip and the Au nanodots. We remark that this linear behavior exists even beyond much larger I values than those measured for the direct contact. If we now analyse the involved magnitudes, we note that for similar J values, the estimated DCP ratio between tip-sample and tip-Au nanodot-sample contact is $DCP(tip - LSMO)/DCP(tip - Au - LSMO) \backsim 10^3 - 10^5$. To estimate DCP, the nanodot diameter was used to calculate the contact area in the tip-Au-film case, whereas for direct tip-film contact it was calculated using the Hertzian model.[*]

As in macroscopic measurements, linear and reversible I-V curves are recorded at nanometer junctions when using configurations with a low electrical contact resistance, while non-linear and hysteretic curves are obtained when poor electrical contacts (direct tip-film contact) are used. This is observed even at low voltages as seen in the inset in Figure 4.5 (b). If the quality of the contacts is poor, additionally, the reproducibility of the curves is deficient because of the variability of the electrical resistance on repeated contacts. This nanoscale experiment further confirms that undesired Joule heating induced by contact heating may control I-V measurements in LSMO films unless proper care of the experimental set-up is considered. Our finding supports the macroscopic measurements showing that an intrinsic Joule self-heating bistable behavior does not exist in the LSMO films at 300K.

4.4 Summary

In this work we have shown that macroscopic transport and nanoscale current versus voltage measurements in $La_{0.7}Sr_{0.3}MnO_3$ thin films remain linear and non hysteretic up to very severe self-heating regimes when low dissipative contact powers are achieved. We have particularly shown that, when $E(J)$ measurements are performed at 300 K and current densities up to $J \backsim 5 \times 10^4 \ Acm^{-2}$ (Joule self-heating $Q = J^2 = 2 \times 10^{12} \ Jm^{-3}$), only a moderate rise in temperature ($\Delta T < 1.5K$) is estimated in the scope of a stationary thermal transfer model for the thin film, the $E(J)$ curves re-

---

[*] Using the Herzian model, the contact area (A) is obtained, for an applied force (F) and a tip radius (R), from the equations: $A = \pi \left(\frac{9}{16} \cdot \frac{R^2F^2}{E^{*2}} \right)^{1/3}$, where $\frac{1}{E^*} = \frac{1-\nu_{tip}^2}{E_{tip}} + \frac{1-\nu_{LSMO}^2}{E_{LSMO}}$. A typical F=50 nN is considered. A tip radius of 25 nm was estimated from line profiles across the Au nanodots, whose diameters were 10-15 nm as evidenced by TEM and IR absorption. For our tip-LSMO system, the respective Young moduli (E) and Poisson ratios (ν) are: $E_{tip} = 1000GPa$ and $\nu_{tip} = 0.15$, and $E_{LSMO} = 500GPa$[152] and $\nu_{LSMO} = 0.38$ (obtained from XRD and TEM measurements, see p.22).

maining linear. A noticeable hysteresis in the $E(J)$ curve is detected instead when the current density is increased up to $J \backsim 10^5\ Acm^{-2}$ ($Q = 10^{13}\ Jm^{-3}$) which leads to $\Delta T \backsim 12$ K.

We have further demonstrated that, under adequate measuring conditions, a regime of bistable resistivity in LSMO thin films is not achieved at $T = 300$ K. We otherwise suggest that this phenomenon would only occur in LSMO films when measuring at temperatures below $T \backsim 250$ K. The best geometry to achieve this regime being a lithographed film where very high current densities can be reached without detrimental effects associated to the electrical contacts which would perturb the thermal profile of the film. Non-linearity and hysteretic behavior have been indeed observed both in macroscopic and in nanoscale measurements, when the dissipative contact power is high. Obviously, our conclusion does not question the existence of bistable resistivity in other oxides, including several manganite phases previously investigated, such as $Pr_{1-x}Ca_xMnO_3$ or $Nd_{1-x}Ca_xMnO_3$[21,128,135,141], or in devices based on LSMO where a certain role of the metallic interfaces has been identified though still not completely clarified. It neither invalidates any proposal concerning the microscopic origin of this phenomenon. Our experiments strongly suggest, however, that in order to firmly conclude about the origin of the intrinsic mechanisms operating in resistance switching, the influence of contact heating and Joule self-heating need to be properly weighted.

Our analysis stresses the very relevant role played by thermal heating generated at the electrical contacts in the investigation of high current transport measurements.

4.5 Experimental procedures

$La_{0.7}Sr_{0.3}MnO_3$ films with a thickness of $\backsim 24$ nm were grown by Chemical Solution Deposition (CSD) on (100)$SrTiO_3$ (STO) substrates ($5 \times 5\ mm^2$). The metal-organic solution was deposited by spin coating, at 6000 rpm for 2 minutes, and annealed at temperatures in the range $900°C - 1000°C$ under an oxygen gas flux, for different times, up to 12 h. Heteroepitaxial growth of LSMO films was confirmed by $\theta - 2\theta$ XRD patterns and XRD q-plot measurements showed that the films are fully strained (see Chapter2).

Electrical transport measurements were performed in a PPMS Quantum Design system in a four-point configuration and magnetic measurements were carried out with a SQUID magnetometer provided with a 7T magnet. To ensure well defined geometries while having large areas where any possible inhomogeneity would be averaged out, lithographed films were prepared through standard photolitography with track widths of 20 μm and 600 μm and voltage taps separated by 2 mm and 1.3

mm, respectively. To explore the influence of the contact resistance, different assemblies were used. Electrical contacts with high resistivity values ($\rho_c \backsim 8.5\Omega cm^2$) consisted of wires directly attached to the film with Ag paste, whereas low resistivity contacts ($\rho_c < 0.2\mu\Omega cm^2$) were obtained by using Ag wires welded with indium to 1 μm thick Ag contacts (capped with 30 nm of Au and annealed to $400°C$ during 1 hour) evaporated onto the LSMO film. To analyze the power dissipated at the structures, $E(J)$ measurements were carried out with different maximum currents, up to 120 mA ($J \backsim 10^5 Acm^{-2}$) for non-lithographed films and up to 5 mA and 0.1 mA for the 600 μm and 20 μm track width lithographed films, ($J = 3 \times 10^4 Acm^{-2}$ and $J = 2 \times 10^4 Acm^{-2}$, respectively).

C-SFM measurements were performed under low humidity conditions (2% RH in a N_2 flux) using a commercial head and software from Nanotec.[77] We used commercial conductive boron-doped diamond coated tips and cantilever force constants of $k = 2.8Nm^{-1}$ (Nanosensors). The conducting tip is biased and placed in contact with the sample, under controlled load, i.e. by using a normal force feedback, to measure the current flow. The same tip has been used in all the C-SFM experiments presented here to permit their direct comparison. In this case, dramatically different dissipative power conditions were obtained by performing I-V curves either in direct tip-film contact or placing the tip on top of Au nanodots[†] previously dispersed by spin coating onto the LSMO film. A thermal treatment at $300°C$ during 1 hour was used after Au deposition to minimize the contact resistance.

[†] A stable aqueous colloidal solution ($105mg/l$) of citrate-stabilized gold nanoparticles were obtained by using trisodium citrate for the reduction of chloroauric acid ($HAuCl_4$) and provided by Dr. J. Dauchot-Weymeers (Université Libre de Bruxelles).

Chapter 5

Reversible bipolar resistive switching in $La_{0.7}Sr_{0.3}MnO_3$ thin films

"Whereof one cannot speak, thereof one must be silent."
Ludwig Wittgenstein

5.1 Motivation

The actual knowledge's based society requires a new more powerful memory technology to develop any field concerning human activity as biomedicine or spatial areas, metereological predictions, simulation in basic research science or entertainment. Nowadays the computers use two types of memories, dynamic random access memory (DRAM) and static random access memory (SRAM). The handicap of this fast memories is that they are volatile, i.e. data is lost when the power supply is removed. For this reason computers also using a nonvolatile memory: hard disk drives (HDDs). HDDs are nonvolatile but they are slow, thus increasing the computer start up time. Another kind of nonvolatile memory are the Flash memories[94]. Their main drawback the slow writing speed and limited number of write/erase cycles. Therefore they are employed for data storage in hard disks, digital cameras, USB memory sticks or cellular disks. At this point, the need of new materials with higher performances have been encouraged the basic research in this field.

In particular, oxide based electronics has become an exciting and strongly developing field because many new functionalities can be reached through small structural or electronic modifications. Metal-insulator transitions, magnetism, ferroelectricity, superconductivity, multiferroicity and semiconductor behaviors have been shown to be feasibly modified at the nanoscale, thus opening new prospects towards a new generation of nanodevices.

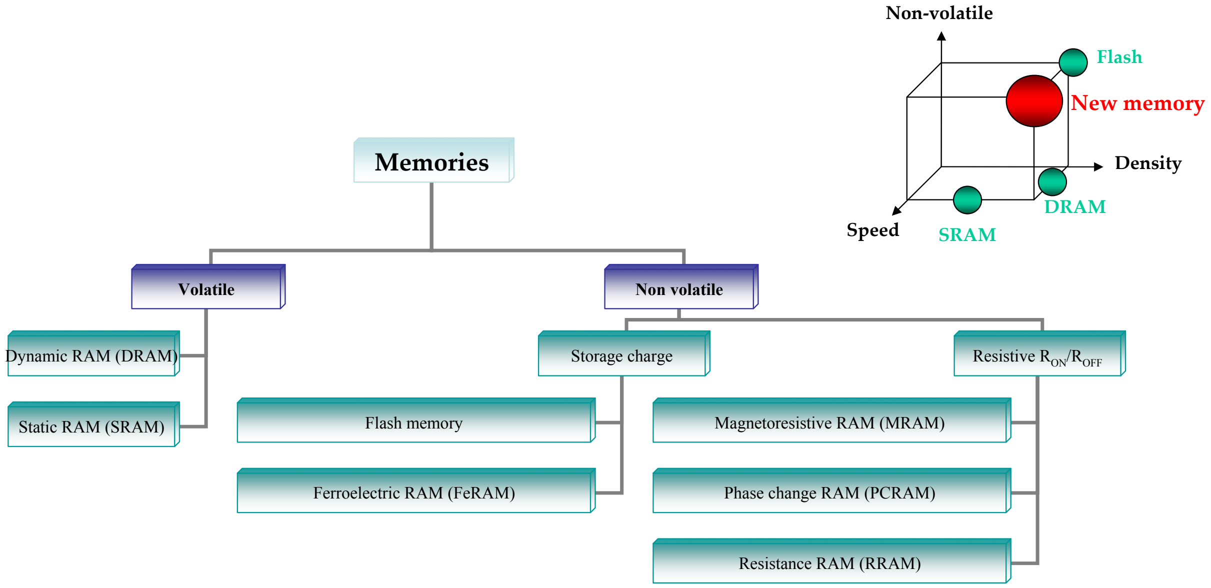

Fig. 5.1: *Emerging new memories*

Resistive switching memory devices (ReRAM) are based on one of the most promising non-volatile data storage concepts to replace conventional charge storage-based devices like EEPROM (Electrically Erasable Programmable Read Only Memory) or Flash[94]. In such devices, a switching mechanism between two distinct resistive states is electrically controlled, in current and/or voltage, depending upon the nature of the material integrated in the memory cell. This technology is already much faster than DRAM and uses less energy, presents good possibilities to reach SRAM speeds, is nonvolatile and would possibly replace hard-drives considerably reducing booting times.

Among the different materials (ferroelectrics[57,181], ferromagnetics[178], multiferroics[56], and chalcogenoides[69,120]) proposed as candidates to be used in a new solid-state nonvolatile ($>$ 10 years) memory technology[104], transition metal oxides are pursued with increasing interest to provide devices with high areal densities, fast random access ($t_{read} \backsim 10$ ns and $t_{write} \backsim 5 - 100$ns), virtually unlimited usage ($> 10^6$ cycles) and low power consumption[140]. Within this scenario, the possibility of fabricating multiple-bits-per-cell resistive memories would considerably increase the storage density capabilities of any conceivable device.

In addition to the operability conditions referred above the new memory technology must spend a low power consumption and all at a low cost.

In addition to that, the theoretic discovery of memristor (memory-resistor) in 1971 by L. Chua and after, experimentally in 2008 by HP Labs.[154], has open the new era in artificial intelligence. In fact, recently Di Ventra and his colleague Pershin have demonstrated experimentally a associative memory with memristive neural networks[123].

5.2 Resistive switching: state of art

Basic ReRAM research is by far not new. It begun almost 40 years ago with works on oxide insulators[76] and amorphous materials[120].

Several types of oxides, such as CuO[29], NiO[25], TiO_2[34,182], Al_2O_3[24], $Pr_{0.7}Ca_{0.3}MnO_3$[7,97] and $La_{1-x}Sr_xMnO_3$[26,96] have been found to display electrically switchable resistivity properties in two terminal geometry junctions. Multiple microscopic mechanisms have been proposed based either on redox processes involving cation or anion migration[8], on the formation/rupture of conducting nanoscale filaments[36,97,134], oxygen diffusion[115], Mott metal-insulator transition[82,135],variable Schottky barrier[165], or charge trapping at interfacial sites[119]. In fact, the actual slow down in RRAM research involving transition metal oxides presenting this phenomenon, comes from the fact that many of the different mechanisms proposed so far, very likely do compete depending on the material. Weighting each contribution is not evident and in most cases only hints on the possible causes have been given.

Very often, however, only macroscopic analyses were reported strongly limiting the capability for a detailed microscopic understanding. A thorough nanoscale analysis of the relationship among structure, composition and physical properties is required to establish clear grounds for understanding and controlling the physical properties at the nanoscale and hence make possible a new generation of nanodevices.

5.3 Resistive switching procedure

The robustness of the switching process with no dependence on particular morphological thin film details will be demonstrated by presenting results for different LSMO samples prepared by the same CSD method and consisting of ultrathin films with different thicknesses (8, 10 and 24nm) and surface morphologies. We first illustrate a complete writing, reading and erasing process performed on a 24 nm thick LSMO film (sample 1) exhibiting a certain concentration of outcropped La-Sr oxide (LSO) nanodots as described in chapter 2. These LSO nanodots are the controlled result of a La excess in the chemical solution and, as it has been already demonstrated in a throughout characterization they do not influence the composition nor the physical properties of the surrounding metallic LSMO film. The surface morphology of this sample is shown in the SFM image of figure 5.2(a)-(b), where the LSO nanodots (50-80 nm high) appear as bright spots outcropping from the thin film surface level. As expected, they exhibit an insulating character, which can be clearly seen in the C-SFM taken at a tip voltage $= 2$ (Fig. 5.2(c)). These nanodots will result therefore very useful to identify surface locations as well as being an excellent in-situ reference for conductivity response measurements. Because no changes in the electrical properties of the film were never observed at this voltage value after repeated sweeping, it will be used as the reading voltage ($= 2$) throughout the following experiments.

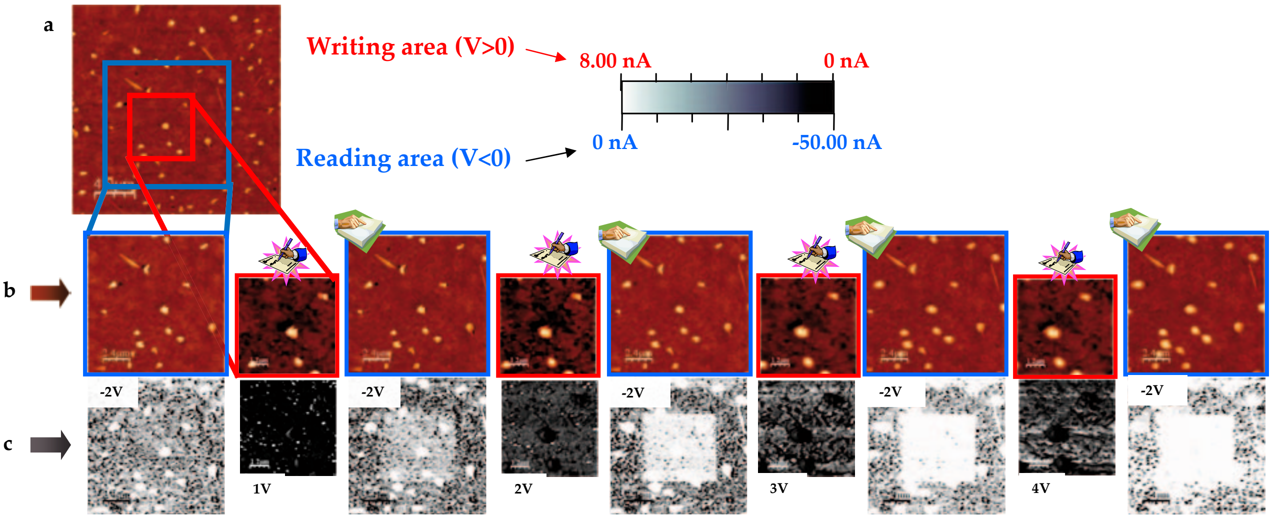

Fig. 5.2: *Resistance switching movie: writing and reading the local conducting properties of LSMO. The reversible transition between low resistive (LR) and high resistive (HR) states is performed (writing at appropriates) by conducting scanning force microscopy (C-SFM). (a), topographic image (20 γ 20 γ) of a 24nm thick LSMO thin film (sample 1). A certain concentration of outcropped insulating ($\chi\phi$ τ) π (LSO) nanodots (50 80 nm high) are used as in situ reference for topographic and conductivity measurements. Concentric squares on the image correspond to the writing (inner square) and reading (outer square) regions, respectively. (b)-(c), topographic and current maps images series displaying the reading area (12 γ 12 γ) taken at $= 2$, before (virgin state) and after writing a HR area (6 γ 6 γ) at several steps $= +1$ $+2$ $+3$ $+4$.*

Electrical switching between LR (ON) and HR (OFF) was accomplished by a systematic approach. The concentric squares in Fig. 5.2(a) correspond to the writing/erasing (inner square) and reading (outer square) regions, respectively. Control of the conducting stage of the surface after scanning at a given > 0 was always monitored by zooming out and reading at $= 2$. The experiments were based on the following protocol:

1. The scan range is set to the reading area. The tip is biased at and topography and current images are simultaneously acquired to characterize the conducting state of the surface
2. The scan range is reduced to the writing area. The is set to a given positive value and topography and current images are simultaneously acquired
3. The is brought back to the reading value ( ) and any possible modification is checked by repeating (1). The process in (2) is repeated at increased until no current is detected within the writing region. The corresponding voltage, which will be seen to slightly depend on film thickness, is considered as the onset for writing, .
4. If desired, total or partial switch back to the conductive stage can be accomplished by scanning the modified region (or a portion of it) at a negative at which the conducting character is recovered. This is called the erasing voltage, .

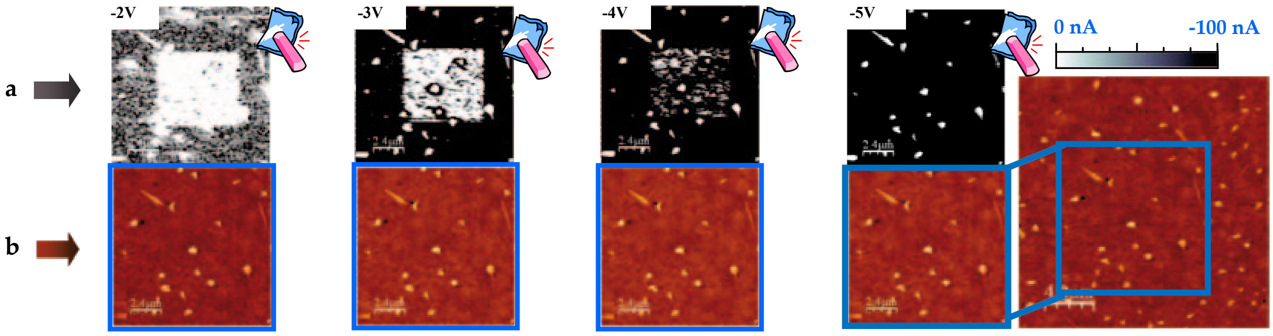

Fig. 5.3: *Resistance switching movie: erasing the local conducting properties of LSMO. The reversible transition between high resistive (HR) and low resistive (LR) states is performed by conducting scanning force microscopy (C-SFM). The non-conducting character of the written region (white square) is reversed by changing the voltage polarity: (a), reading process at* $= 2$ *and three steps of the erasing process* $_{0} = 3$ *,* 4 *and* 5 *. The conducting character of the initial LSMO is recovered. (b) topographic images series of the erased region.*

Figure series 5.2(c) correspond to a writing (at $= +1\ +2\ +3\ +4$) and reading ($= 2$) steps showing that after using a writing voltage of $= +4$ the scanned region has been completely transformed and presents a non-conducting character. Note that at this point, the LSO non-conducting nanodots are no longer distinguished from the surrounding surface. Figures 5.3(a)-(b), on the other hand, illustrate three steps of the erasing process ($-3V$, $-4V$ and $-5V$). As it is seen the electrical transition is completely reversed for $V_{er} = -5V$.

Note that because $V_{er} > V_{rd}$, more current is detected in (f) than in (b). Interestingly, a close inspection of the whole reversing process allows observing that the near surroundings of the outcropped LSO nanoislands (Fig. 5.2(d)) do reverse the conducting character at slightly lower voltages that the rest of the LSMO film. This can be attributed either to the effect of the local strain induced in the LSMO film at the boundaries with the LSO nanodots (previously demonstrated by TEM analysis in chapter 2), to point defects or slightly different film thickness at these locations or to a local redistribution of atomic species. This issue will be readdressed later on throughout the chapter.

Figure 5.4a shows a typical I-V characteristic curve conducted by application of a voltage cycle ($-10V$, $+10V$) starting from negative values at a fixed tip location on the virgin (pre-switched) film surface. Positive bias is defined as the voltage by which electrons current flows from the sample to the tip. The duration of the cycle is $\tau = 76$ ms and the voltage sweep sense is indicated by the arrows. The result is a clearly asymmetric bipolar switching curve which indicates that probably diverse microscopic processes govern charge injection under each bias polarity. In bipolar switching systems the set operation takes place on one polarity of the voltage or current, and the reset operation requires the opposite polarity[176].

After the conducting (LR) excursion for negative V_{tip}, the I-V slope decreases ($-0.5V < V_{tip} < +0.5V$) reflecting a large tip-film surface contact resistance and again increases for positive voltages till suddenly drops at $V_{tip} = +5V$. This critical V_{tip} is close to the V_{wr} determined from the previous experiment (figure 5.2c) and is considered the set point for switching (LR to HR). In this particular case, the drop in the measured current gives a conductance ratio of $I_{ON}/I_{OFF} \backsim 10^2$ but could be up to 10^3 depending of the final HR stated reached. As can be better observed in the clearly hysteretic logarithmic plot of figure 5.4 (b), from this set voltage on, a negative resistance region is observed and a high resistivity state is reached, in which the current stays at very low values (< 10 nA) all the rest of the cycle until, eventually, the voltage ramp reaches the established maximum ($V_{max} = +10V$). As corresponding to a new stable steady state, the system persists at this HR during the voltage excursion back until a given opposite polarity bias, $V_{tip} \backsim -8V$ in this case, is reached. At this voltage, in what resembles a rectifier behavior, a sharp current injection drives the system to the initial conducting state, where it remains during the rest of the excursion, completing the cycle. As it will be demonstrated through different experiments described in this thesis work, independently of

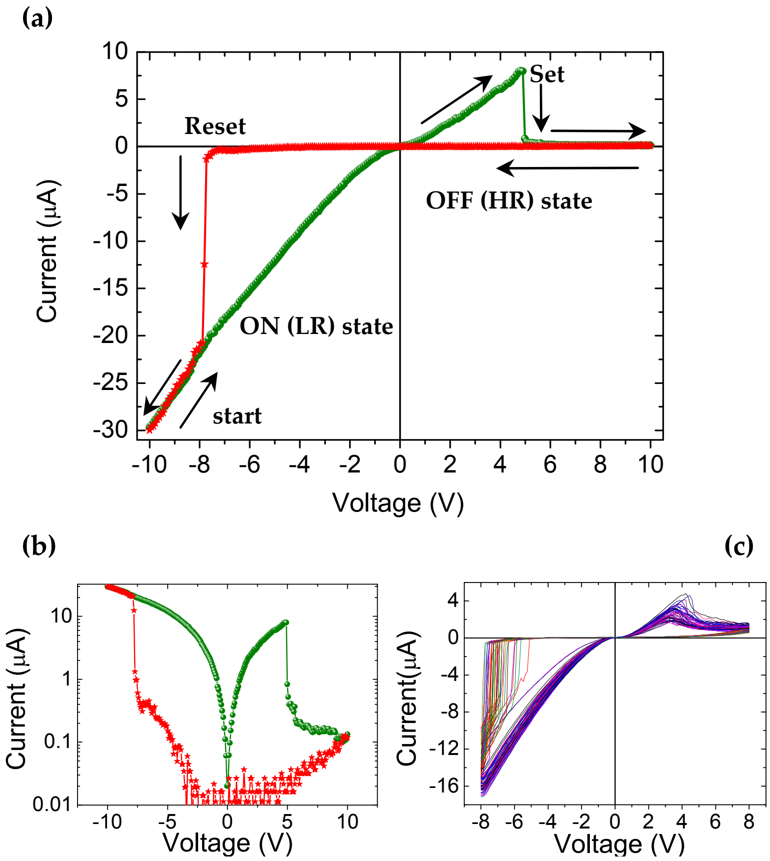

Fig. 5.4: *Local current-voltage characteristics and endurance test. Hysteretic bipolar switching I-V curves for a 10nm thick LSMO thin film (sample 2). (a), starting from a conducting (LR) state, the voltage ramp is applied to the tip from negative to positive values and back to complete the cycles as indicated by the arrows. SET (LR to HR) and RESET (HR to the initial LR) points are marked in what is the first I-V cycle. LR and HR are identified as ON and OFF, indicating the pass or blockage of electronic current through the device. (b), Logarithmic scale plot of the I-V in (a), showing the abrupt change in conductivity ($I_{ON}/I_{OFF} > 100$) at the operation SET. (c), endurance test (100 of a 500 I-V cycles series). Though a reduction of the reset voltage is eventually observed, the system maintains its switching behavior.*

the initial negative V_{tip} value, but depending on the final V_{wr} different final HR state can be reached, revealing a tuneable resistance multilevel switching in this LSMO system. From the shape of the I-V curves, the possible nature of the set and reset states will be further discussed below.

We remark that due to the metallic nature of the film, no electroforming[36] (in the common sense of this term as the formation of paths for conduction) is needed to observe resistance switching, guarantying no oxide breakdown, which would depend on the dielectric and structural quality of the film. Moreover, the polarity of the set switching (LR to HR) and reset switching (HR to LR) voltages was in each case always the same, independently of the voltage cycle direction. The persistence and robustness of the process was verified by consecutive bipolar switching curves conducted on the same surface location. Figure 5.4c shows the first 100 of 500 bipolar cycles of one example of such endurance tests. Though a reduction of the reset voltage is eventually observed, the system maintains its switching behavior. Importantly, no differences in the reported switching ON behavior were detected by changing the compliance current in the range from 1 pA to 1 mA, then it was usually set to values adequate to properly measure the complete I-V cycles.

As commented above, the writing process can be conducted at different V_{wr} to tune different HR states. The corresponding V_{er} , would consequently depend on the specific V_{wr} used (Fig.5.5) and results to be of about the same absolute value, $V_{er} \backsim -V_{wr}$. Reaching a negative voltage large enough is needed to be able to inject current into the system.

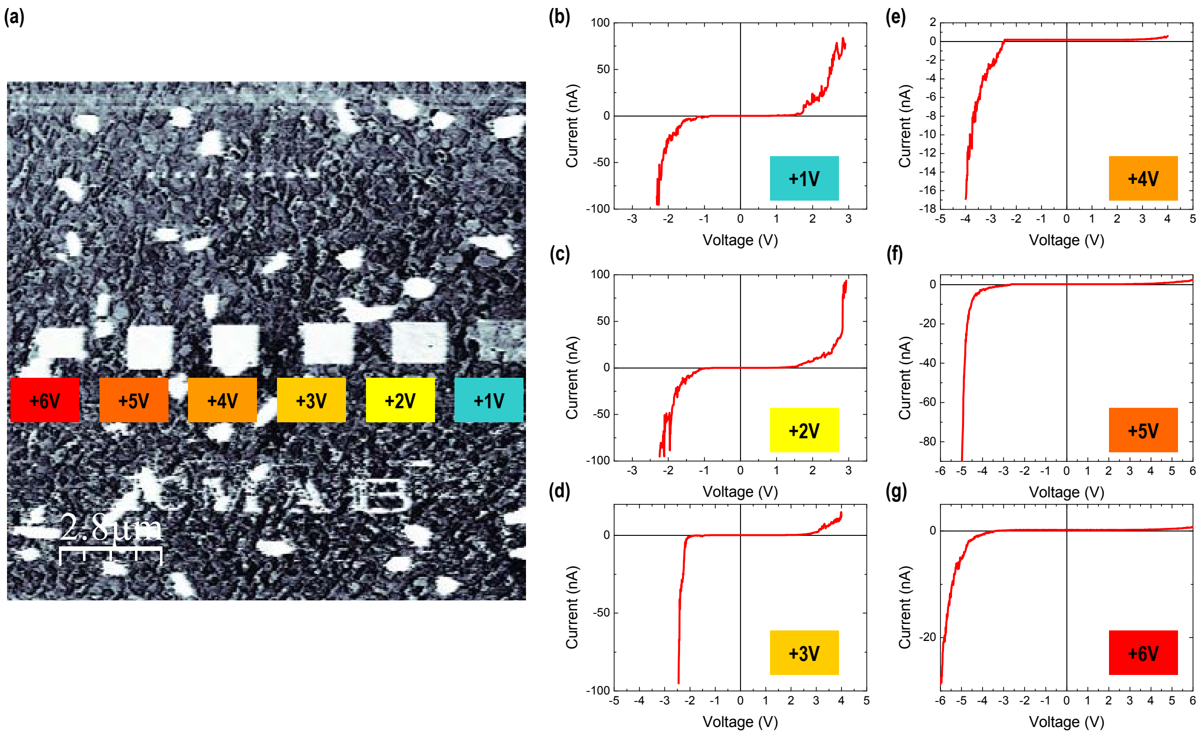

Fig. 5.5: *(a) Current map reading image of different HR states written at V_{wr} from $+1V$ to $+6V$. The corresponding I-V curves (b-g) are restricted to the V range of interest and to illustrate that the rectifying (reset) behavior occurs at $V_{tip} = -V_{wr}$, indicating the multilevel nature of the resistive LR to HR switching. The I-V curves have been performed from positive to negative voltage values. The institutional logo "ICMAB" has been lithographed at the bottom image using the lithography tool of the Nanotec*[114] *software.*

A complementary method to analyze the memory effect between writing and erased processes is the so called 3D modes (sec. 7.8.4). This method is used here to measure the current as a function of the applied voltage (V) along a surface line (xy), thus obtaining a I(xy,V) image as that of figure 5.6c which crosses the regions modified by writing at different voltages, as indicated in figure 5.6a. In such a way: horizontal profiles in the image of figure 5.6c provide the current relief values along the xy line at a given voltage (Fig. 5.6d) and vertical profiles correspond to the characteristic I-V curve at a given point (x,y) (Fig. 5.6e). In such a way, in one unique 3D image, the whole set of I-V curves are obtained for an ensemble of surface locations (line). In this particular case, starting with a $= 4$ it can be seen that the HR states written at $+1$V, $+2$V and $+3$V have been erased while HR states written at $+4$V, $+5$V and $+6$V remain unaltered. This supports that in order to erase a given HR state, the applied voltage should be at least .

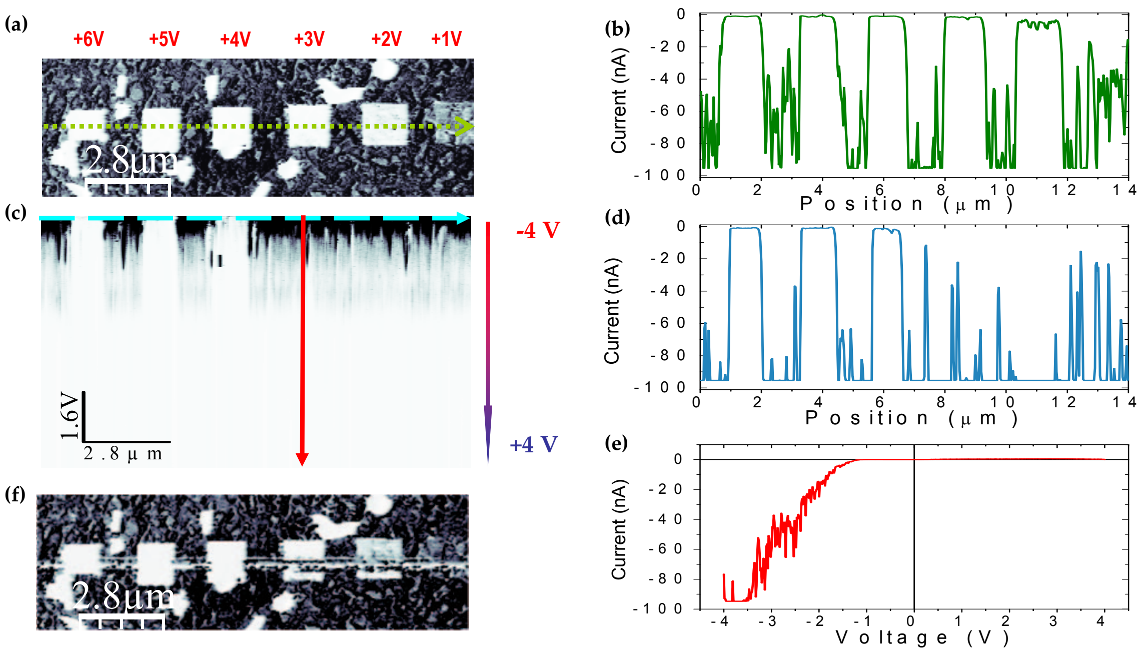

Fig. 5.6: *(a) Current map reading at* 2 *image of different HR states written at* *from* $+1$ *to* $+6$ *. (b) Current profile along the doted green line crossing the HR modifications. (c) 3D I(xy,V) image where the horizontal axis denote the x-y position, the vertical axis goes from top (-4V) to bottom (+4V) and the colour scale (from black to white) designs the detected measured (from* $100\rho\nu$ *to* $0\rho\nu$ *). (d) Horizontal profile at -4V (blue line) and vertical profile (e), i.e, I-V curve (red line)taken along the corresponding lines indicated in the I(xy,V) in (c). (f) Current map reading image after 3D image. Note that because the initial voltage is -4V, large enough to erase modifications written at lower writing voltages, a line has been erased (the system goes back to a conducting state) along the +3V and +2V squares. Similarly, since the final V reached is +4V, at which the virgin film is transformed to a HR state, a line has been written along the tip pass location between the initial modified squares.*

Because the final V reached during the 3D imaging reaches the value of $+4$, which is high enough to modify the virgin film surface, a line has been erased between the marks. In addition, as the initial voltage is 4 , a voltage large enough to erase modifications written at lower writing voltages, a line has been erased along the $+3$ and $+2$ squares. As a consequence, we can think of wire-like modifications, promising for nanodevice applications, made by the sweeping action of the tip at different voltages. The longitudinal dimension of such wires is only limited by the total piezo scan range (up to sixty microns) and the short dimension is limited by the contact area of the tip. At the present, lines as thin as 100 nm can be performed. If the voltage is applied on an specific point, insulating nanodots of comparable diameter are obtained instead (Fig.5.7). This demonstrates the scalability of the resistive switching effect to nanoscale devices.

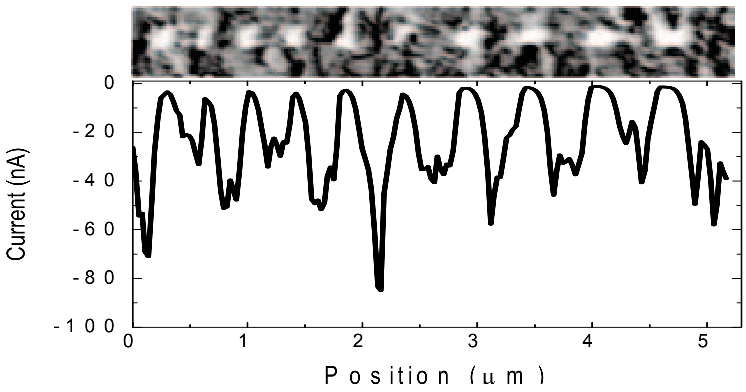

Fig. 5.7: *Current map of some HR modifications to illustrate the storage capability of the method in* 24 *nm LSMO film thickness : high resistance nanostructures are embedded in a metallic matrix. The lateral size of each nanostructure is under 100 nm.*

In addition, because the importance of knowing about the spatial extent in depth of the induced transition, i.e. whether the whole film thickness is modified or not, we employ a lithographic SPM based strategy to write HR states with specific geometries.

Figure 5.8 presents a series of induced HR states made with the conducting tip, by using lithography mode of Nanotec software, describing rings (dotted lines in (a)) at different , on a 10nm thick LSMO thin film with quite homogeneous morphology (sample 2). As can be seen in the current map of figure 5.8(b), while at below +5V no noticeable changes were detected, from this voltage on non-conducting rings were observed. Interestingly, for $> +10$ negligible or no current was measured within the inner ring region. The lack of detectable current in that region, where no electrical change must have been induced, points to a blockage of the electric current at the ring location and across the whole film thickness, which prevents electric flow between tip and the grounded electrode, placed at the sample border (millimeters apart from the tip-surface contact). This interpretation is confirmed by locally erasing the HR state at the location marked by the solid line in figure 5.8c which indicates the tip trajectory at $V_{er} = -10V$. The erased narrow bridge restores the electrical connection between the region enclosed by the ring and the rest of the metallic LSMO film (Fig.5.8d). Such a simple experiment leads us to conclude that, effectively, the film was driven to the HR state throughout the whole film thicknesses following the vertical component of the high electric field created at the tip apex i.e. forming a non conducting tube that completely blocks the current through the inner region (5.8e), which becomes a topologically isolated volume. Though the true electric field distribution in this system is not known, because of the relationship between the tip-sample contact area ($\backsim 100nm$ in diameter) and the film thickness ($< 24nm$), the electric field drop will be maximum under the tip.

An schematics to illustrate that the whole thickness of the LSMO film can be modified is shown in (Fig.5.8e). When the HR ring does not reach the underneath insulating substrate, electric contact between the inside region exist and current is measured within. However, once the full film is modified, the electrical contact with the inner region is cut and, consequently, it is seen as an insulator in the current map. This gives to a “wrong” reading, since a conducting region would be seen as non-conducting in the C-SFM maps and points to the need of finding a different reading tool.

Thus, even though the above experiment completely demonstrates the local nature of the electrical switching process, it means that a proper reading procedure different than C-SFM is needed. In order to do that we performed combined C-SFM and KPM measurements in the very same region. We note that combining these two SFM modes requires controlling the operation parameters to be able to pass from direct tip-surface contact, at which C-SFM writing and reading are made, to non-contact dynamic KPM sets at which the tip is located tens of nm apart from the same surface.

An array of rings written at different voltages were lithographed in an 8 nm thick LSMO film (sample 3), where small LSMO islands appear as nanometric ($\backsim 2nm$ high) bright protrusions in the topographic image of figure 5.9a. The LSMO nature of these islands is revealed by their conducting character (darker spots) as seen in the current map in (b). A low onset for switching ($V_{wr} = +2V$) seems to correlate with the lower film thickness of this sample. Exactly the same behavior already described for sample 2 is observed in the C-SFM measurements, where no current is detected in the non-modified inner ring regions. Conversely, a notable piece of information is provided by the contact potential difference (CPD) image, revealing KPM as a more sensitive tool than C-SFM to changes in the LSMO nature. A customized colour scale has been used to highlight the discrete

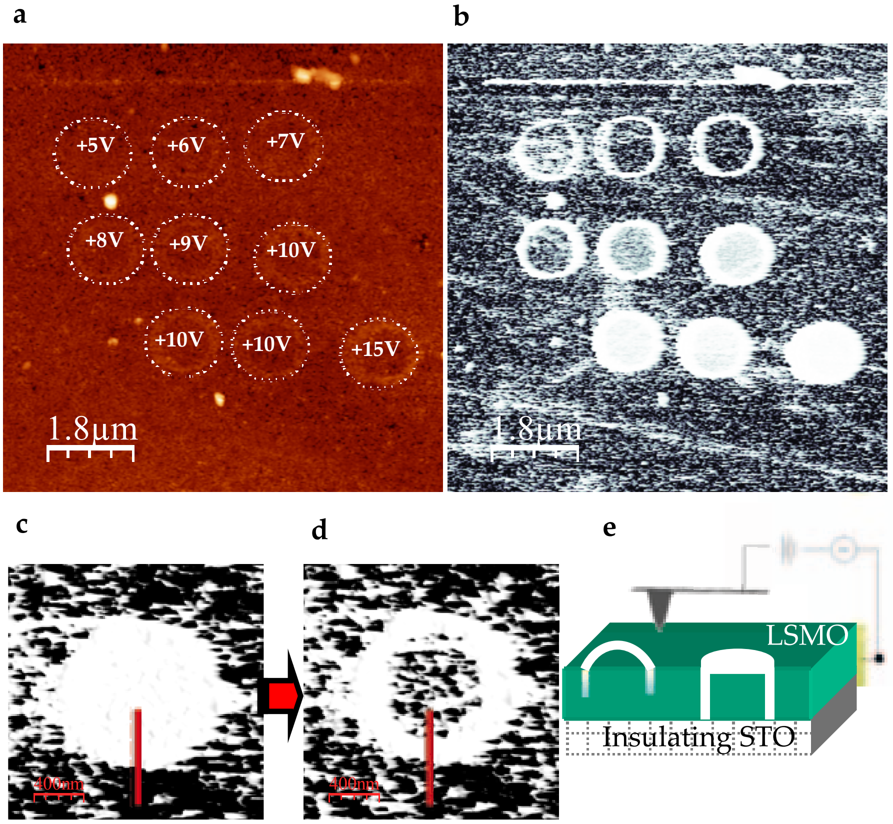

Fig. 5.8: *Full LSMO film thickness modification: voltage dependence of the writing process. (a-b) Simultaneously acquired topographic view and current map (* $= 2$ *) of a 10nm thick LSMO thin film (sample 2). A lithographic C-SFM procedure has been used to write HR states with ring geometry at different* *from* $+5$ *to* $+15$ *. From a given voltage threshold, non-modified (LR) regions are electrically isolated, indicating the whole film thickness has been driven to the HR state. (c-d) verification test: current images before and after a LR bridge connects the inner conducting region with the outer conducting LSMO film. The bridge LR state is induced by drawing a line crossing the HR ring (red line) with the tip at reversed polarity,* $_{\theta} = 10$ *). (e) Schematics of the proposed lithographed model (cross section) and C-SFM set up (not to scale). The tip is biased and the counter-tip electrode contact is established at the border of the sample. The schematics illustrates how the inner (non-modified, i.e. conducting) region encircled by a HR ring can be seen as conducting or not depending on the depth of the HR modification.*

values of the surface potential that are depicted as a function of in the plot.

The film surface can be visualized as the top view of a series of HR hollow cylinders embedded in a thin LR matrix. If we consider a conducting SFM tip and a conducting sample, with different work functions (see experimental procedures, sec.7.8.4), which are electrically connected, then the electrons trying to move out of the different surface regions would see a different potential barrier

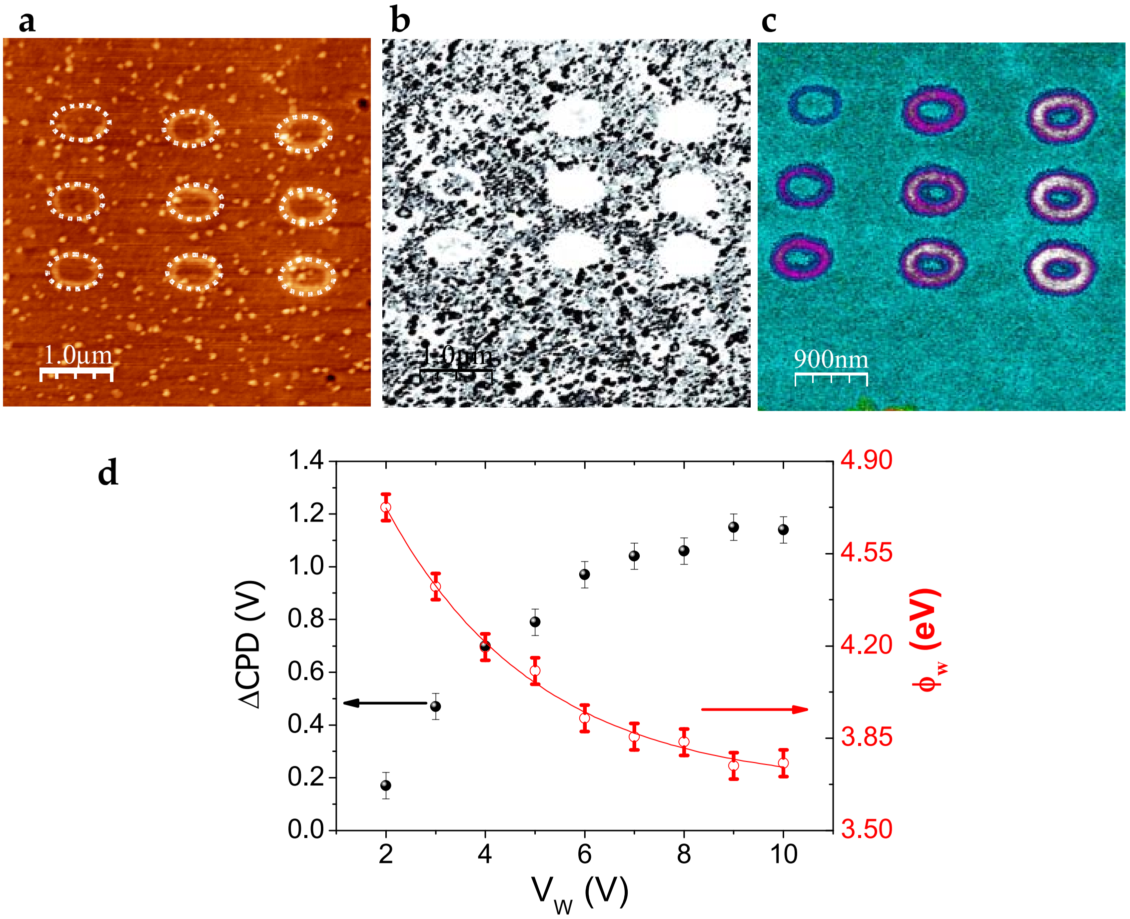

Fig. 5.9: *Combined C-SFM and KPM reading strategy and HR multilevel detection. C-SFM measurements are performed by placing the tip in direct contact with the sample whereas KPM are done in a non-contact dynamic mode (*$\backsim 10-30$ *nm apart). (a) Topographic view of a* $8nm$ *thick LSMO film (sample 3). The dotted lines indicate the written HR rings at different increasing voltages* $V_{wr} = +2V$ *to* $+10V$*, in steps of* $1V$ *from up to bottom and left to right. (b) Simultaneous reading current map (*$V_{rd} = -2V$*). Total current scale is* $100nA$*. (c) Contact potential difference (CPD) map as measured by KPM. The CPD color scale goes from cyan (*$0V$*) to white (*$1.2V$*). (d) contact potential difference (left axis) relative to that of the LSMO virgin film (*ΔCPD*) as a function of* V_{wr} *and calculated local work function (*$\phi_w = \phi_{LSMO} - \Delta CPD$*) (right axis) for the different HR written states.* $\phi_{LSMO} = 4.9$ *eV is taken from reference*[132]*. Importantly, KPM is sensitive to different HR states (correct reading and multilevel detection) not distinguishable in the C-SFM measurements.*

(electrostatic) which leads to a different work function (ϕ) depending on the local electronic properties[117]. When this barrier is larger (higher ϕ) a decrease in the surface CPD signal is observed. If the work function of the vibrating electrode is ϕ_{tip} and ϕ_{LSMO} is that of the virgin LSMO thin film, then the contact potential for the virgin surface is:

$$CPD_{LSMO} = \phi_{tip} - \phi_{LSMO}$$

Whereas for a region written with V_{wr} would be given by:

$$CPD_w = \phi_{tip} - \phi_w$$

And consequently, the contact potential difference (CPD) between modified regions and the surrounding film will correspond to the change in work function respect to the non-modified conducting LSMO:

$$\Delta CPD = CPD_w - CPD_{LSMO} = \phi_{LSMO} - \phi_w = \Delta\phi$$

In other words, provided we know the CPD values measured for rings made at different voltages, the corresponding relative changes in work function ($\Delta\phi$) can be obtained as a function of the writing bias voltage. $\Delta CPD > 0$ indicates that the work function and, consequently, the hole concentration decrease in the modified regions ($CPD_w < CPD_{LSMO}$).

In addition the absolute value of $\Delta\phi$ increases for increasing V_{wr} and reaches a saturation value of $\Delta\phi \backsim 1.15$ eV. Provided the reported value for $La_{1-x}Sr_xMnO_3$ ($x = 0.3$) is $\phi_{LSMO} \backsim 4.895$ eV[132] our results indicate that the highest HR state reached corresponds to $\phi_w \backsim 3.7$ eV. The simplest way to interpret the work function changes obtained from the macroscopic image of CPD, could be interpreting these changes as being due to a decrease of the carrier concentration (holes) under applied positive bias. However, changes in carrier concentration due to changes in local composition, i.e cation or anion distribution, cannot be neglected. Using heteroepitaxial junctions, the Fermi level positions for $La_{1-x}Sr_xMnO_3$ referenced to the Fermi level of $Nb : STO$ ($SrTi_{0.99}Nb_{0.01}O_3$) have been reported to shift downward (increasing ϕ_{LSMO}) with hole doping as $\backsim x$(eV)[142] . Within this context, our results would be consistent with a situation of reduced x, lower than the initial x=0.3. Though the true composition after film modification is something to be evaluated (see below), we note that the LSMO phase diagram predicts an insulating character of $La_{1-x}Sr_xMnO_3$ for $x < 0.2$. Obviously, a similar behavior is expected for an increase in the amount of oxygen vacancies.

Back to the reversibility of the process, already observed in the C-SFM experiments described before, we now show the capability of KPM to read out and differentiate resistive states after several set and reset processes. Figure 5.10a shows the KPM image of a sequence of writing and erasing processes performed one after the other over decreasing areas on a 10 nm thick LSMO film (sample

2) i.e. scanning at alternating opposite bias voltages ($V_{er} = -V_{wr}$). In such a way, the central region has been modified four times (twice written and twice erased). The averaged CPD signal, i.e. the change in work function, reflects the back and forth change in electrical nature of the modified film regions. Interestingly, if the negative voltage employed during the reset process is larger than that for writing, work functions ϕ_w larger than that of the virgin state can be reached as well and thus the corresponding $\Delta CPD < 0$. This is illustrated in figure 5.10b for a 8 nm thick LSMO film (sample 2) where the inside of a square written at $V_{wr} = +4$ V was reset using a $V_e = -6$ V. The averaged CPD profile serves to illustrate that the capability of the method goes beyond reversibility and serves to finely tune the work function by choosing the appropriate V_{wr} and V_{er} .

The switchable character of these nanoscale modifications is further illustrated in Fig. 5.10c where a grid made of lines, lithographed by C-SFM at different writing and erasing tip voltages, is shown. First, six horizontal lines were lithographed at different V_{wr}, from +2V to +12V (bottom to top) on the same surface (sample 2). The vertical line profile crossing all the written lines is shown in the bottom plot of Fig. 5.10c to obtain the CPD of each state for increasing V_{wr}. As already commented, the work function value saturates at $\backsim 1eV$ for voltages larger than $+10V$. A series of lines perpendicularly lithographed at different negative voltages complete the squared grid. In such a way, at every vertical and horizontal cross of lines, a given HR state would be reset to a lower resistive state. Though the spatial resolution is limited and the erased states are slightly blurred due to overlap of high CPD values at adjacent HR states, the horizontal profile taken along the upper line ($V_{wr} = +12$ V) is shown in the top plot of Fig. 5.10c to clearly illustrate the result. Hills and valleys in CPD correspond to HR and LR states, respectively and exemplify the capabilities of bit storage in a foreseen multilevel device. This capability would be even larger if the multilevel resistance is employed in a nanodot array following a single point lithography (Fig.5.7) instead of a line based lithography.

Durability of the modifications were tested in time, temperature and magnetic fields, and the HR states were found to persist after several months, upon annealing up to 400 K and show no important degradation under magnetic fields up to 3T (see the before and after C-SFM measurements in Fig.5.11).

Throughout the different above considerations, we have suggested that changes in the local distribution of the existing atomic species can play a role in the reversible resistive switching of LSMO. In order to examine this point as far as possible and get more insight into the microscopic phenomenon here reported, the chemical composition of specific written (HR) and erased (LR) states were analyzed by means of soft x-ray photoelectron emission microscopy (PEEM)[13]. Precise sur-

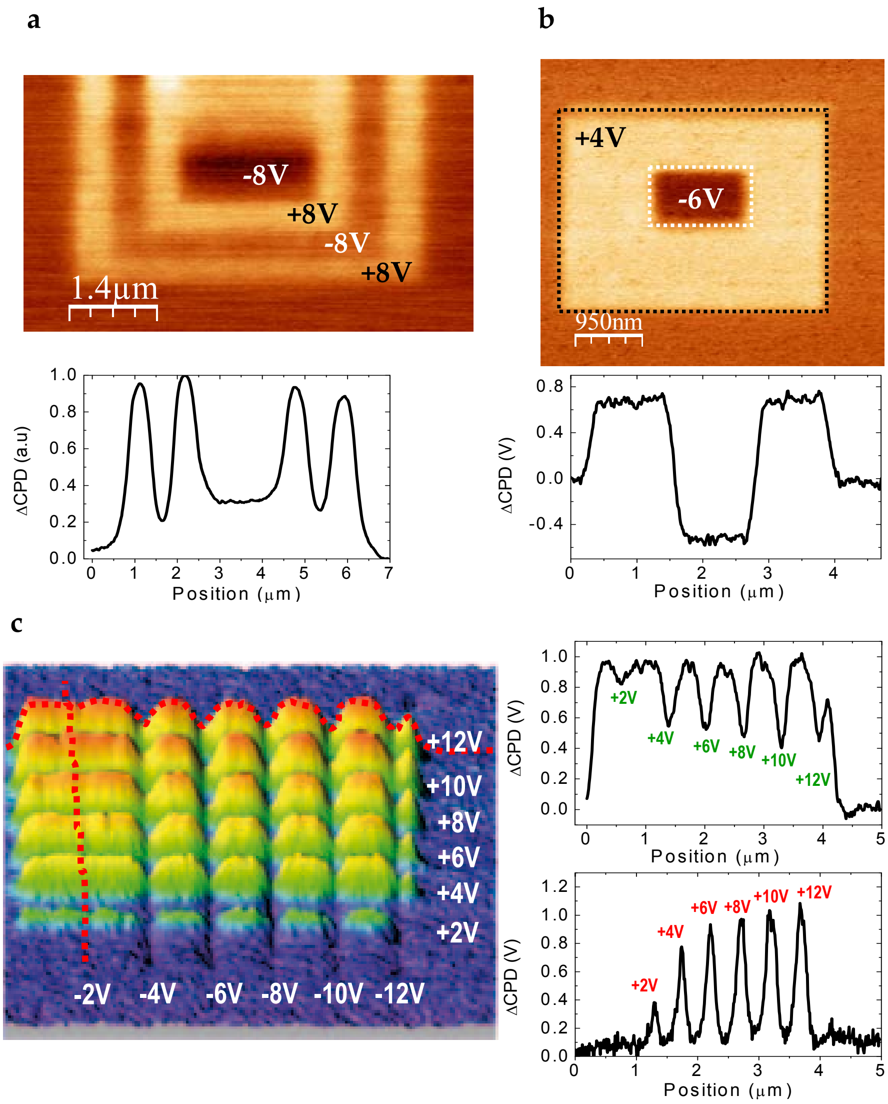

Fig. 5.10: *Reversible multilevel LR and HR data storage. (a) KPM image and corresponding line profile, of a sequence of writing and erasing processes performed one after the other over decreasing areas on a 10nm thick LSMO film (sample 2) at opposite bias voltages (* $= +8$ *and* $_{\theta} =$ 8 *). (b) KPM image of a writing (* $= +4$ *) and an erasing (* $_{\theta} = 6$ *) processes performed one after the other over decreasing areas on a 8nm thick LSMO film (sample 3). The corresponding line profile shows the sensitivity of KPM to detect positive and negative changes in the local , depending on the magnitude of the applied and* $_{\theta}$*. (c) Three dimensional view of a KPM image of a grid made of perpendicular crossing lines lithographed by C-SFM at different and* $_{\theta}$ *on sample 3 (left image). It is indicated the profile along the crest at the top line of the image (* $= +12$ *) (upper right plot), and along of the writing processes (lower right plot).*

face modifications could be studied by PEEM because their persistence time. Moreover, though they

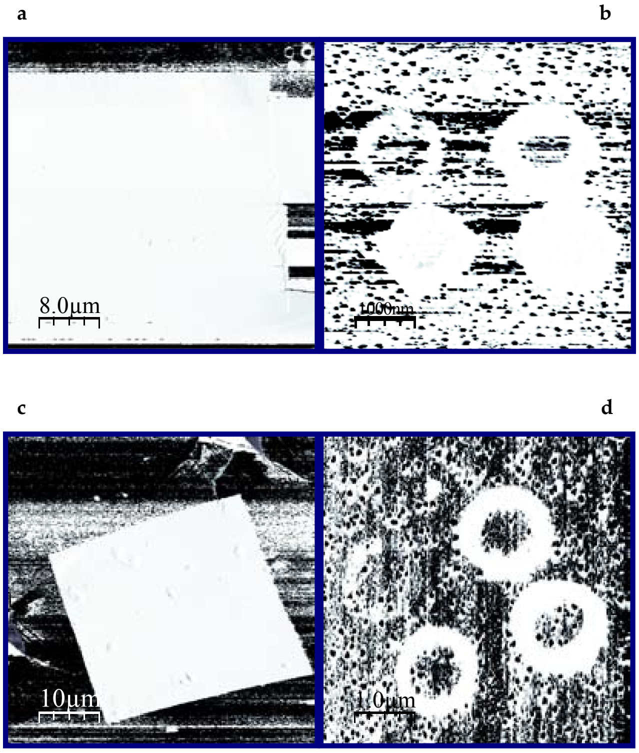

Fig. 5.11: *Current map reading images of different HR modifications before (a,b) and after several months (c,d) the samples were submitted to temperature (up to 400ºC) and magnetic field (up to 3T) endurance tests.Tough the small differences between b and d in the measured current can be ascribed either to different reading conditions or to a contamination layer which connects the inner and outer metallic regions, note that as well as the squared modification, the HR rings persist in all cases.*

were observable by SEM and PEEM in the image mode, for an easier location, the LSMO film surfaces were patterned with micrometric indentations forming specific geometries (see secc.7.7, p.103). Taking into account the high surface sensitivity of PEEM ($\backsim 4$ nm in depth), one of the thinnest LSMO films (sample 3) was used for these purposes. A summary of the chemical analysis is presented in figure 5.12 where a writing/erasing protocol similar to that of figure 5.10b was used: the inside of a square written at $V_w = +4$ V was reset using a $V_e = -6$ V. The modified region was imaged at several photon energies ($0.1-0.2$ eV steps) across the La $M_{5,4-}$, Mn $L_{3,2-}$, and O K-edges. Unfortunately, the experimental available energy range did not permit access to obtain information about Strontium. As can be seen in the images taken at each of the three absorption edges (left panels) clear differences between the virgin LSMO and the modified surface are observed. The central panels of figure 5.12 present the averaged Mn, La and O spectra as a function of photon energy for the regions of interest, namely LSMO (black continuous line), HR (red open symbols) and LR (green filled symbols).

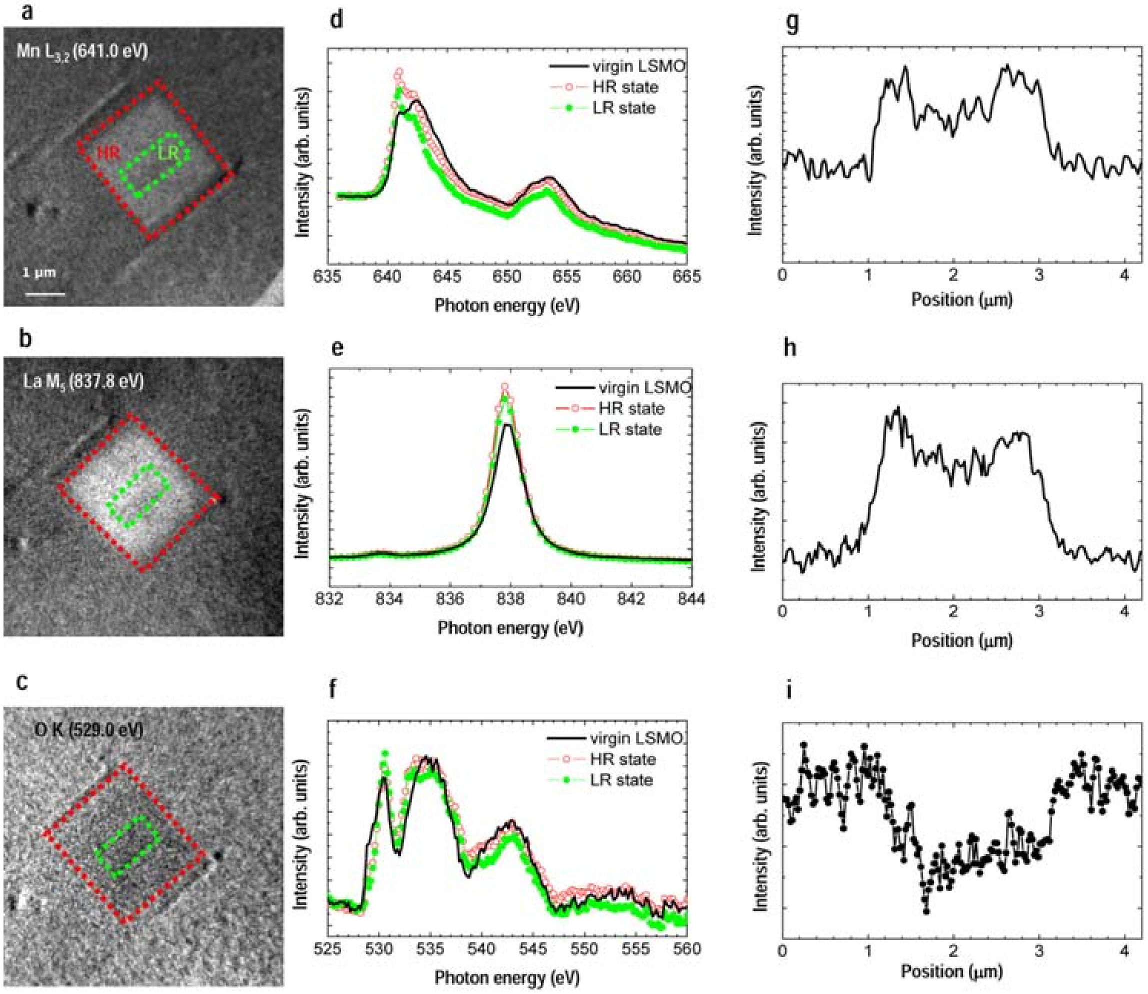

Fig. 5.12: *Atomic species distribution in switched HR and LR states. a, b and c, PEEM images obtained on a modified LSMO surface (sample 3) at selected energies* (641.0, 837.8 *and* 529.0 *eV) within the Mn L-, La M- and O K-edges, respectively. The inside of a square written at* $V_w = +4V$ *was reset using a* $V_{er} = -6V$. *d, e and f averaged spectra obtained within the virgin LSMO (black line), written HR state (red open dots) and erased LR state (green closed dots) regions at the Mn L-, La-M and O K-edges, respectively. g, h and i line profiles across the three regions (virgin, HR and LR) at the energies corresponding to images a, b and c, respectively.*

The virgin LSMO region depicts a Mn L-edge spectrum similar to that reported for mixed valence perovskites of the same composition with bulk-like magnetic properties[168,169]. The shape as well as the integrated intensity of this spectrum strongly depend on the Mn oxidation state[2,93] and the peak emerging at the low energy side of the L_3 edge for both, HR and LR regions, can be interpreted as the presence of divalent Mn[168,169]. On the other hand the broader intensity at few eV above the edge (and more pronounced in the virgin LSMO) is ascribed to $Mn^{3+/4+}$.

A detailed analysis of the whole spectrum, including double step background subtraction[27] indicates that the signals in the modified regions can be decomposed, in both HR and LR, as being due to 38% Mn^{2+} and 62% of nominal mixed $Mn^{3+/4+}$ valence[93], i.e. the proportion does not change during the set to reset transition. On the other hand, considering that the integrated intensity is proportional to the Mn-3d unoccupied states and keeping the relative proportions of Mn^{2+} and $Mn^{3+/4+}$, the total amount of Mn atoms at the HR region can be estimated to increase by about 22% with respect to that of the surrounding virgin LSMO film, within the same analysed depth. Upon erasing, the Mn content recovers approximately a 10%, i.e. the erased LR state has an excess of about 12% the value of the virgin film. The increase/decrease of Mn content indicates a clear displacement of Mn cations.

A similar result is observed for La cations. La M_5-edge spectra taken at LSMO, HR and LR are identical with respect to shape and energy positions indicating identical oxidation state for the Lanthanum cations (La^{3+}) in the three regions. Nevertheless differences on their relative maximum intensity highlight local changes of the cation concentration. The integrated intensity corresponding to the written region has increased by 27% with respect to that of the virgin LSMO film. Provided the oxidation state remains the same, this increase in intensity can be correlated to an identical increase of Lanthanum atoms at the HR region within the analysed depth. The La excess in the LR state is subsequently reduced by 9%, i.e. still a 18% larger than the initial value indicating that, as observed for the Mn species, the reset process seems not to be completely reversible in terms of La content.

Analysis of the O K-edge spectrum changes is not as straight forward. Three main features at ca. 544 eV, 536 eV, and at 530 eV, respectively are observed in case of $La_{1-x}Sr_xMnO_3$ perovskites. The broad peak at 544 eV is attributed to electronic bands of Mn 4sp and La 6sp character, while the one at 536 eV is related to a mixture of La 5d with Sr 4d bands, i.e. the spectrum reflects hybridization with the various elements and strongly depends on the oxygen local environment (Mn, La and Sr distribution and content). If only the intensity at 529 eV (bottom right panel in figure 5.12) is considered, contrary to what happens with Mn and La, a decrease of the signal is observed at the modified regions within the analyzed depth, otherwise in accordance with the reported correlation between Mn^{2+} formation and oxygen vacancies Vo^{2+} creation[2,44,93]. However, though the HR state induced during the writing process involves changes of the spectral shape and relative intensities of the different features, these changes seem to remain after the erasing process. Consequently, with the data at hand, it is not possible to correlate the changes in the O k-edge spectrum with the induced electrical modifications in the LSMO thin film.

The above results clearly point to the fact that both, electrons and ions may play an important role on the induced transition between LR and HR states. Interestingly, after Leon Chua predictions[35] on the existence of memristor devices[154], the hysteretic behaviour of many systems exhibiting resistance switching have been described by mechanism involving both electronic and ionic transport. This might be also the scenario for the present case. The switching characteristic observed for a particular memristive system helps classifying the nature of the dopant drift inside the memristor. In this context, the shape of our hysteretic I-V curves would be consistent with a hard switching governed by nonlinear ion drift in high electric field[182]. These nonlinearities have been related with long retention times and fast switching process[155].

5.4 Summary

In this chapter, we have described a low energy consumption procedure which permits the reversible electrical resistivity switching in $La_{0.7}Sr_{0.3}MnO_3$ thin films in an extremely local and controlled way. Though not completely understood, the mechanism by which the LSMO is transformed from its intrinsic metallic to one non-conducting character is described within the frame of electronic and ionic transport within the oxide film. First of all, starting from a metallic oxide, obviously no electroforming is needed. In addition, it is based on LSMO intrinsic properties and not on particular film surface or interface details. The measured conductance ratios ($I_{ON}/I_{OFF} > 100$) are valuable for high efficiency amplifiers. An excellent write and erase endurance makes both ON- and OFF-states stable over more than 500 cycles, under continuous readout testing. The modifications persist after annealing (tested in the range 5 - 400 K), show no detectable degradation under magnetic fields (tested up to 3T) and display a long retention time (several months). Our approach is based in a new concept where the writing and erasing processes are made through C-SFM while read out is performed through a non-invasive KPM. The dynamic range for the writing process spans a range of $\Delta\phi \backsim 2$ eV and KPM is able to work as a multilevel recording device we think that an important increase of the integration density (at least by a factor 20) might be achieved. The capability to fabricate multilevel and switchable resistive nanostructures embedded in low cost oxide thin films can be easily envisaged as a suitable approach towards active electronic elements, in particular for the fabrication of high-density data storage applications.

5.5 Experimental procedures

Scanning Force Microscopy (SFM) measurements were performed using a commercial head and software from Nanotec[114] under a N_2 environment (RH 2%) to diminish any possible humidity effect. For the conductivity measurements (C-SFM), we used either commercial conductive B-doped diamond-coated tips with $k = 2.8N.m^{-1}$ (Nanosensors) or Cr-Pt coated Si tips with $k = 3N.m^{-1}$, resonance frequency of 75 kHz and contact resistance of 300 ohms on Pt thin film surface (Budgetsensors in factory specifications). The same tip has been used in all the C-SFM experiments of at least one series. To check tip-sample conditions, the adhesion force was systematically determined from force versus distance curves prior to and after each conductivity experiment. Current images were acquired in a non-invasive manner (no sample indentation) by using the contact operation mode at the lowest possible applied load required. The conducting tip (first electrode) was placed in direct contact with the sample, under controlled load, i.e. by using a normal force feedback and the current was measured between tip and sample. Simultaneous topographic images z(x,y) and current maps I(x,y) over a given region at a fixed voltage permitted writing (positives V_{tip}), reading (small positive V_{tip}) and erasing (negatives $_{Vtip}$). In our setup, the sample was always grounded and the voltage was applied to the tip. Provided the insulating character of the substrates used ($SrTiO_3$) the direct electric contact to ground is established through a metallic clamp (counter electrode) firmly attached to the surface film at the sample border (millimeters apart from the tip-surface contact). An external I-V converter (*Stanford Research Systems*) was used to have access to a wide range of compliance currents ($1pA$ to $1mA$). Whereas for topographic images the color code is the commonly used, bright for high and dark for low, for the current maps it depends on the voltage sign. Thus higher currents appear darker in C-SFM images taken at negatives V_{tip}, while brighter for positives V_{tip}. The current-voltage (I-V) characteristics of the contact where measured as a function of the bias voltage applied between tip and sample, starting from negative tip voltages.

Kelvin probe force microscopy was used to measure the surface contact potential difference (CPD) simultaneously to topography. The tip-sample distance was controlled by a feedback loop working in the dynamic mode. The mechanical vibration of the cantilever is done at the first resonance frequency, which in our case is about $75kHz$. To detect the electrostatic force, an ac voltage $V_{ac}sin(\omega t)$ is applied between tip and sample, in addition to a dc bias V_{DC}. The ac voltage induces oscillatory electrostatic forces according to $F_{el} = -\partial C/\partial z(V_{DC} - V_{CPD})^2$, where the spectral component at the frequency of the ac voltage results to $F_{\omega} = \partial C/\partial z(V_{DC} - V_{CPD})V_{ac}sin(\omega t)$. The oscillation at ω is detected using a lock-in amplifier and a controller is used to reduce the amplitude to zero by adjusting V_{DC} to match the CPD. In order to avoid crosstalking with topography, the oscillating bias voltage is applied at a lower frequency of $7kHz$ with an ac bias voltage of $0.5V$.

Photoelectron emission microscopy (PEEM) experiments were perfomed at the UE49-PGM-a beamline of the BESSY synchrotron facility by using an Elmitec PEEM provided with energy filtering. This allows single photoelectron peak imaging and therefore to obtain space resolve chemical information. The angle of incidence of the incoming X-ray linearly polarized beam with respect to the sample surface was fixed to 15.7^{o}. Within such a configuration the effective X-ray spot sizes $35\mu m \times 10\mu m$.

Chapter 6

General conclusions

This concluding chapter summarizes, the questions addressed and results of the present thesis. The thesis was dedicated to the study of structural, electronic and magnetic properties of doped lanthanum manganite $La_{0.7}Sr_{0.3}MnO_3$ thin films on strontium titanate $SrTiO_3$ grown by chemical solution deposition method.

Below follow the main results obtained from our studies.

A new mechanism is proposed for the generation of self-assembled nanodots at the surface of a film based on spontaneous outcropping of the secondary phase of a nanocomposite epitaxial film. Epitaxial self-assembled Sr-La oxide insulating nanodots are formed through this mechanism at the surface of an epitaxial metallic ferromagnetic $La_{0.7}Sr_{0.3}MnO_3$ film grown on $SrTiO_3$ from chemical solutions. TEM analysis reveals that, underneath the La-Sr oxide (LSO) nanodots, the film switches from the compressive out-of-plane stress component to a tensile one. It is shown that the size and concentration of the nanodots can be tuned by means of growth kinetics and through modification of the La excess in the precursor chemical solution. The driving force for the nanodot formation can be attributed to a cooperative effect involving the minimization of the elastic strain energy and a thermodynamic instability of the LSMO phase against the formation of a Ruddelsden-Popper phase $Sr_3Mn_4O_7$ embedded in the film, and LSO surface nanodots. The mechanism can be described as a generalization of the classical Stranski-Krastanov growth mode involving phase separation. LSO islands induce an isotropic strain to the LSMO film underneath the island which decreases the magnetoelastic contribution to the magnetic anisotropy.

We have studied epitaxial single crystal LSMO thin films on STO substrate grown by CSD method as a function of the LSMO film thickness to evidence the connections between structure, microstructure and physical behavior. X-ray diffraction has shown that for CSD-grown LSMO films the completely relaxed state is achieved at very low thickness ($60nm$). Self-nanostructured LSMO films consisting of $(La, Sr)O_x$ islands and Ruddelsden-Popper inclusions within an epitaxial matrix of high crystalline perfection, are shown to plastically relax the films at these thickness. Curie and metal to insulator transition temperatures show film thickness dependence, but they do not show correlation with strain states. The analysis of the dependence of the Curie temperature on the elastic deformation can only describe the response of the fully strained films ($24nm$), whereas for partially and fully relaxed films ($35nm$ and $60nm$) other effects should be considered. On the other hand, the T_{MI} dependence with thickness could be explained by using lattice parameters arguments alone, while the MR^{5T} and ρ^{390K} evidenced an influence of structural and chemical disorder in the film for the thickest and relaxed films. The lack of a full correlation between the strain state, T_c and T_{MI} suggests that these transition temperatures are influenced in a different way by other factors, such as chemical inhomogeneity and structural disorder in the film.

The E(J) characteristics of well characterized fully strained epitaxial $La_{0.7}Sr_{0.3}MnO_3$ films have been investigated up to high current densities ($J \backsim 10^4 - 10^5\ Acm^{-2}$). Different electric contact resistances and different current path configurations have been used to sort out the role of Joule self-heating from contact heating in the transport properties. It is demonstrated through macroscopic transport and conductive scanning force microscopy measurements that contact heating may lead to non-linear and irreversible E(J) characteristics when high contact resistances are used. Low dissipative contact power measurements are crucial to define the upper J limits to keep linear and reversible E(J) characteristics. We demonstrate that Joule self-heating in $La_{0.7}Sr_{0.3}MnO_3$ thin films only induces moderate warming at high temperatures while achieving bistable resistivity at low temperatures would require the use of very high current densities ($J \backsim 5 \times 10^5\ Acm^{-2}$).

Switching from different resistive states is an outstanding phenomenon observed in several complex oxides with potential for large-capacity non-volatile memories. Most microscopic mechanisms proposed so far involve particular interfacial properties and imply high energy consumption for operation onset. Instead of the widely investigated high to low resistance transitions, we report on the nanoscale reversible transition from low resistive to tunable high resistive states, where no electroforming processes are needed. The conducting tip of a scanning force microscope has been used to reversibly write non-conducting states through the whole thickness of well characterized thin films of the robust metallic ferromagnet $La_{0.7}Sr_{0.3}MnO_3$ obtained by chemical solution deposition. The Kelvin probe microscopy is proposed as a non-invasive reading tool for quantitative multilevel detection and Soft X-ray photoelectron emission microscopy highlights the importance of cationic and anionic diffusion in the process. This nanoscale investigation of the local resistivity switching in the absence of junction interfaces, points to inherent thin film properties as responsible for the observed phenomenon.

Chapter 7

Experimental techniques and procedures

7.1 Chemical solution deposition method

There are several methods to obtain oxide thin films. Manganite thin films have been prepared by a variety of physical and chemical methods (Fig.7.1). Physical methods that have been used include: magnetron sputtering, molecular beam epitaxy (MBE), pulsed laser deposition, etc. A comparative overview addressing the common features and the differences of the physical deposition methods is given in a recent review paper[66]. However, in these methods, not only a special expensive apparatus is required, but also formation of a thin film having a large area are difficult.

The term Chemical Solution Deposition (CSD) include a broad spectrum of techniques ranging from sol-gel processing over hybrid approaches to metal organic decomposition (MOD)[144]. It is a long-established industrial process very cost-effective and versatile and it presents a closely control of the composition . By careful control of the precursor chemistry and processing parameters the control of surface morphology, electronic and magnetic properties is possible.

The sol-gel process in general is based on the transition of a system from a liquid solution "sol" (mostly a colloidal suspension of particles) into a gelatinous network "gel" phase. Sol-gel, hybrid deposition methods, and MOD are based on the use of metalorganic precursors. In contrast to sol-gel approaches, that use generally alkoxide precursors, MOD methods typically use carboxylate precursors. MOD methods are more straightforward than sol-gel approach, since the precursors are commonly water insensitive. However, due to the high organic content of the films, cracking problems are frequently encountered. In order to get ahead of this drawback, there have been developed mixed routes which utilize precursors with smaller organic groups, which allow reduce the tendency toward cracking. These hybrid solution deposition methods generally use low molecular weight car-

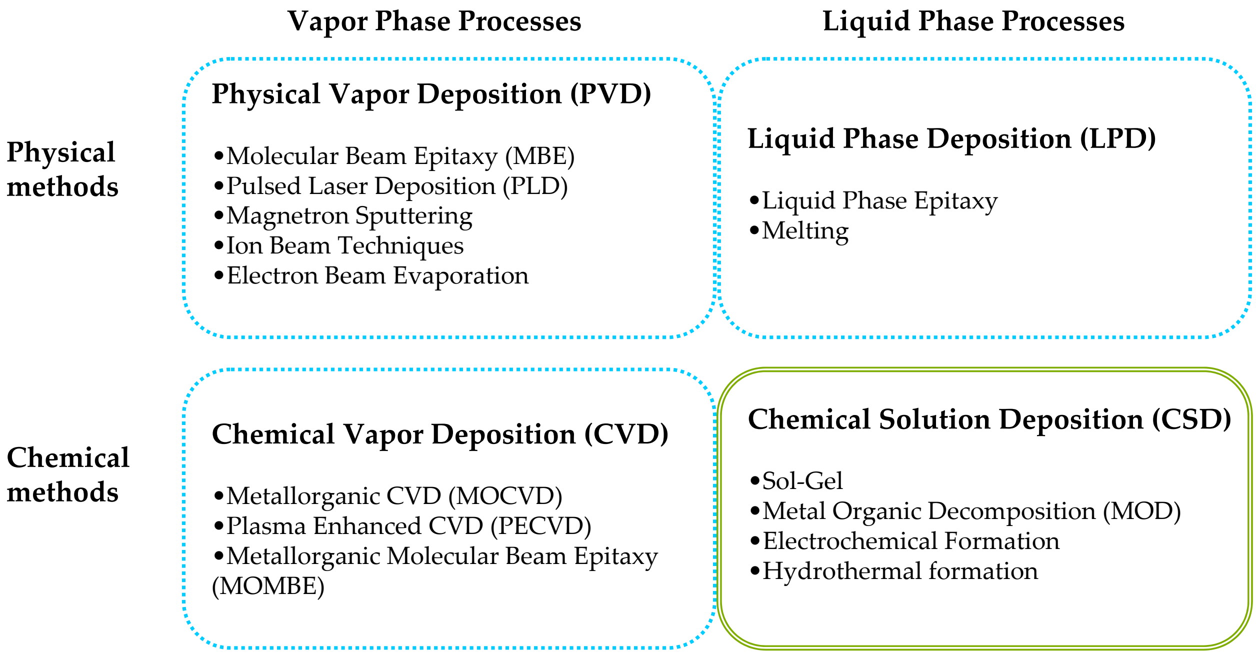

Fig. 7.1: *Overview on different deposition methods for electroceramic thin films.*

boxylate and alkoxide precursors, namely acetates or propionates.

Precursor solutions are deposited by different deposition techniques like spin coating, spray content or dip coating. All the samples studied in this report have been obtained by spin coating since it is a easy to apply, has low investment costs and the consumption of precursor solution is lower. The chemical structure of the precursor solution and its thermal decomposition behavior have a large influence on the microsstructure of the resulting thin film and hence its physical properties as we seen in previous chapters.

7.2 Synthesis of samples

All the samples have been grown by MOD route. The precursor solution have been prepared according to the flow chart displayed in figure 7.2. This is a well established route developed by *Hasenkox et al.*[72,73].

In the first step commercially La-, Sr- and Mn-acetates[*] are dissolved in a large excess of propionic acid and distilling of the liberated acetic acid obtaining dried propionates [†]. The propionates are all mixed and dissolved in propionic acid at room temperature to prepare the precursor solution.

---

[*] $(La(OOCCH_3)_3 \times 3H_2O$, $Mn(OOCCH_3)_2 \times H_2O$ and $Sr(OOCCH_3)_2$

[†] $La(OOCC_2H_5)_3$, $Sr(OOCC_2H_5)_2$ and $Mn(OOCC_2H_5)_2$

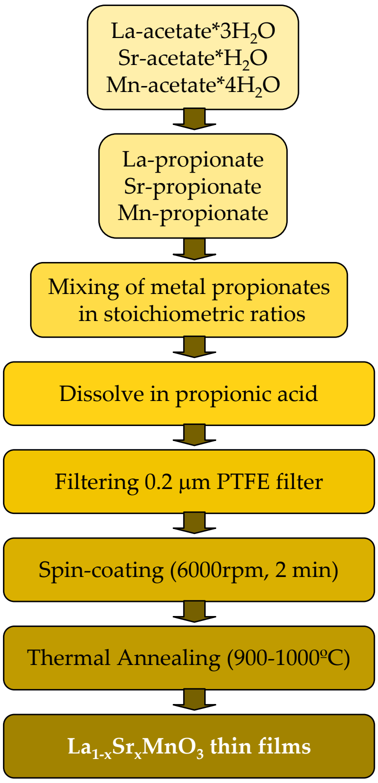

Fig. 7.2: *Flow chart of the preparation process for* $La_{1-x}Sr_xMnO_3$ *thin films by the all propionic in propionic acid route. Adapted from Hasenkox et al.*[72].

Final spin coating solutions were obtained by mixing appropriate amounts of the precursor solutions and dilution to different concentrations with propionic acid. All preparation steps were carried out under ambient atmosphere, which simplifies the synthesis procedure. LSMO films were deposited on (100) $SrTiO_3$ (STO) substrates by spin coating at 6000 rpm for 2 min and annealed at temperatures in the range 900-1000°C under flowing oxygen gas for different annealing times up to 12 h. Using a temperature ramp of $3^oC/min$, both during warming and during cooling, and a oxygen flow rate of $0.6l/min$. Previous studies were performed in the group in order to optimize the parameters of precursor solution and annealing processing[74]. The stoichiometry of the precursor solution was checked by inductively coupled plasma (ICP) that allowed us to obtain a quantitative determination of multi-elements at trace and ultra-trace concentration levels.

7.2.1 Substrate requirements and epitaxy

For the growth of a crystalline thin film the choice of the appropriate substrate is of primary importance. *Julia Phillips*[124] has reviewed the criteria guiding the selection of substrates for high temperature superconductors, which applies to the case of manganites as well. The basic requirements for the substrate can be summarized as follows:

- Chemical stability. It is important that there is no chemical reaction between the film and the substrate. Also there should not be any reaction between the substrate and the oxygen gas required to grow manganites.

- Thermal expansion match. If the substrate and film have different thermal expansion coefficients there might be problems with cracking of the film. From the reported thermal expansion coefficients of LSMO and STO ($\alpha_{LSMO} \approx 11.5 \times 10^{-6} K^{-1}$ at x = 0.33[70] and $\alpha_{STO} \approx 11 \times 10^{-6} K^{-1}$[45]), together with the corresponding room temperature lattice parameters $a_{LSMO} = 0.3873nm$[102] and $a_{STO} = 0.3905nm$, one finds a misfit strain $\epsilon_m = (a_{STO} - a_{LSMO})/a_{LSMO} = 0.83\%$ at room temperature and a smaller value of 0.79% at 800 °C.

- Surface quality. A uniform surface is necessary in order to get a uniform homogeneous film. Defects on the film surface can have a significant impact on the nucleation of the film, and can influence the film morphology and structure.

- Substrate cleanliness. A cleaned surface is a requirement for reproducible results. Usually the cleaning procedure is the result of an empirical process. In our case we put the substrate in acetone in an ultrasonic bath and dry it in a nitrogen flow.

- Substrate homogeneity. If the substrate consist of a small amount of another phase different than the predominant one, this might affect the surface and the film may not grow well on the whole substrate. Twin boundaries that propagate throughout the substrate are potential nucleation sites for competing crystalline directions.

- Substrate thermodynamic stability. It is important that the substrate do not undergo any phase transition in the temperature range that is spanned during the preparation and growth process.

In order to grow epitaxial films there are more factors that should be considered. The term "epitaxy" describe the phenomenon of the oriented growth of crystals of one substance on the crystal surface of another substance. The term has been generalized to thin crystalline films grown in a well-defined orientation on a single crystal substrate.

- Lattice match. The difference in the in-plane lattice parameters should be minimized to get epitaxial films. Differences in lattice parameters can also be a way of changing the properties of the film. In-plane and out-of-plane misfit can be defined as:

$$\epsilon_{//} = \frac{a_{LSMO} - a_{LSMO}^{bulk}}{a_{LSMO}^{bulk}} \times 100 \tag{7.1}$$

$$\epsilon_{\perp} = \frac{c_{LSMO} - c_{LSMO}^{bulk}}{c_{LSMO}^{bulk}} \times 100 \tag{7.2}$$

- Coincidence sites. Not only the lattice constants should be matched but the atoms that coincide should preferably have the same atomic size and valency. This means that a good substrate should have a similar structure to the film material.

- Surface quality. For epitaxial films this factor is even more important. Misoriented grains frequently nucleate on irregularities on the surface.

- Structural quality. Generally one can say that the crystalline quality of the film will be no greater than that of the substrate. Impurity phase inclusions and twins will likely effect the epitaxial quality.

Substrates, however, are much more than merely a chemically inert mechanical support for thin films; they are functional elements which can be used to tailor the thin film properties. They can be prepared as chemically well-terminated atomically flat surfaces as well as with step and terrace structures.

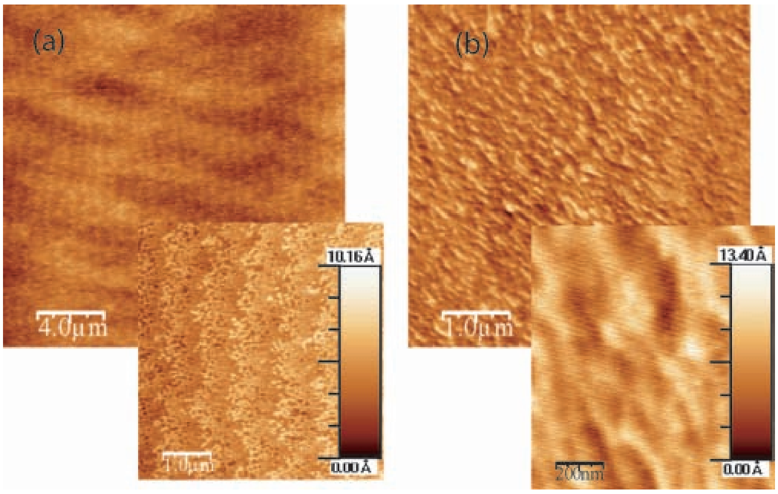

Fig. 7.3: *Topographic SFM images of $SrTiO_3$ surface (a) ($20\mu m \times 20\mu m$) after thermal treatment (900°C-1h) showing large atomically flat terraces and (b) ($5\mu m \times 5\mu m$) without thermal treatment displaying regular flat surface without step formation.*

Figure 7.3a represents a STO(001) substrate with large-area terraces atomically flat interrupted by one unit cell high steps, while figure 7.3b shows regular flat surface without step formation . To reach flat terraces a thermal treatment has been accomplished during 1h at 900°C warming up and cooling down at 3°C/min under a oxygen flow rate of 0.5 l/min. Since not significant differences in magnetotransport properties of LSMO thin films grown in STO substrates after and without thermal treatment are founded, all the samples presented in this report have been grown in STO substrate as-received. We used commercially available $SrTiO_3$ substrates[‡].

The above mentioned reasons make $SrTiO_3$ a good choice as substrate. A summary of properties of substrate materials suitable for complex oxide thin films deposition can be found in reference[118].

7.2.2 Thickness determination

LSMO thin films were deposited on STO substrates from different concentrations of precursor solution and thermal annealing conditions (see sec.3.2.1, p.32). In this way, we have obtained thin films with different thickness which have been determined by direct measurements using a SFM on tracks obtained by optical lithography for resistivity measurements, TEM cross section images or TOF-SIMS depth profiles. In figure 7.4a, TOF-SIMS depth profiles are displayed for a LSMO thin film grown under thermal annealing of 900°C during 1h and starting from a concentration of precursor solution of 0.1M. The film thickness is determined by monitoring the secondary ion count rate of selected elements as a function of time. The analysis uses Cs^+ primary ions and positive secondary ions. To convert the time axis into depth, the SIMS analyst uses a profilometer to measure the sputter crater depth. A profilometer is a separate instrument that determines depth by dragging a stylus across the crater and noting vertical deflections. Total crater depth divided by total sputter time provides the average sputter rate. Thus a thickness of $7-12nm$ can be derived (Fig.7.4a) for a starting concentration of $0.1M$. Similarly, for a LSMO film at 900°C-12h and a concentration of solution of 0.3M (Fig.7.4b) the thickness is evaluated in the range of $20-26nm$. We have also performed direct measurements through SFM in LSMO lithographed films (see sec.7.11, p100). The film thickness derived from these measurements are in good agreement with TEM average thickness determination.

[‡] The supplier was *Crystec GmbH*, Berlin.

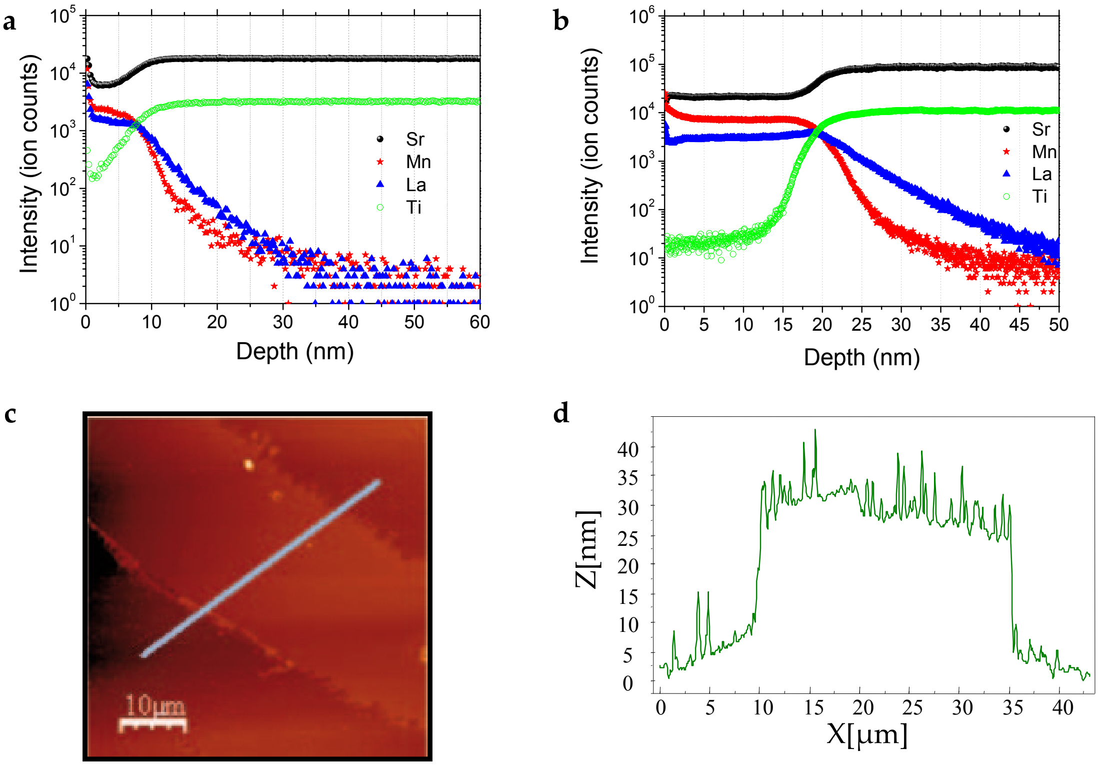

Fig. 7.4: *Film thickness determination in LSMO thin films on STO substrates. (a) TOF-SIMS depth profile for LSMO film grown at 900ºC-1h for with a precursor solution of 0.1M and (b) for 1000ºC-12h with 0.3M. (c) Topographic SFM image (50 γ 50 γ) in a lithographed track of LSMO film grown under 1000ºC-12h and a solution concentration of 0.3M. (d) Average profile taken in line of image (c).*

7.3 Chemical characterization

7.3.1 SIMS

Secondary ion mass spectrometry (SIMS) is based on the mass spectrometric analysis of ions, which are generated by the interaction of a primary ion beam (keV range) with a sample (Fig.7.5). The mass to charge ratio (γ) of the species are analyzed and yields positive and negative secondary ion mass spectra consisting on the ion γ versus the number of ions detected at each γ . During SIMS analysis, the sample surface is slowly sputtered away. Continuous analysis while sputtering produces information as a function of depth, called a depth profile. When the sputtering rate is extremely slow it is called static SIMS in contrast to dynamic SIMS used for depth profiles. Depth resolution depends on flat bottom craters, the redeposition by sputtering from crater wall onto the analysis area or direct sputtering on the crater wall.

The ToF-SIMS instrument used for this thesis is an ION-ToF IV system situated at the Parc Cien-

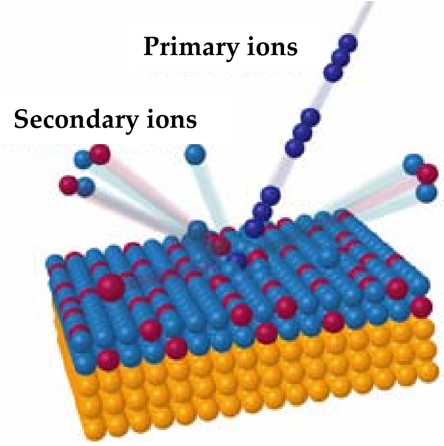

Fig. 7.5: *A schematics drawing of the secondary ion emission process initiated by the impact of a primary ion. Extensive fragmentation occurs near the collision site producing mainly atomic particles. Away from the point of impact collisions become less energetic resulting in the emission of larger molecular fragments.*

tific of Barcelona. This mass spectrometer enables to analyze an unlimited mass range with high sensitivity and quasi-simultaneous detection of all secondary ions collected by the mass spectrometer. But, since the technique uses a mass spectrometer, the SIMS analyst must be aware of the possibility of mass interferences. This is the occurrence of two or more secondary ions with the same nominal m/z. Especially in oxides compounds where the number of possibilities for mass interferences increases drastically. Also it is important to note that the charge of the detected ion is not determined by the charge state of that species in the matrix. Furthermore, quantitative SIMS analysis is difficult because the secondary ion yields (fraction of sputtered atoms that become ionized) depend on several factors and are not directly proportional to its concentration in the sample. More information about these concerns can be found in the review of *Van Vaeck et al.*[167].

7.3.2 EELS-EFTEM

Based on the particle character of electrons, we can divide electron scattering into elastic and inelastic scattering. An electron that undergoes elastic scattering is assumed to interact with matter with no energy loss, while in the case of a elastically scattered electron, a measurable loss of energy is assumed. Released energy can be emitted as X-rays, which carries information about the atoms that produced it and thus chemical information from the material under investigation. Inelastically scattered electrons as the result of the ionization of atoms by the primary electrons are measured in electron energy loss analysis (EELS) and energy filter transmission electron microscopy (EFTEM) analysis. These electrons carry chemical information about the ionized atom.

EELS/EFTEM experiments were performed and analyzed by P. Abellán, F. Sandiumenge and M.-J. Casanove using equipment from "Serveis Cientifico-Tècnics" of the Universitat de Barcelona (UB), Universitat Autònoma de Barcelona (UAB) and CEMES (Toulouse). The used microscopes and technical parameters are mentioned within the experimental methods of the respective chapter.

7.3.3 Photoemission electron microscopy

Photoemission Electron microscopy (PEEM) allows element selective imaging profiting of core-level excitation of photoelectrons or secondary electrons within the so called soft X-ray range ($200 - 2000eV$). The escape depth of the electrons limits the probed depth to $2 - 4nm$. Such a limited near surface sensitive allows, in a rough way, interpreting percentual variations of the integrated spectral intensity as percentual variations of the number of cations/ions.

PEEM experiments were performed and analyzed by S.Valencia and F.Kronast in Helmholtz-Zentrum, Berlin. Technical parameters are mentioned within the experimental methods of the respective chapter.

7.4 Structural characterization

X-ray diffraction (XRD) is useful method to identify crystal structure and investigate thin film crystalline quality by detecting the diffracted X-ray. Diffraction is a coherent and elastic scattering phenomenon of an incident electromagnetic wave, where the periodic lattice of a crystal diffuses in a coherent way the X-rays. For constructive interference according to Braggs law we know that

$$n\lambda = 2d_{hkl}Sin\theta \tag{7.3}$$

where n is the reflected order, d_{hkl} is distance between parallel (hkl) planes of crystal, λ is the wavelength of X-ray source and θ is the angle between incident X-ray beams and crystal plane. Fig. 7.6a shows a schematics of Bragg diffraction condition.

In our study, to investigate the highly epitaxial grown LSMO films, XRD measurements were performed with two different two circle diffractometers, Rigaku Rotaflex RU200B and Siemens D5000 with Cu X-ray source ($\bar{\lambda} = 1.5418\mathring{A}$, $\lambda\left(K_{\alpha1}^{Cu}\right) = 1.5405\mathring{A}$ and $\lambda\left(K_{\alpha2}^{Cu}\right) = 1.5443\mathring{A}$) and a four circle General Area Detector Diffraction System (GADDS) introduced by Bruker AXS with a two-dimensional (2D) area detector, located at the ICMAB.

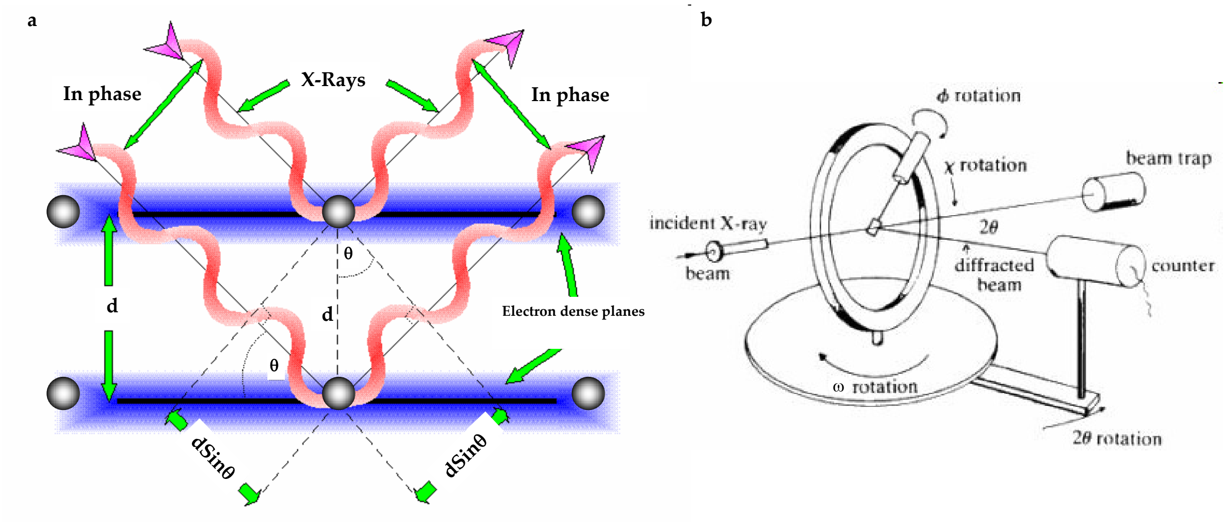

Fig. 7.6: *(a)Schematics of X-ray Bragg diffraction. (b) Sketch of an X-ray diffraction system displaying the angles and their relationship to sample surface for XRD measurements.*

A diffractometer system, as shown in Fig. 7.6b, consists of an X-ray source, sample holder stage and a detector. Different configurations of X-ray source, thin film sample and detector can be performed in order to get different information, namely:

- $\theta - 2\theta$ scan: It provides information about the crystal orientation of the substrate and thin films and about the out of plane lattice parameters. Thin film samples with a mixture of single crystal, random polycrystalline layers and highly textured layers can be measured with all the features appearing simultaneously in diffraction frames by using GADDS with 2D detector. For the calculation of the out of plane lattice parameter the diffraction pattern was shifted as much as necessary to achieve the STO reference angle. After that, a pseudo-Voigt fitting function of the peak is performed to determine accurately the peak position (Fig.7.7).

  Finally, since the $La_{0.7}Sr_{0.3}MnO_3$ bulk phase is rhombohedral at room temperature with the pseudocubic parameter a 3.873Å[102], we can calculate the lattice parameters considering a cubic system:

$$d_{hkl} = \frac{a}{\sqrt{h^2+k^2+l^2}} \Rightarrow \sin^2\theta = \frac{\lambda^2}{4a^2}\left(h^2+k^2+l^2\right) \tag{7.4}$$

- *Rocking curve* or ω scan: Crystal texturing or mosaic of thin films can be investigated by this measurement. The full width at half maximun (FWHM) $\Delta\omega$ of the rocking curve of a low indexed peak is indicative of the crystalline quality of the sample.

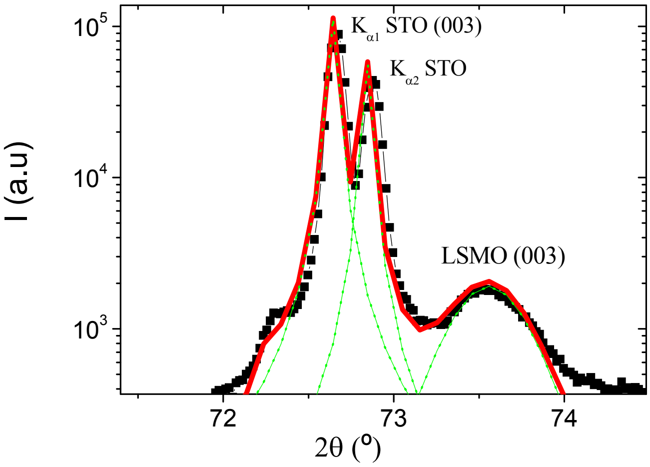

Fig. 7.7: *Zoomed $\theta - 2\theta$ scan of (003) LSMO and STO reflections from a LSMO film of 60 nm grown under 1000°C-12h annealing. Fitted curves by using pseudo-Voigt functions are indicated for $\lambda(K_{\alpha1})$ and $\lambda(K_{\alpha2})$ (003) reflection for STO and LSMO film. The total fitting curve (sum of pseudo-Voigt contributions from STO and LSMO) is also indicated.*

- *Pole figures* or ϕ scan: It is used to represent the orientation distribution of crystallographic lattice between film and substrates. Oblique planes of film and substrate were commonly used to determine in-plane orientation.

- *Reciprocal space maps (RSMs) or Q-plots*: They provide in-plane lattice parameters. Executing a series of $\omega - 2\theta$ scans at fixed ϕ and χ around particular asymmetric reflections of substrate and film peak, we can get through a complete area of the reciprocal space. Thus, it is possible to obtain a map of the reciprocal space. To get information about the lattice parameters, the scan axis must be changed from θ and ω to the wave vectors parallel to the surface Q_x and perpendicular to the surface Q_y with the following relations:

$$Q_x = \frac{\lambda}{2} sin\theta sin(\theta - \omega) \tag{7.5}$$

$$Q_y = \frac{\lambda}{2} sin\theta cos(\theta - \omega) \tag{7.6}$$

where λ is the wavelength of the incident X-ray beam and Q_x and Q_y are the equivalent reciprocal space distances on the equivalent real space distances. Absolute values of in-plane a and out of plane parameter c can be extracted from the position of the peak, again corrected by a ω and θ shift deduced from the substrate peaks with:

$$a = \frac{h}{Q_x} \tag{7.7}$$

$$c = \frac{l}{Q_y} \tag{7.8}$$

where h and l denote the Miller indices of the peak.

7.4.1 Transmission Electron Microscopy

The basic principles for understanding how transmission electron microscopy (TEM) works are similar to those from the optic microscopes[177]. With transmission electron microscopy, a thin ($< 200nm$) sample is bombarded by a highly focused beam of single-energy electrons generated by termoionic discharge in a cathode or by field emission which afterwards are accelerated by an electric field. The beam has enough energy for the electrons to be transmitted through the sample. The transmitted electron signal is greatly magnified by a series of electromagnetic lenses up to atomic resolution. The magnified transmitted signal can be observed in two ways, through electron diffraction or direct electron imaging. Electron diffraction patterns allows observing the diffraction pattern of the studied material, and thus information about the unit-cell can be deduced. Direct electron images yield information about the microstructure of different phases, their orientation and size.

HRTEM experiments were performed and analyzed by P. Abellán, F. Sandiumenge and M.-J. Casanove. The used microscopes and technical parameters are mentioned within the experimental methods of the respective chapter.

7.5 Transport properties analysis

Electric transport measurements have been performed using a Physical Properties Measurements System (PPMS) from Quantum Design located at the ICMAB. The system has a 9 T superconducting magnet and a helium cryostat which allows a precise temperature control between 1.8 K and 400 K. The system incorporates a nano-voltmeter and a dc/ac current source which provides currents down to $1\mu A$ and up to 2A with a resolution of $0.1\mu A$. Vacuum grease is used when mounting the sample in order to ensure a good thermal coupling. Additionally a thermometer is found just below the sample mounting space to monitor the sample temperature.

In order to determine the resistivity of the thin films we have used the four-point configuration. Thus, the resistivity has been obtained avoiding the contribution of contact resistivity.

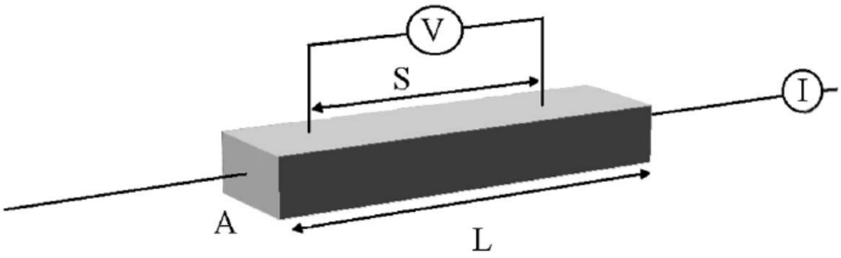

Fig. 7.8: *Schematic view of the four-point configuration. I denotes the current through the sample, L, the length and, A, the cross sectional area, of the sample, V, the difference of voltage measured between two separated points by a distance S.*

To compute quantitative data the geometry of the sample has to be considered, thus the resistivity of a film is calculated by

$$\rho = R\frac{A}{S} = \frac{(V_1 - V_2)}{I}\frac{tw}{S}$$

where R is the resistance measured and derived from the difference between voltages $(V_1 - V_2)$ of two separated points of the sample and the current I that through between them , A, the cross sectional area is defined as the product of thickness (t) and the width (w) of the film and S is the distance between the contacts. A sketch of this configuration is displayed in figure 7.8.

In this regard, important error sources exist when the silver paint contacts technique is used because the inaccuracy of the distance existing between them crucially determines the uncertainty resistivity. In figure 7.9 is displayed an illustrative example of our silver paste contacts on LSMO thin film, where four Ag wires (0.125 mm of diameter) were directly attached to the film with silver paste. A general view is shown in (a), where a non regular distance between contacts is identified. The dispersion in the separation distance, amounting up to several hundred of microns (b), disable any quantitative data of the resistivity.

In addition to the geometrical limitation, silver paste contacts yield to noisy and non reproducible resistance measurements as it is shown in figure 7.10a. Also this kind of contact presents a time consuming limitation because a rate higher than $3^{\circ}C/min$ would be able to break the contact with the film.

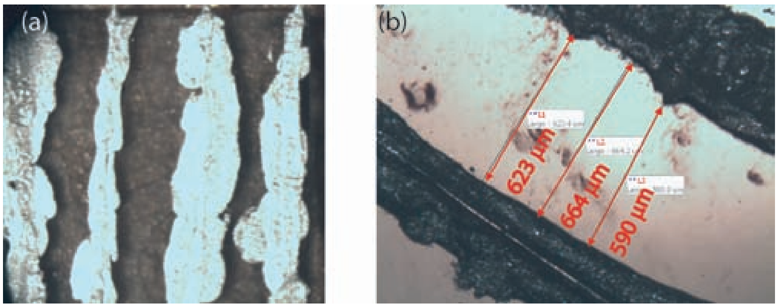

Fig. 7.9: *Optical image of a LSMO film with silver contacts. (a) General view showing the four-point configuration using silver paste contacts. (b) Zoom in the central region of image (a), where a single electrical pads is shown.*

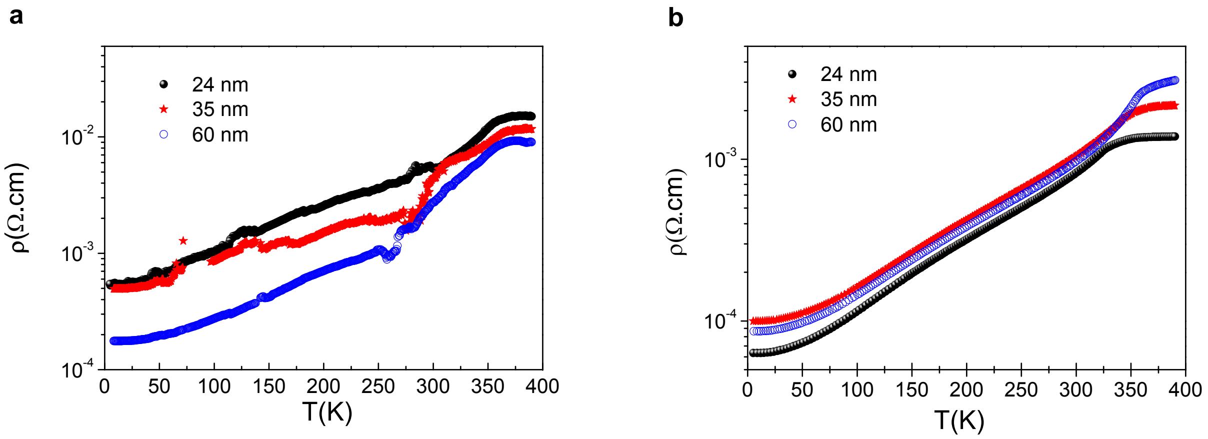

Fig. 7.10: *Temperature dependence of resistivity measured in LSMO thin films with different film thickness using two different contact methods. (a) Contacts prepared by direct attachment of Ag wires with silver paste. (b) Contacts performed by Ag and Au evaporated on the LSMO surface and In wires welded on top.*

To ensure well defined geometries while having large areas where any possible inhomogeneity would be averaged out, lithographed films were prepared through standard photolitography with track widths of 20 μm (Fig.7.11b) and 600 μm (not showed) and voltage taps separated by 2 mm and 1.3 mm, respectively. The photolithographic methodology used, will be explained next. On the other hand, to achieve good quality for the electrical contacts and to avoid contact deterioration during the measurement Ag ($1\mu m$) were evaporated onto the LSMO films, capped with 30 nm of Au and cured by annealing during one hour at 400°C under a flowing oxygen (0.4 l/min). The configuration of contacts tap is displayed in figure 7.11a.

This configuration, two taps for current in the corners of the film ($1.6mm \times 1.6mm$) and four voltage taps in the middle region ($1.6mm \times 1mm$), allows us to performs three-point and four-point

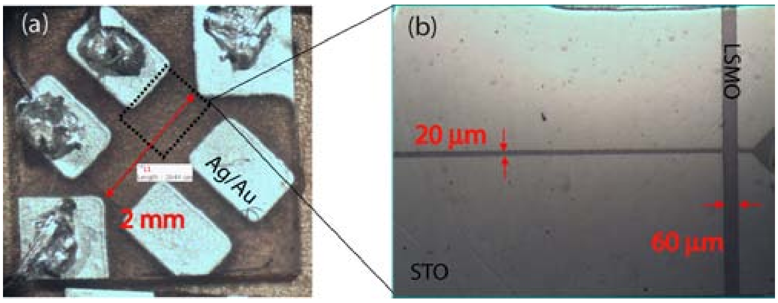

Fig. 7.11: *(a) Optical micrograph of a lithographed sample and (b) magnification of the lithographed tracks.*

configuration measurements in the same film in order to calculate the resistance contact value and the resistivity of sample, respectively (Fig.7.12). After that, the Ag wire was welded with Indium at moderate temperature (350°C) in order to take care to not degrade the surface of the film. A sketch of the film linked by wires to the PPMS holder is displayed in figure 7.12.

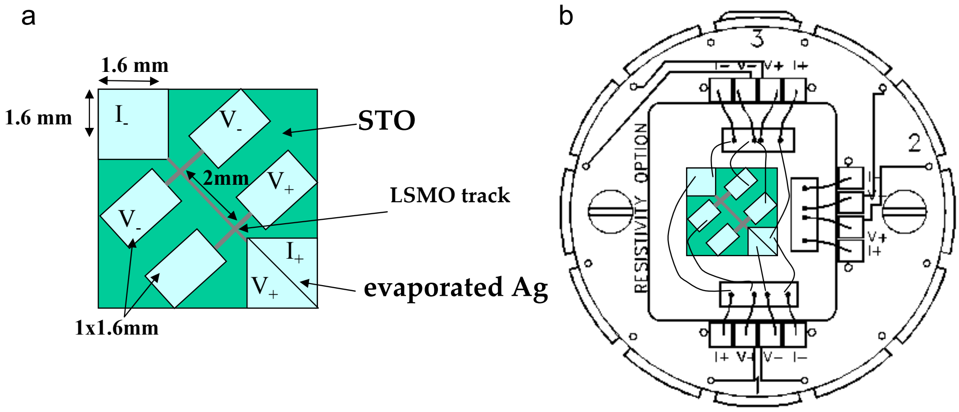

Fig. 7.12: *Resistance contact determination. (a) Planar view sketch of lithographed film. (b) Contact architecture displaying the film onto PPMS holder setup designed to measure the resistivity of LSMO film obtained by four-point configuration (channel 3) and to determine the contact resistance by three-point configuration (channel 1).*

In this way, the quality of electrical contacts has been ascertained from the difference between four and three point configuration for two lithographed LSMO films grown in the sames conditions (1000°C during 12h). Figure 7.13 displays several IV curves using contacts based on Ag evaporated and wires welded with Indium (a) and contacts directly attached with Silver paste (b). Calculating the slope of each IV characteristic we obtain the resistance of the two kinds of contacts. In the case of contacts based on Ag evaporated and wires welded with Indium, the contact resistance is under our PPMS sensitivity ($R < 10^{-6}\mu\Omega$). On the contrary, high resistance values were obtained for contacts with Silver paste ($R = 340\Omega$). But the relevant parameter to work with is the resistivity contact

($\rho_c = R_c A_c$) which considers geometrical factors of contact taps. Thus, electrical contacts with high resistivity values ($\rho_c = 8.5 \Omega cm^2$) consisted of wires direct attached of LSMO film with Silver paste, whereas low resistivity contacts ($\rho_c = 0.2 \mu\Omega cm^2$) were obtained by using Ag wires welded with In to Ag contacts evaporated onto LSMO film.

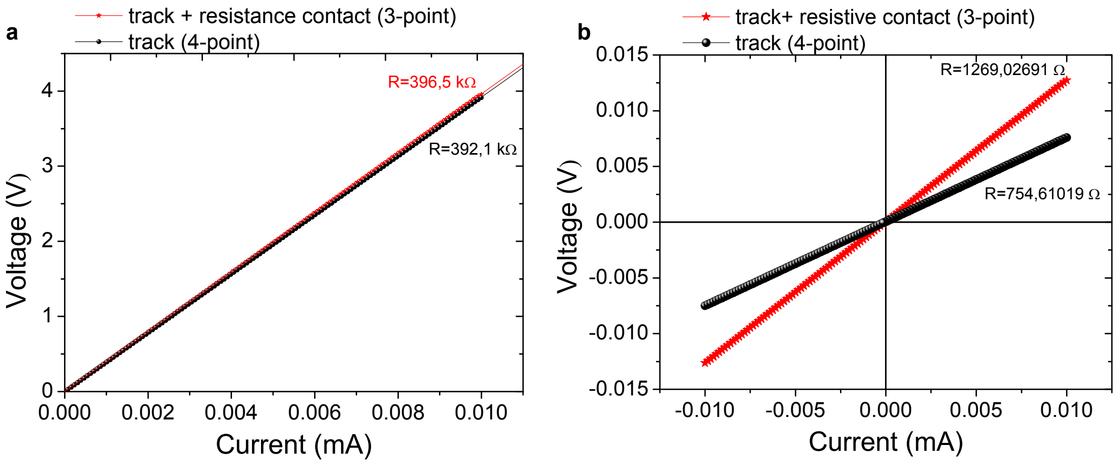

Fig. 7.13: *Contact resistance determination. I-V characteristics determination using Ag wires welded with indium (a) and using Ag wires directly attached with silver paste (b) to Ag contacts evapotared onto the LSMO film. The difference between 4-point and 3-point configuration is used to obtain the resistance contact values.*

Note that the differences between figure 7.13(a) and (b) in the voltage scale are produced by differences in the lithographed track widths, (a) with a width of 20 μm and (b) 600 μm. The values of contact resistivity ($\rho_c = R_c A_c$) obtained are in agreement with those achieved in high-T_c superconductors[88].

7.5.1 Photolithography and etching of LSMO films

Micrometric wide tracks on LSMO thin films are defined by using optical lithography. This kind of lithography is cost-effective and a simple method that allows to obtain track width of $10-20 \mu m$. The experiments were carried out in the clean room facility of the UAB.

Photolithography is based on the interaction of ultraviolet (UV) light and photosensitive materials, namely photo-resists. Schematically, the process is as follow:

- Cleaning of the film with acetone and methanol to get rid of the organic and ionic impurities.

- A drop of photo-resists (Shipley Microposit 1813) is deposited at the LSMO film surface and dispersed by spin-coating at 1500 rpm/s, 3500 rpm during 45 s. A positive photo-resist with photo-active components can be removed using a suitable developer.

- The film then is placed in a hot plate kept at 100ºC during 60 seconds to remove the organic solvent of the resist.
- The film is then aligned with the mask containing the desired pattern using a mask aligner.
- The resist is exposed during 15 seconds and then developed for 30 seconds using the Microposit MF-321 developer in order to transfer the desired pattern into the photo-resist.
- A final treatment of the remaining photo-resist includes a hard bake at 100ºC for 30 min.
- Dipping the sample on a bath of $H_2SO_4(30\%) + H_2O_2(26\%) + H_2O(44\%)$ the LSMO thin film is attacked. But, in order to control the attack of the film, the solution was diluted two times with $H_2O(2\%)$. The etching processes was optimized by M. Bibes[15].

This methodology has been adapted from that used to obtain superconducting lithographed films within the superconductivity group[64] of ICMAB.

7.6 Magnetic characterization

7.6.1 SQUID DC-Magnetometer

A superconducting quantum interference device (SQUID) DC-Magnetometer was used to investigate the magnetic response of LSMO thin films. A SQUID consists of a superconducting loop and a weak link, the so-called Josephson junction. These devices give rise to an output voltage signal, which is a periodic function of the flux threading the superconducting loop in which one or two weak links are inserted. This geometry is termed dc-SQUID (constant bias current).The magnetometer includes a SQUID detection system and a precision temperature control unit in the bore of a high-field superconducting coil. The sample is located inside the superconducting coil so that a uniform dc-magnetic field is applied. The detection system is based on a set of pickup coils which are placed in the center of the superconducting coil; the sample is then displaced through the coil set, inducing a current in the detection coils proportional to magnetic flux variation. The signal is amplified by means of a SQUID sensor which converts current to voltage achieving a high sensibility. Hence, the magnetic moment induced by the sample is proportional to the voltage variations that the SQUID detects, which can resolve magnetic moments as small as $10^{-9}Am^{-2}$ ($10^{-6}emu$). All the system is placed inside a helium cryostat which refrigerates the superconducting coil and allows a precise temperature control between 1 8 and 400 . Isothermal and temperature dependent magnetization curves were measured with two commercially available Quantum Design SQUID magnetometers provided with 5 5μ and 7μ superconducting coils. These equipments are integrated in the low temperatures and magnetometry service of ICMAB .

The isothermal magnetization curves showed normally a negative slope of the magnetization at high magnetic fields, due to the diamagnetic character of the substrate. This contribution was eliminated by high fields data linear fit subtraction.

7.7 Tracking regions for finding nanoscale modifications

In order to locate nanometric motives, we have performed nanoindentations at the LSMO film surface. This marks are easy to find by a simple optical microscope. Several squares were usually drawn in order to carry out a variety of experiments inside of each square. The lateral size of the squares is 50 γ , under the maximum scan range of piezoelectric SFM. In figure 7.14a two optical images are presented. The upper image shows SFM cantilever and tip with a spot laser diffraction on it. The bottom image display a zoom of upper image where the distances between indentation delimited squared are typed.

A quick inspection of the surface morphology and the electrical characterization provided by the SFM technique herself, allows us to confirm that this method perturb the surface film only few micrometers around it. Thus, the inner region of the square delimited by four indentations is available to performed desirable nanoscale modifications by using SFM.

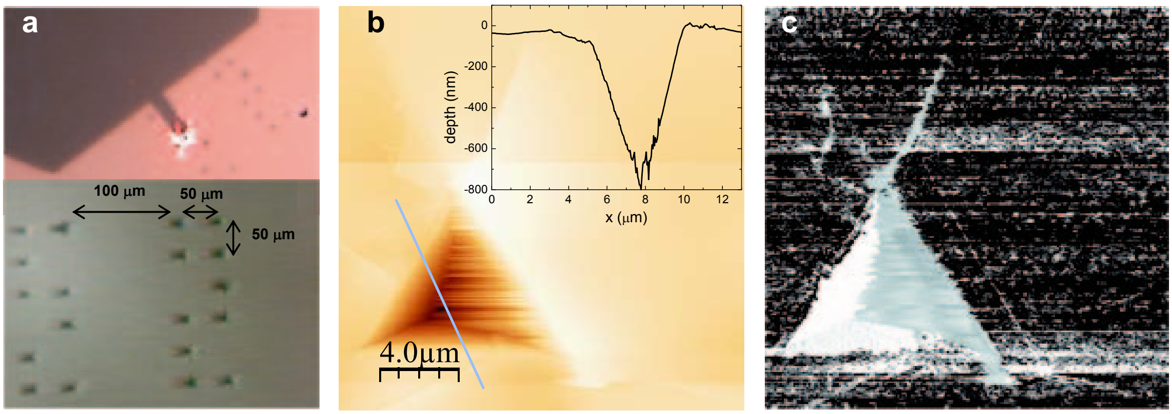

Fig. 7.14: *(a) Optical images displaying indentations marks. (b) and (c) Topography and current map showing the indentation on LSMO thin film of 8 nm thickness grown on STO substrate. Current map current colour goes from 0 nA (white) to 100nA (black). The depth of the indenting hole is about 800 nm.*

In figure 7.14b a topographic image is shown with a current map obtained simultaneously shown in (c). Despite of the depth reached by the indentation tip is of about 800 nm, the film around it remains unaltered, morphologically and electrically. The force applied during nanoindentation (400 mN) has been optimized on STO substrates by Jone Zabaleta[87].

7.8 Scanning force microscopy

The dawn of the scanning probe microscopy (SPM) came in 1982 with the invention of the scanning tunnelling microscope (STM) by Heinrich Rohrer and Gerd Binnig[18]. As its name indicates, this technique is based on the quantum tunnelling effect, which formulates that a current can flow between two electrodes separated by a thin insulator or a vacuum gap. In this microscope, a sharp metallic tip is brought close to a conductive surface and, upon applying a voltage, a current flows between tip and surface provided their separation is small (in the nanometre range). In a standard experiment the tip, attached to a piezoelectric actuator, is moved in three dimensions over the surface while an electronic controller keeps the tunnelling current constant by means of a feedback loop that varies the tip-sample distance. This distance is recorded as a function of the tip lateral position and displayed as a microscopic image. Typical applied voltages and measured currents are in the range of mV to $\backsim 3V$ and pA to nA. These voltages result in large electric fields ($\backsim 10^{10}\ V.m^{-1}$) localized near the tip apex which implies that the tunnelling current flows from the very last atom of the tip apex to the single surface atom below, inherently providing atomic resolution. The exponential dependence of this current on the tip-sample distance is the key point in the success of STM, in terms of resolution, since for typical tip-sample systems, a change of only 0.1 nm in the distance results in one order of magnitude difference in the measured current. The invention of the STM immediately triggered the development of several other techniques that sense local properties of surfaces giving rise to the so-called SPM family. Generally speaking, in any scanning probe microscope, a short-range interaction is sensed by a local probe which is scanned over the surface under study. The magnitude of interest is measured, recorded and processed by a computer system. The scanning force microscopy (SFM) was the first extension of the STM[17]. In this case, the metallic tip is replaced by a force sensor, so-called cantilever, to measure the interaction forces acting between probe and sample. These forces are usually in the range of nN to μN and, though atomic resolution can be achieved, typical lateral resolution ranges between 5nm and 20nm depending on the sharpness of the probe. Vertical distances can be measured with an accuracy of $\backsim 0.1$ nm. Besides surface topography, the probe-sample interactions also reveal information about lattice symmetry, adhesion, friction, elasticity, wear, etc...

with unprecedented spatial resolution. The success of the SFM technique mainly arises from the possibility to image surfaces independent of their conductivity properties, a severe limitation of the STM technique. But SPM in general and SFM in particular, offer much more than just imaging. Some alternative and outstanding applications of SPM in the field of material science have been collected in[98].

7.8.1 Components of the scanning force microscopy

The force sensor

Strictly speaking, the SFM does not measure forces but the bending and torsion of a lever (also called cantilever), induced by the forces acting on a nanometer-sized tip attached to one of the lever ends. Therefore, this cantilever has to be as soft as possible to be able to detect forces down to the pN. Ideally, the stiffness should be below interatomic spring constants, which are typically in the range of $10-20\ nN.nm{-}1$. To achieve this and additionally prevent the transmission of external vibrations to the cantilever, its effective mass has to be as small as possible. Today, such cantilevers with integrated tips are commercially produced by standard microfabrication techniques, mostly from silicon or silicon nitride. The later use of a coating layer allows producing tips with different surface properties (conductive, magnetic...).

The deflection sensor

Different techniques have been proposed to detect the small bending of the cantilever due to tip-sample forces[139]. Though in the first SFM setup, this deflection was measured with an STM tip (since the backside of the cantilever is metalized, a tunnelling tip was brought close to it, to measure the normal deflection[17]), subsequent designs simplified the original by using optical (interferometer, beam reflection) or electrical methods (piezoresistive, piezoelectric). Our systems employ the optical beam deflection method, proposed in[4,107] and found nowadays in most of the microscopes. Within this method, a laser beam is focused on the rear metalized side of the cantilever and the reflected beam is collected by a segmented position-sensitive photodiode. Each sector of the photodiode generates a voltage proportional to the intensity received. If the photodiode is segmented in four quadrants (as in our systems), the normal bending and the torsion of the cantilever can be separated and quantified[108]. A schematic drawing of our setup is shown in figure 7.15. In the absence of forces the laser spot is centered, i.e. equal signals are measured in each of the four sectors. When a force acts on the tip, the lever is deflected and the reflected spot is displaced. As depicted in part (a), normal forces produce a vertical bending of the cantilever that is proportional to the signal difference between the upper and lower halves of the detector ($_{\theta}$). Similarly, the main effect of lateral forces is the torsion of the cantilever (part (b)), which is proportional to the signal difference between the right and left halves of the photodiode ($_{1}$ $_{2}$).

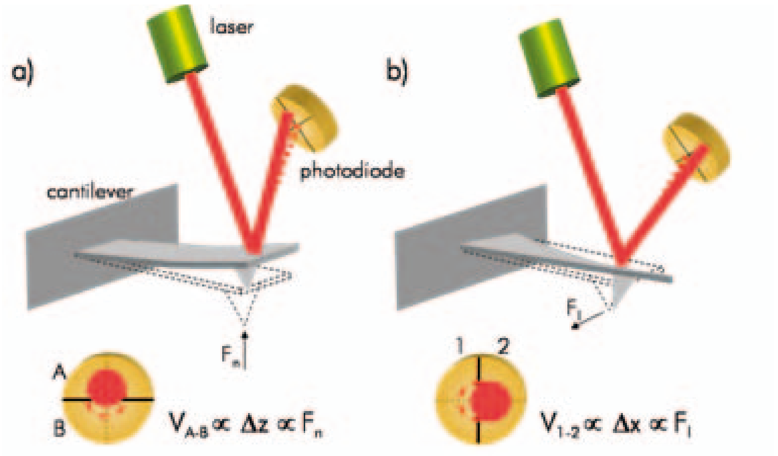

Fig. 7.15: *Schematic representations showing the optical detection method used to measure the cantilever displacement produced by normal (a) and lateral forces (b). Dashed cantilever and laser paths represent their respective position in the absence of forces. At this position and* $_{1}$ $_{2}$ *are adjusted to zero. Normal forces are proportional to the signal whereas lateral forces, to the* $_{1}$ $_{2}$ *signal.*

The scanning system

The scanning probe needs to be positioned with an accuracy of 1 pm if atomic resolution is required. This is usually achieved by attaching either the tip or the sample (this latter is the configuration used in this work) to piezoelectric actuators. These generally consist of lead-zirconate-titanate (PZT) ceramic materials placed between two metal electrodes. When a potential difference is applied across the electrodes, the piezoelectric ceramic expand or contract in a direction that is perpendicular to the applied electric field. The motion of the ceramic is controlled by the polarity and magnitude of the applied voltage. The tube shaped piezoelectric actuator of figure 7.16 is the most frequently used in SFM. It is a hollow cylinder that has one electrode on the inner surface and four equally spaced electrodes on the outer surface. Biasing the inner electrode controls the tube's motion in the direction, part (a). This change will be referred to as the piezo displacement ( ) from now on (though we use the same symbol, it can differ from the vertical cantilever displacement). Biasing two opposite outer electrodes moves the tube in the and directions, part (b). If and are small, this provides the scan area (,) on the surface plane of a typical SPM image.

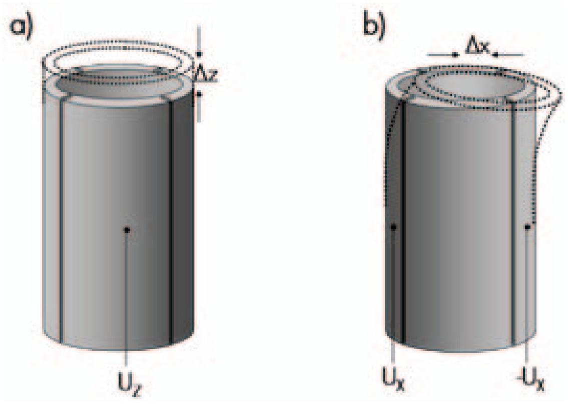

Fig. 7.16: *Schematic representation of the response of a tube-shaped piezo actuator to an applied voltage between the internal and external electrodes (a) and two opposite external sectors (b).*

The Control Unit

A high voltage unit connected to a digital signal processor (DSP) inside a PC basically complete our experimental setups. The DSP board is mainly in charge of collecting the signal coming from the photodiode and controlling the movement of the piezo. Due to the limited voltage range of the DSP (3 V) and the high voltages required by the piezo to work (up to 300 V), the signal is amplified and supplied to the microscope through a high voltage unit. The amplification gain is selected by the user depending on the vertical and lateral scales of the sample under study: lower gains imply smaller scanned area but increased resolution. The DSP is also in charge of the so-called feedback loop, a way to control the vertical distance between tip and sample by maintaining a selected magnitude fixed to a preset value during the scanning. Throughout this work the magnitude used has been the normal deflection of the cantilever, i.e. the normal load. By means of the feedback loop, this deflection and the preset setpoint are continually compared at each point of the image. If they are not equal, a voltage is applied to the scanner in order to move the sample closer to or further from the probe, to maintain constant the normal load. This applied voltage is the signal used for generating the SFM image.

7.8.2 Relevant tip surface interactions

The operation principle of a scanning force microscope is the detection of the force acting between probe and sample. This force can have different origins and contributions and, depending on the tip-sample system under study, the predominant interaction mechanism might vary. In this section we describe the most relevant forces for the work presented here. More detailed information on intermolecular and surface forces can be found in the book[83].

Short range forces: these forces arise from the overlapping of electron wave functions and from the repulsion of the ion cores. Their range is comparable to the extension of the electron wave functions, i.e. less than one nanometer. They can be either attractive (as for example in bond formation) or repulsive (due to the Pauli exclusion principle). As stated in the compilation work by Meyer and coworkers[106], the magnitude of attractive short-range forces is around $0.5 - 1$ nN and the decay length around $0.2 - 0.3$ nm. Akin to the tunnelling current in STM, when these forces are predominant, true atomic resolution is possible in scanning force microscopy imaging[111]. When the short-range repulsive forces are predominant, the tip and the sample are considered to be in “contact” and, though lattice periodicity is possible for well ordered systems, true atomic resolution is however limited.

Van der Waals forces: we already mentioned this interaction when considering the intermolecular forces in self-assembled monolayers. In fact, these are dipole-dipole interactions always present between molecules and atoms. The most important are not those between permanent dipoles but the so-called dispersion forces, which act between dipoles arising from fluctuations and dipoles induced in their electric field. In order to model this interaction in SFM, macroscopic bodies rather than individual atoms or molecules are considered. The tip-sample geometry can be well approximated as a sphere approaching a plane and the van der Waals interaction for such configuration has the form:

$$F_{vdW} \approx -\frac{AR}{r^2} \tag{7.9}$$

where R is the sphere radius, r is the sphere-plane distance and A is the Hamaker constant. The order of magnitude of this constant, which accounts for the materials involved, is $\backsim 10^{-19}$J[83]. In vacuum or air, this van der Waals interaction is always attractive. However, in other media the interaction can be attractive ($A > 0$) or repulsive ($A < 0$), depending on the dielectric constant (ϵ) and the refractive index (n) of the tip, the sample and the medium in-between. For example, a medium with ϵ and n close to the respective values of the tip and sample greatly reduce the van der Waals forces compared to the vacuum. This interaction acts between the surface and the mesoscopic tip end, i.e. not only the end atoms of the tip, and for typical tip-sample systems (e.g. Si_3N_4-Au in air) and tip radius $R = 30$ nm, the van der Waals force at a distance $r = 0.5$ nm is of the order of $F_{vdW} = 4$ nN.

Friction and adhesion forces: during sliding, a macroscopic object has to overcome an opposing force which results in a loss of kinetic energy and, if no additional energy is supplied, the object finally stops. This force, that opposes the relative motion between objects in contact, is the friction force. In the SFM setup, friction causes the torsion of the cantilever when the tip is scanned over the sample as shown in figure 7.15b. These lateral forces can be exploited to form an image or map of the energy dissipated. This contrast might arise from mechanical and/or chemical differences between regions.

Adhesion is the molecular attraction exerted between bodies in contact and can be defined as the free energy change to separate unit areas of two media from contact to infinity in vacuum or in a third medium[83]. Moreover, in SFM working under ambient conditions, there is another important contribution to the adhesion force coming from the water meniscus that forms between the tip and substrate due to adsorption of thin water films at surfaces and subsequent capillary condensation[39]. The formation of this meniscus produces an attractive adhesion force that depends on the relative humidity and the hydrophilicity of tip and sample. The final expression for this force between a sphere and a plane is:

$$F_{adh} = 2\pi R_{\gamma}(cos\theta_1 + cos\theta_2) \tag{7.10}$$

with R the sphere radius, and the contact angle of the respective surfaces and the liquid and the surface tension of the water. Even for low relative humidity, the order of magnitude of the adhesion force due to capillary condensation for typical silicon nitride tips, at a distance of 0.5 nm, is $\backsim 10^{-8}$ N which is comparable to the forces used in SFM experiments. In the present work adhesion has been used only to check and verify tip conditions.

Electrostatic forces: these forces act between localized charges on insulating tip and samples. Their strength and distance dependence obey the Coulomb's law and are usually stronger than other long-range interactions such as the van der Waals or the magnetic interaction. Between conducting tip and sample, electrostatic forces appear when they are at a different potential. If one considers the tip-sample system as a capacitor, the force is given by:

$$F_{el} = \frac{\partial C}{\partial z}(U_{bias} - U_{cpd})^2 \tag{7.11}$$

where U_{bias} is the bias voltage applied between tip and sample and U_{cpd} is the contact potential difference caused by their different work functions. The capacitance, C, depends on the tip-sample distance, the geometry of the system and the dielectric constant of the medium in-between. Therefore, the force also depends on these parameters, which are included in the derivative of the capacitance. From equation 7.11 it is inferred that a zero bias voltage does not normally correspond to a minimal electrostatic force, since the contact potential difference is not compensated. Due to the long-range character of these forces, electrostatic interactions act between the sample and the whole cantilever. Only for very small tip-sample distances ($\leq$ 2 nm), the electrostatic force contribution from the end of the tip dominates over the other terms[60]. The capability of measuring electrostatic forces has been used during the present work by means of Kelvin probe microscopy, which is described later on.

7.8.3 Operation modes in SFM

The rich variety of interactions that can be detected in SFM has made possible a wide variety of operation modes. The schematic force-distance relation shown in Fig.7.17 illustrates that different interactions are expected, depending on the distance separating the sample and the probing tip.

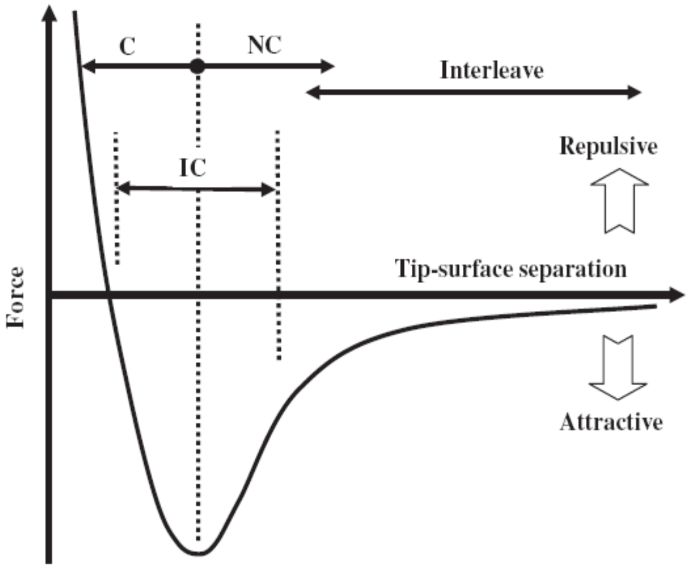

Fig. 7.17: *A sketch of the dependence of force on sample tip separation showing the regimes in which contact (C), non-contact (NC), intermittent contact (IC), and interleave imaging are performed. Also shown are domains of repulsive and attractive tip-surface interactions. From Kalinin et al.*[146]

The first developed was the so-called contact mode where the tip and the sample are in direct mechanical contact. By measuring the change in the vertical deflection of the cantilever as the tip scans the sample surface, topographic images are obtained. Simultaneously to the surface topography, maps of friction or conductivity, which also require direct contact, can be measured. Another kind of operation modes are the so-called dynamic modes where the cantilever is oscillated near its resonance frequency at a given distance from the sample surface. Depending on the amplitude of oscillation, compared to the tip-sample distance, the tip may either not contact the sample (small amplitude) or intermittently contact the sample surface (large amplitude). By measuring changes in amplitude, phase or frequency of the oscillating cantilever in response to the existing tip-sample interactions, one can obtain not only topographic images of the surface but also dissipation, magnetic or electrostatic maps. Though further details are given in next section on those modes employed throughout this work, a complete description of all of them can be found in general SFM book[106].

7.8.4 Scanning probe techniques

Conductive scanning force microscopy

Conductive SFM is used for collecting simultaneous topography imaging and current imaging. Standard conductive SFM operates in contact mode. Variation in surface conductivity can be distinguished by using a conductive tip and applying a DC voltage to the tip (in some microscopes the voltage is applied to the sample). The sample is held at ground potential. The normal forces which act in the vertical bending of the cantilever are in the range of 250-600 nN while current maps are performed. More details can be seen in secc.5.5.

Kelvin probe microscopy

The Kelvin probe technique takes its name from William Thomson, also known as Lord Kelvin, who first introduced it in 1898[91] to explain the formation of built-in contact potential differences (CPD) in metals. To describe this phenomenon, the concept of work function (ϕ) has to be introduced. In its simplest definition, ϕ is the minimal energy needed to remove an electron from the electronic ground state in a given material. It is usually defined as the difference in energy between an electron in the vacuum state and an electron at the Fermi energy of the metal (Fig. 7.18a). In other types of materials, such as semiconductors or insulators, it can be regarded as the difference in energy between the vacuum level and the most loosely bound electrons inside the solid. The Kelvin probe microscopy (KPM)[117] is a method for measuring the surface potential distribution with nanometer resolution. In CPD can be contribute the chemical potential

If we consider a conducting SFM tip and a conducting sample with different work functions (Fig. 7.18a), which are electrically connected, electrons flow from the material with the smaller work function to the material with higher work function. The contact potential difference (CPD) between them, is commonly defined as:

$$V_{CPD} = \frac{\phi_{sample} - \phi_{tip}}{q} = \frac{\Delta\phi}{q} \tag{7.12}$$

where ϕ_{tip} and ϕ_{sample} are the work functions of the tip and the sample, respectively, and q is the elementary charge.

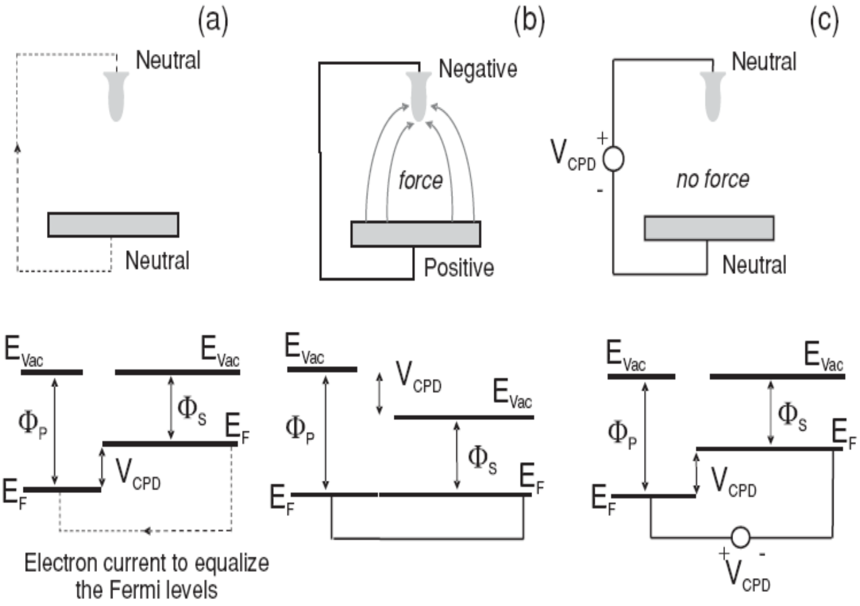

Fig. 7.18: *Definition and basic measurement setup of contact potential difference (CPD). Energy level diagrams of two different metals with work functions ϕ_p and ϕ_s: In case (a) both metals, which are assumed to be plates and form a capacitor, are isolated. If they are connected, as in part (b), the Fermi levels E_F align with the consequence that a potential drop, the so-called contact potential difference (CPD), in the local vacuum level E_{vac} is generated. The vacuum level is flattened by a bias voltage V_{CPD}, as shown in part (c). From Glatzel et al.*[61].

Between the two materials different surface potentials cause electrostatic forces due to the separation-dependent capacitance C between the tip and the sample. Assuming a parallel-plate-capacitor geometry, this force F takes the form of:

$$F = \frac{1}{2}\frac{\partial C}{\partial z}(\Delta\phi)^2 \tag{7.13}$$

where z is the tip-sample distance. To measure the electrostatic force separately from other forces (mainly *van der Waals* and chemical forces), an ac voltage V_{ac} at a frequency ω is superimposed on the tip-sample voltage V_{dc} is applied to the conducting SFM tip (Fig.7.18c). Then, the electrostatic force between the two electrodes (Eq.(7.13)) becomes

$$F = \frac{1}{2}\frac{\partial C}{\partial z}\left\{(\Delta\phi) + [V_{dc} + V_{ac}sin(\omega t)]\right\}^2 \tag{7.14}$$

Developing the equation 7.14 one finds that the force can be separated into three different terms:

$$F = F_{\omega} + F_{\omega}sin(\omega t) + F_{2\omega}sin(2\omega t) \tag{7.15}$$

where,

$$F_{dc} = -\frac{1}{2}\frac{\partial C}{\partial z}\left((V_{dc} - \Delta\phi/q)^2 + \frac{1}{2}V_{ac}^2\right) \tag{7.16}$$

$$F_{\omega} = -\frac{\partial C}{\partial z}(V_{dc} - \Delta\phi/q)V_{ac}sin(\omega t) \tag{7.17}$$

$$F_{2\omega} = \frac{1}{4}\frac{\partial C}{\partial z}V_{ac}^2 cos(2\omega t) \tag{7.18}$$

As a result of the F_{ω} and $F_{2\omega}$, the tip starts vibrating. The tip vibration amplitude can be easily monitored during operation of the SFM. If the V_{dc} applied to the tip is equal in magnitude and opposite in sign to the $\Delta\phi$ of the sample, the spectral components at frequency ω of the tip vibration amplitude, as well as of the force acting on the tip (see Eq.(7.17)) will become zero. The principle of operation of KPM is based on nullifying the tip vibration amplitude at the resonant frequency by applying an adjustable dc voltage. The dc part F_{dc} (Eq.(7.16)) contributes to the topographical signal, the term F_{ω} at the frequency ω (Eq.(7.17)) is used to measure the CPD, and the contribution $F_{2\omega}$ (Eq.(7.18)) can be used for capacitance microscopy.

Mapping of the surface potential was made in the so-called *lift mode*. These measurements were made simultaneously with the topography scan in the tapping mode (Fig.7.19a), using an electrically conducting tip. After each line of topography scan was completed, the feedback loop controlling the vertical piezo was turned off, and the tip was lifted from the surface and traced over the same topography at constant distance (lift scan height), (Fig.7.19b). During this *interleave* scan, a dc bias potential and an oscillating (ac) potential were applied to the tip.

The KPM feedback loop was used to adjust the dc bias on the tip to nullify the force and hence the vibration amplitude of the cantilever at operating frequency (see Eq.(7.17)). Therefore, a quantitative map of $\Delta\phi$ can be obtained by monitoring the voltage V_{dc} applied by the feedback signal. This technique allows very high (the images presented in this thesis have a resolution of $\approx 50mV$) potential

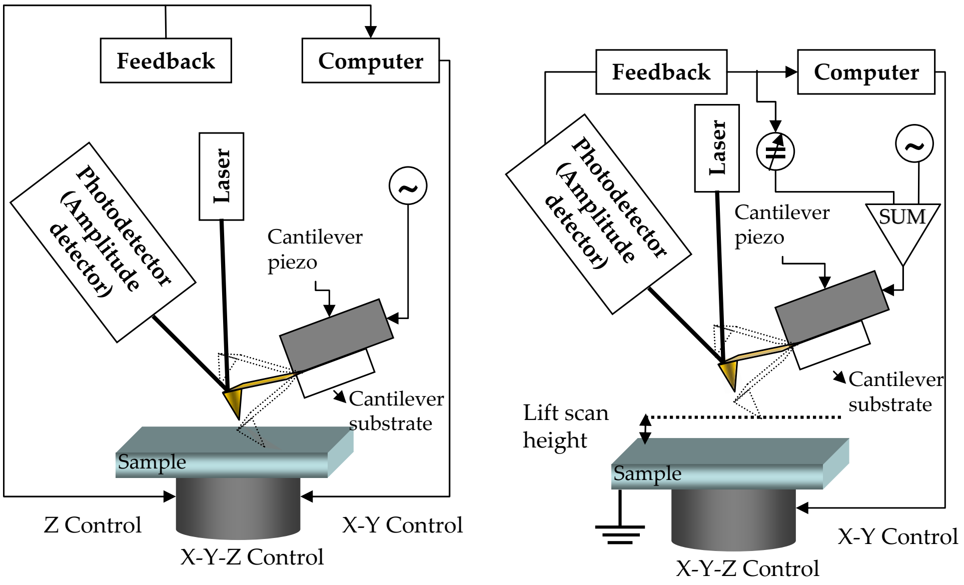

(a)

(b)

Fig. 7.19: *(a) Topography measurements in tapping mode. The cantilever is vibrated by a piezo at the resonant frequency of its free vibrations. Feedback adjusts tip-surface separation to maintain constant amplitude. The feedback output is recorded by the computer and becomes the surface height map. (b) Surface potential measurements during interleave scan in lift mode. The cantilever is scanned across the surface at a constant height. An oscillating voltage is applied to the tip. The KPM feedback adjusts dc bias to nullify vibration amplitude at the operating frequency. The nano-Kelvin probe feedback output is recorded by the computer and by reversing the sign becomes the surface potential map. Adapted from Bhushan and Goldade*[14].

resolution.

Three-dimensional Modes

The so-called *three-dimensional (3D) modes* are an alternative way for recording data[39,114]. Thus, we can obtain a given magnitude ($_1$ $_2$) where $_1$ and $_2$ do not necessarily correspond to longitudinal dimensions. In the resulting image (generally denoted as 3D image) the colour scale represents the magnitude and the horizontal and vertical axis, the two magnitudes chosen as variables ($_1$ and $_2$, respectively), whose influence on is under study. In this way, horizontal profiles provide $_1$ curves at the selected $_2$ value and vertical profiles provide $_2$ curves at selected $_1$ value. Since various images can be simultaneously recorded, the dependence of more than one magnitude on the same two variables can be obtained.

7.9 Outlook

While this thesis presented an experimental methodology to switch between different resistive states in LSMO thin film with promising electrical characteristics, there still remain open questions, especially concerning the ultimate driving force behind this resistive switching phenomenon.

A detailed study of the current-voltage characteristics, in order to determine the possible charge transport mechanisms operating during a complete voltage cycle, is in progress. Preliminary analysis of the different I-V branches indicates that both bulk-limited (i.e. intrinsic) and electrode-limited conduction exist.

To get more insight into the mechanism of resistance switching, it is vital to non-destructively analyze the possible local changes in structure and chemical composition of the tip-induced modifications. Because we have already demonstrated the film is modified in the vertical direction (perpendicular to the film surface), cross-sectional transmission electron microscope (TEM) and electron energy-loss spectroscopy (EELS) or energy-filtered-TEM (EFTEM) measurements might be a powerful tool for such analysis. However, obtaining non-invasive experimental conditions of monitoring the electrical modifications under the electron beam of the microscope needs to be guaranteed. We are at present working on that.

Considering that the studied LSMO manganite presents, in principle, a strong correlation between structural, electronic and magnetic properties we are considered that the analysis of the magnetic properties at the nanoscale of the tip-written marks appear as an essential issue to address. For this purpose, we have employed different approaches, which have not provided conclusive results yet. However, in particular, magnetic force microscopy (MFM) is viewed as a promising technique for such analysis, in which however, for the moment, electrostatic and capacitive interactions forces of electrical modified regions perturb de tip oscillation and should be eliminated. Overcoming the electrostatic interaction problem in modified regions would be possible as well by using X-ray magnetic circular dichroism (XMCD) to study the correlation between electronic and magnetic properties.

Bibliography

[1] ABAD, L.; LAUKHIN, V.; VALENCIA, S.; GAUP, A.; GUDAT, W.; BALCELLS, L. and MARTINEZ, B.: «Interfacial strain: The driving force for selective orbital occupancy in manganite thin films». *Adv. Funct. Mater.*, 2007, **17(18)**, pp. 3918–3925.
http://dx.doi.org/10.1002/adfm.200700137

[2] ABBATE, M.; DE GROOT, F. M. F.; FUGGLE, J. C.; FUJIMORI, A.; STREBEL, O.; LOPEZ, F.; DOMKE, M.; KAINDL, G.; SAWATZKY, G. A.; TAKANO, M.; TAKEDA, Y.; EISAKI, H. and UCHIDA, S.: «Controlled-valence properties of $La_{1-x}Sr_xFeO_3$ and $La_{1-x}Sr_xMnO_3$ studied by soft-x-ray absorption spectroscopy». *Phys. Rev. B*, 1992, **46(8)**, p. 4511.
http://link.aps.org/abstract/PRB/v46/p4511

[3] ADAMO, C.; KE, X.; WANG, H. Q.; XIN, H. L.; HEEG, T.; HAWLEY, M. E.; ZANDER, W.; SCHUBERT, J.; SCHIFFER, P.; MULLER, D. A.; MARITATO, L. and SCHLOM, D. G.: «Effect of biaxial strain on the electrical and magnetic properties of (001) $La_{2/3}Sr_{1/3}MnO_3$ thin films». *Appl. Phys. Lett.*, 2009, **95(11)**, pp. 112504–3.
http://link.aip.org/link/?APL/95/112504/1

[4] ALEXANDER, S.; HELLEMANS, L.; MARTI, O.; SCHNEIR, J.; ELINGS, V.; HANSMA, P. K.; LONGMIRE, MATT and GURLEY, JOHN: «An atomic-resolution atomic-force microscope implemented using an optical lever». *Journal of Applied Physics*, 1989, **65(1)**, pp. 164–167. doi: 10.1063/1.342563.
http://link.aip.org/link/?JAP/65/164/1

[5] ANDERSON, P. W. and HASEGAWA, H.: «Considerations on Double Exchange». *Physical Review*, 1955, **100(2)**, p. 675.
Http://dx.doi.org/10.1103/PhysRev.100.675

[6] ANGELONI, M.; BALESTRINO, G.; BOGGIO, N. G.; MEDAGLIA, P. G.; ORGIANI, P. and TEBANO, A.: «Suppression of the metal-insulator transition temperature in $La_{2/3}Sr_{1/3}MnO_3$ thin films». *J. Appl. Phys.*, 2004, **96(11)**, pp. 6387–6392.
http://link.aip.org/link/?JAP/96/6387/1

[7] ASAMITSU, A.; TOMIOKA, Y.; KUWAHARA, H. and TOKURA, Y.: «Current switching of resistive states in magnetoresistive manganites». *Nature*, 1997, **388(6637)**, pp. 50–52.
http://www.nature.com/nature/journal/v388/n6637/abs/388050a0.html

[8] BAIKALOV, A.; WANG, Y. Q.; SHEN, B.; LORENZ, B.; TSUI, S.; SUN, Y. Y.; XUE, Y. Y. and CHU, C. W.C: «Field-driven hysteretic and reversible resistive switch at the $Ag - Pr_{0.7}Ca_{0.3}MnO_3$ interface». *Appl. Phys. Lett.*, 2003, **83(5)**, pp.

957–959.
http://dx.doi.org/10.1063/1.1590741

[9] Balcells, Ll; Carrillo, A. E.; Martinez, B.; Sandiumenge, F. and Fontcuberta, J.: «Room temperature magnetoresistive sensor based on thick films manganese perovskite». *J. Magn. Magn. Mater.*, 2000, **221(1-2)**, pp. 224–230.
http://dx.doi.org/10.1016/S0304-8853(00)00389-9

[10] Balcells, Ll; Cifre, J.; Calleja, A.; Fontcuberta, J.; Varela, M. and Benitez, F.: «Room-temperature magnetoresistive sensor based on thick films manganese perovskite». *Sensors and Actuators A: Physical*, 2000, **81(1-3)**, pp. 64–66.
Http://dx.doi.org/http://dx.doi.org/10.1016/S0924-4247(99)00118-1

[11] Balevicius, S.; Zurauskiene, N.; Stankevic, V.; Cimmperman, P.; Kersulis, S.; Cesnys, A.; Tolvaisiene, S. and Altgilbers, L. L.: «Fast reversible thermoelectrical switching in manganite thin films». *Appl. Phys. Lett.*, 2007, **90(21)**, p. 212503.
http://dx.doi.org/10.1063/1.2741602

[12] Barth, J. V.; Costantini, G. and Kern, K.: «Engineering atomic and molecular nanostructures at surfaces». *Nature*, 2005, **437(7059)**, pp. 671–679.
http://dx.doi.org/10.1038/nature04166

[13] Bauer, E.: «Photoelectron spectromicroscopy: present and future». *J. Electron Spectrosc. Relat. Phenom.*, 2001, **114-116**, pp. 975–987.
http://dx.doi.org/10.1016/S0368-2048(00)00261-9

[14] Bhushan, Bharat and Goldade, Anton V.: «Kelvin probe microscopy measurements of surface potential change under wear at low loads». *Wear*, 2000, **244(1-2)**, pp. 104–117.
HTTP://DX.DOI.ORG/10.1016/S0043-1648(00)00450-6

[15] Bibes, M.: *Creiximent i estudi de capes primes de manganites de valència mixta.* Ph.D. thesis, ICMAB-CSIC, 2001.

[16] Bibes, M.; Valencia, S.; Balcells, Ll; Martinez, B.; Fontcuberta, J.; Wojcik, M.; Nadolski, S. and Jedryka, E.: «Charge trapping in optimally doped epitaxial manganite thin films». *Phys. Rev. B*, 2002, **66(13)**, p. 134416.
http://link.aps.org/abstract/PRB/v66/e134416

[17] Binnig, G.; Quate, C. F. and Gerber, Ch: «Atomic Force Microscope». *Phys. Rev. Lett.*, 1986, **56(9)**, p. 930.
HTTP://DX.DOI.ORG/10.1103/PhysRevLett.56.930

[18] Binnig, H., G.; Rohrer: «Scanning tunnelling microscopy». *Helv. Phys. Acta*, 1982, **55**, pp. 726–735.

[19] Biskup, N.; de Andres, A.; Ochando, I. M. and Casais, M. T.: «Nonlinear electrical characteristics of the low-bandwidth manganites $R_{1-x}Ca_xMnO_3$ (R=Pr,Nd,Ho,Er; x=0.3-0.5)». *Phys. Rev. B*, 2006, **73(18)**, p. 184404.
http://dx.doi.org/000237950300057

[20] Brous, J.; Fankuchen, I. and Banks, E.: «Rare Earth Titanates with A Perovskite Structure». *Acta Crystallographica*, 1953, **6(1)**, pp. 67–70.

[21] Carneiro, A. S.; Jardim, R. F. and Fonseca, F. C.: «Current localization and Joule self-heating effects in Cr-doped $Nd_{0.5}Ca_{0.5}MnO_3$manganites». *Phys. Rev. B*, 2006, **73(1)**, p. 012410.
http://dx.doi.org/10.1103/PhysRevB.73.012410

[22] Castell, Martin R.: «Wulff shape of microscopic voids in UO_2crystals». *Phys. Rev. B*, 2003, **68(23)**, p. 235411.

[23] Cavallaro, A.; Sandiumenge, F.; Gazquez, J.; Puig, T.; Obradors, X.; Arbiol, J. and Freyhardt, H. C.: «Growth mechanism, microstructure, and surface modification of nanostructured CeO_2 films by chemical solution deposition». *Adv. Funct. Mater.*, 2006, **16(10)**, pp. 1363–1372.
http://dx.doi.org/10.1002/adfm.200500206

[24] Chang, M.; Jo, M.; Kim, S.; Ju, Y.; Jung, S.; Lee, J.; Yoon, J.; Hwang, H. and Lee, C.: «Charge loss behavior of a metal-alumina-nitride-oxide-silicon-type flash memory cell with different levels of charge injection». *Appl. Phys. Lett.*, 2008, **93(23)**, p. 232105.
http://dx.doi.org/10.1063/1.3041642

[25] Chang, S. H.; Lee, J. S.; Chae, S. C.; Lee, S. B.; Liu, C.; Kahng, B.; Kim, D. W. and Noh, T. W.: «Occurrence of Both Unipolar Memory and Threshold Resistance Switching in a NiO Film». *Phys. Rev. Lett.*, 2009, **102(2)**, p. 026801.
http://dx.doi.org/10.1103/PhysRevLett.102.026801

[26] Chen, A.; Haddad, S.; Wu, Y. C.; Lan, Z.; Fang, T. N. and Kaza, S.: «Switching characteristics of Cu_2O metal-insulator-metal resistive memory». *Appl. Phys. Lett.*, 2007, **91(12)**, p. 123517.
http://dx.doi.org/10.1063/1.2789678

[27] Chen, C. T.; Idzerda, Y. U.; Lin, H. J.; Smith, N. V.; Meigs, G.; Chaban, E.; Ho, G. H.; Pellegrin, E. and Sette, F.: «Experimental Confirmation of the X-Ray Magnetic Circular Dichroism Sum Rules for Iron and Cobalt». *Phys. Rev. Lett.*, 1995, **75(1)**, p. 152.
http://link.aps.org/abstract/PRL/v75/p152

[28] Chen, G. J.; Chang, Y. H. and Hsu, H. W.: «The effect of microstructure and secondary phase on magnetic and electrical properties of La-deficient $La_{1-x}MnO_{3-\delta}$ $(0 \leq x \leq 0.3)$ films». *J. Magn. Magn. Mater.*, 2000, **219(3)**, pp. 317–324.

[29] Chen, X.; Wu, N. J.; Strozier, J. and Ignatiev, A.: «Direct resistance profile for an electrical pulse induced resistance change device». *Appl. Phys. Lett.*, 2005, **87(23)**, p. 233506.
http://dx.doi.org/10.1063/1.2139843

[30] Chen, X.; Wu, N. J.; Strozier, J. and Ignatiev, A.: «Spatially extended nature of resistive switching in perovskite oxide thin films». *Appl. Phys. Lett.*, 2006, **89(6)**, p. 063507.
http://dx.doi.org/10.1063/1.2236213

[31] CHEN, Y. F. and ZIESE, M.: «Nonlinear transport properties of $La_{2/3}Ca_{1/3}MnO_3$ and Fe_3O_4 films in the extreme Joule heating regime». *J. Appl. Phys.*, 2007, **101(10)**, p. 103902.
http://dx.doi.org/10.1063/1.2730574

[32] CHEN, Y. F.; ZIESE, M. and ESQUINAZI, P.: «Bistable resistance state induced by Joule self-heating in manganites: A general phenomenon». *Appl. Phys. Lett.*, 2006, **88(22)**, p. 222513.
http://dx.doi.org/10.1063/1.2209204

[33] CHEN, Y. F.; ZIESE, M. and ESQUINAZI, P.: «Joule-heating-enhanced colossal magnetoresistance in $La_{0.8}Ca_{0.2}MnO_3$ films». *Appl. Phys. Lett.*, 2006, **89(8)**, p. 082501.
http://dx.doi.org/10.1063/1.2337280

[34] CHOI, B. J.; JEONG, D. S.; KIM, S. K.; ROHDE, C.; CHOI, S.; OH, J. H.; KIM, H. J.; HWANG, C. S.; SZOT, K.; WASER, R.; REICHENBERG, B. and TIEDKE, S.: «Resistive switching mechanism of TiO_2 thin films grown by atomic-layer deposition». *J. Appl. Phys.*, 2005, **98(3)**, p. 033715.
http://dx.doi.org/10.1063/1.2001146

[35] CHUA, L. O.: «Memristor - Missing Circuit Element». *IEEE T. Circuits. Syst.*, 1971, **Ct18(5)**, pp. 507–519.

[36] CHUDNOVSKII, F. A.; ODYNETS, L. L.; PERGAMENT, A. L. and STEFANOVICH, G. B.: «Electroforming and switching in oxides of transition metals: The role of metal-insulator transition in the switching mechanism». *J. Solid State Chem.*, 1996, **122(1)**, pp. 95–99.
http://dx.doi.org/10.1006/jssc.1996.0087

[37] COEY, J. M. D.; VIRET, M. and VON MOLNAR, S.: «Mixed-valence manganites». *Advances in Physics*, 1999, **48(2)**, pp. 167–293.

[38] COHN, J. L.; NEUMEIER, J. J.; POPOVICIU, C. P.; MCCLELLAN, K. J. and LEVENTOURI, T.: «Local lattice distortions and thermal transport in perovskite manganites». *Phys. Rev. B*, 1997, **56(14)**, pp. R8495–R8498.

[39] COLCHERO, J.; STORCH, A.; LUNA, M.; GOMEZ-HERRERO, J. and BARO, A. M.: «Observation of liquid neck formation with scanning force microscopy techniques». *Langmuir*, 1998, **14(9)**, pp. 2230–2234.

[40] COLL, M.; GAZQUEZ, J.; POMAR, A.; PUIG, T.; SANDIUMENGE, F. and OBRADORS, X.: «Stress-induced spontaneous dewetting of heteroepitaxial $YBa_2Cu_3O_7$ thin films». *Phys. Rev. B*, 2006, **73(7)**, pp. 075420–8.
http://dx.doi.org/10.1103/PhysRevB.73.075420

[41] CULLITY B.D, INTRODUCTION TO MAGNETIC MATERIALS: *Introduction to magnetic materials*. Addison and Wesley, 1972.

[42] DAGOTTO, ELBIO; HOTTA, TAKASHI and MOREO, ADRIANA: «Colossal magnetoresistant materials: the key role of phase separation». *Phys. Rep.*, 2001, **344(1-3)**, pp. 1–153.

[43] DE GENNES, P. G.: «Effects of Double Exchange in Magnetic Crystals». *Physical Review*, 1960, **118(1)**, p. 141.
Http://dx.doi.org/10.1103/PhysRev.118.141

[44] DE JONG, M. P.; BERGENTI, I.; OSIKOWICZ, W.; FRIEDLEIN, R.; DEDIU, V. A.; TALIANI, C. and SALANECK, W. R.: «Valence electronic states related to Mn^{2+} at $La_{0.7}Sr_{0.3}MnO_3$ surfaces characterized by resonant photoemission». *Phys. Rev. B*, 2006, **73(5)**, p. 052403.
http://dx.doi.org/10.1103/PhysRevB.73.052403

[45] DE LIGNY, DOMINIQUE and RICHET, PASCAL: «High-temperature heat capacity and thermal expansion of SrTiO3 and SrZrO3 perovskites». *Phys. Rev. B*, 1996, **53(6)**, p. 3013.
http://link.aps.org/abstract/PRB/v53/p3013

[46] DHO, J.; HUR, N. H.; KIM, I. S. and PARK, Y. K.: «Oxygen pressure and thickness dependent lattice strain in $La_{0.7}Sr_{0.3}MnO_3$ films». *J. Appl. Phys.*, 2003, **94(12)**, pp. 7670–7674.
http://link.aip.org/link/?JAP/94/7670/1

[47] DORR, K.: «Ferromagnetic manganites: spin-polarized conduction versus competing interactions». *J. Phys. D*, 2006, **39(7)**, pp. R125–R150.
ISI:000237216900008

[48] EKIN, J. W.; CLICKNER, C. C.; RUSSEK, S. E. and SANDERS, S. C.: «Oxygen Annealing of Ex-Situ YBCO/Ag Thin-Film Interfaces». *IEEE T. Appl. Supercon.*, 1995, **5(2)**, pp. 2400–2403.

[49] FOEX, M.: «Proprietes de Quelques Solutions Solides et Composes A Base Doxyde de Lanthane». *Bull. Soc. Chim. Fr.*, 1961, **(1)**, pp. 109–&.

[50] FOLTYN, S. R.; CIVALE, L.; MANUS-DRISCOLL, J. L.; JIA, Q. X.; MAIOROV, B.; WANG, H. and MALEY, M.: «Materials science challenges for high-temperature superconducting wire». *Nat. Mater.*, 2007, **6(9)**, pp. 631–642.

[51] FONTCUBERTA, J.; MARTINEZ, B.; SEFFAR, A.; PIÑOL, S.; GARCIA-MUÑOZ, J. L. and OBRADORS, X.: «Colossal Magnetoresistance of Ferromagnetic Manganites: Structural Tuning and Mechanisms». *Phys. Rev. Lett.*, 1996, **76(7)**, p. 1122.
http://link.aps.org/abstract/PRL/v76/p1122

[52] FOR DIFFRACTION DATA, INTERNATIONAL CENTRE: «No. 000221430», 2008.

[53] FOR DIFFRACTION DATA, INTERNATIONAL CENTRE: «No. 000221431», 2008.

[54] FOR DIFFRACTION DATA, INTERNATIONAL CENTRE: «No. 000420343», 2008.

[55] FU, C. C.; HUANG, Z. and YEH, N. C.: «Spin-polarized quasiparticle transport in cuprate superconductors». *Phys. Rev. B*, 2002, **65(22)**, p. 224516.
http://link.aps.org/doi/10.1103/PhysRevB.65.224516

[56] GAJEK, MARTIN; BIBES, MANUEL; FUSIL, STEPHANE; BOUZEHOUANE, KARIM; FONTCUBERTA, JOSEP; BARTHELEMY, AGNES and FERT, ALBERT: «Tunnel junctions with multiferroic barriers». *Nat. Mater.*, 2007, **6(4)**, pp. 296–302.
http://dx.doi.org/10.1038/nmat1860

[57] Garcia, V.; Fusil, S.; Bouzehouane, K.; Enouz-Vedrenne, S.; Mathur, N. D.; Barthelemy, A. and Bibes, M.: «Giant tunnel electroresistance for non-destructive readout of ferroelectric states». *Nature*, 2009, **460(7251)**, pp. 81–84.
`http://dx.doi.org/10.1038/nature08128`

[58] Gibert, M.; Puig, T. and Obradors, X.: «Growth of strain-induced self-assembled $BaZrO_3$ nanodots from chemical solutions». *Surf. Sci.*, 2007, **601(13)**, pp. 2680–2683.

[59] Gibert, M.; Puig, T.; Obradors, X.; Benedetti, A.; Sandiumenge, F. and Hohne, R.: «Self-Organization of Heteroepitaxial CeO_2 Nanodots Grown from Chemical Solutions». *Adv. Mater.*, 2007, **19(22)**, pp. 3937–3942.
`http://dx.doi.org/10.1002/adma.200700361`

[60] Gil, A; Colchero, J; Gomez-Herrero, J and Baro, A M: «Electrostatic force gradient signal: resolution enhancement in electrostatic force microscopy and improved Kelvin probe microscopy». *Nanotechnology*, 2003, **14(2)**, pp. 332–340.
`http://stacks.iop.org/0957-4484/14/332`

[61] Glatzel, Th; Lux-Steiner, M. Ch; Strassburg, E.; Boag, A. and Rosenwaks, Y.: «Principles of Kelvin Probe Force Microscopy». In: *Scanning Probe Microscopy*, pp. 113–131, 2007.
`http://dx.doi.org/10.1007/978-0-387-28668-6_5`

[62] Gorbenko, O. Y.: «HREM and XRD characterization of epitaxial perovskite manganites». *J. Magn. Magn. Mater.*, 2000, **211(1)**, pp. 97–104.

[63] Gurevich, A. V. and Mints, R. G.: «Self-Heating in Normal Metals and Superconductors». *Reviews of Modern Physics*, 1987, **59(4)**, pp. 941–999.

[64] Gutierrez, J.: *Vortex pinning and critical currents in $YBa_2Cu_3O_{7-x}$ MOD-TFA thin films and Coated Conductors*. Ph.D. thesis, ICMAB-CSIC, Universitat Autònoma de Barcelona, 2008.

[65] Gutierrez, J.; Llordes, A.; Gazquez, J.; Gibert, M.; Roma, N.; Ricart, S.; Pomar, A.; Sandiumenge, F.; Mestres, N.; Puig, T. and Obradors, X.: «Strong isotropic flux pinning in solution-derived $YBa_2Cu_3O_{7-x}$ nanocomposite superconductor films». *Nat. Mater.*, 2007, **6(5)**, pp. 367–373.
`http://dx.doi.org/10.1038/nmat1893`

[66] Habermeier, Hanns-Ulrich: «Thin films of perovskite-type complex oxides». *Materials Today*, 2007, **10(10)**, pp. 34–43.
`http://dx.doi.org/10.1016/S1369-7021(07)70243-2`

[67] Haghiri-Gosnet, A. M. and Renard, J. P.: «CMR manganites: physics, thin films and devices». *J.Phys. D*, 2003, **36(8)**, pp. R127–R150.
`http://stacks.iop.org/jd/36/R127`

[68] Haghiri-Gosnet, A. M.; Wolfman, J.; Mercey, B.; Simon, C.; Lecoeur, P.; Korzenski, M.; Hervieu, M.; Desfeux, R. and Baldinozzi, G.: «Microstructure and magnetic properties of strained $La_{0.7}Sr_{0.3}MnO_3$ thin films». *J. Appl. Phys.*, 2000, **88(7)**, pp. 4257–4264.

[69] HAMANN, H. F.; O'BOYLE, M.; MARTIN, Y. C.; ROOKS, M. and WICKRAMASINGHE, K.: «Ultra-high-density phase-change storage and memory». *Nat. Mater.*, 2006, **5(5)**, pp. 383–387.
http://dx.doi.org/10.1038/nmat1627

[70] HAMMOUCHE, A.; SCHOULER, E. J. L. and HENAULT, M.: «Electrical and Thermal-Properties of Sr-Doped Lanthanum Manganites». *Solid State Ionics*, 1988, **28**, pp. 1205–1207.

[71] HAMMOUCHE, A.; SIEBERT, E. and HAMMOU, A.: «Crystallographic, Thermal and Electrochemical Properties of the System $La_{1-x}Sr_xMnO_3$ for High-Temperature Solid Electrolyte Fuel-Cells». *Mater. Res. Bull.*, 1989, **24(3)**, pp. 367–380.

[72] HASENKOX, U.; MITZE, C. and WASER, R.: «Metal propionate synthesis of magnetoresistive $La_{1-x}(Ca, Sr)_{(x)}MnO - 3$ thin films». *J. Am. Ceram. Soc.*, 1997, **80(10)**, pp. 2709–2713.

[73] HASENKOX, U.; MITZE, C.; WASER, R.; ARONS, R. R.; POMMER, J. and GUNTHERODT, G.: «Chemical solution deposition of epitaxial $La_{1-x}(Ca, Sr)_{(x)}MnO_3$ thin films». *Journal of Electroceramics*, 1999, **3(3)**, pp. 255–260.

[74] HASSINI, A.; POMAR, A.; GUTIERREZ, J.; COLL, M.; ROMA, N.; MORENO, C.; RUYTER, A.; PUIG, T. and OBRADORS, X.: «Atomically flat MOD $La_{0.7}Sr_{0.3}MnO_3$ buffer layers for high critical current $YBa_2Cu_3O_7$ TFA films». *Supercond. Sci. Technol.*, 2007, **20(9)**, pp. S230–S238.
http://dx.doi.org/000249596200019

[75] HE, J. Q.; JIA, C. L.; SCHUBERT, J. and WANG, R. H.: «Microstructures of epitaxial $La_{0.7}Ca_{0.3}MnO_3$ thin films grown on $SrTiO_3$ and $NdGaO_3$ substrates». *J. Cryst. Growth*, 2004, **265(1-2)**, pp. 241–249.

[76] HICKMOTT, T. W.: «Low-Frequency Negative Resistance in Thin Anodic Oxide Films». *J. Appl. Phys.*, 1962, **33(9)**, pp. 2669–2682.

[77] HORCAS, I.; FERNANDEZ, R.; GOMEZ-RODRIGUEZ, J. M.; COLCHERO, J.; GOMEZ-HERRERO, J. and BARO, A. M.: «WSXM: A software for scanning probe microscopy and a tool for nanotechnology». *Rev. Sci. Instrum.*, 2007, **78(1)**, p. 013705.
http://dx.doi.org/10.1063/1.2432410

[78] HWANG, H. Y.; CHEONG, S. W.; ONG, N. P. and BATLOGG, B.: «Spin-Polarized Intergrain Tunneling in $La_{2/3}Sr_{1/3}MnO_3$». *Phys. Rev. Lett.*, 1996, **77(10)**, p. 2041.
http://link.aps.org/abstract/PRL/v77/p2041

[79] HWANG, H. Y.; CHEONG, S. W.; RADAELLI, P. G.; MAREZIO, M. and BATLOGG, B.: «Lattice Effects on the Magnetoresistance in Doped LaMnO3». *Phys. Rev. Lett.*, 1995, **75(5)**, p. 914.
http://link.aps.org/abstract/PRL/v75/p914

[80] IMAMORI, S.; TOKUNAGA, M.; HAKUTA, S. and TAMEGAI, T.: «Room temperature low-field colossal magnetoresistance in $La_{0.7}Sr_{0.3}MnO_3$». *Appl. Phys. Lett.*, 2006, **89(17)**, p. 172508.
http://dx.doi.org/10.1063/1.2364165

[81] Infante, I. C.; Sanchez, F.; Fontcuberta, J.; Wojcik, M.; Jedryka, E.; Estrade, S.; Peiro, F.; Arbiol, J.; Laukhin, V. and Espinos, J. P.: «Elastic and orbital effects on thickness-dependent properties of manganite thin films». *Phys. Rev. B*, 2007, **76(22)**, p. 224415.
http://dx.doi.org/10.1103/PhysRevB.76.224415

[82] Inoue, I. H. and Rozenberg, M. J.: «Taming the Mott transition for a novel Mott transistor». *Adv. Funct. Mater.*, 2008, **18(16)**, pp. 2289–2292.
http://dx.doi.org/10.1002/adfm.200800558

[83] Israelachvili, J.: *Intermolecular and surface forces*. Academic Press, 1992.

[84] Janousch, M.; Meijer, G. I.; Staub, U.; Delley, B.; Karg, S. F. and Andreasson, B. P.: «Role of oxygen vacancies in Cr-doped $SrTiO_3$ for resistance-change memory». *Adv. Mater.*, 2007, **19(17)**, pp. 2232–2235.
http://dx.doi.org/10.1002/adma.200602915

[85] Jeong, D. S.; Schroeder, H.; Breuer, U. and Waser, R.: «Characteristic electroforming behavior in $Pt/TiO_2/Pt$ resistive switching cells depending on atmosphere». *J. Appl. Phys.*, 2008, **104(12)**, p. 123716.
http://dx.doi.org/10.1063/1.3043879

[86] Jin, S.; Tiefel, T. H.; McCormack, M.; Fastnacht, R. A.; Ramesh, R. and Chen, L. H.: «Thousandfold Change in Resistivity in Magnetoresistive La-Ca-Mn-O Films». *Science*, 1994, **264(5157)**, pp. 413–415.
http://www.sciencemag.org/cgi/content/abstract/264/5157/413

[87] Jone, Z.: *Autoensamblaje dirigido de nanoestructuras de $Ce_{0.9}Gd_{0.1}O_{2?y}$ crecidas por via quimica sobre sustratos nanoindentados*. Master's thesis, ICMAB-CSIC, 2008.

[88] Jones, H.: *Introduction to section B5: Superconductors contacts in "A Handbook of Superconducting Materials"*. volume Vol. I: Superconductivity, Materials and Processes. IOP Publishing Ltd., 2003.

[89] Jonker, G. H. and Vansanten, J. H.: «Ferromagnetic Compounds of Manganese with Perovskite Structure». *Physica*, 1950, **16(3)**, pp. 337–349.
Http://dx.doi.org/10.1016/0031-8914(50)90033-4

[90] Kang, B. S.; Wang, H.; Manus-Driscoll, J. L.; Li, Y.; Jia, Q. X.; Mihut, I. and Betts, J. B.: «Low field magnetotransport properties of $(La_{0.7}Sr_{0.3}MnO_3)_{(0.5)} : (ZnO)_{(0.5)}$ nanocomposite films». *Appl. Phys. Lett.*, 2006, **88(19)**.
http://link.aip.org/link/?APL/88/192514/1

[91] Kelvin, L.: *Philos. Mag.*, 1898, **46**, p. 82.

[92] Khartsev, S. I.; Johnsson, P. and Grishin, A. M.: «Colossal magnetoresistance in ultrathin epitaxial $La_{0.75}Sr_{0.25}MnO_3$ films». *J. Appl. Phys.*, 2000, **87(5)**, pp. 2394–2399.
http://link.aip.org/link/?JAP/87/2394/1

[93] Laan, G. van der and Kirkman, I. W.: «The 2p absorption spectra of 3d transition metal compounds in tetrahedral and octahedral symmetry». *J. Phys.: Condens. Matter*, 1992, **4(16)**, pp. 4189–4204.

[94] LAI, S. K.: «Flash memories: Successes and challenges». *Ibm Journal of Research and Development*, 2008, **52(4-5)**, pp. 529–535.

[95] LANGJAHR, P. A.; WAGNER, T.; RUHLE, M. and LANGE, F. F.: «Thermally induced structural changes in epitaxial $SrZrO_3$ films on $SrTiO_3$». *Journal of Materials Research*, 1999, **14(7)**, pp. 2945–2951.
http://link.aip.org/link/?JMR/14/2945/1

[96] LAU, H. K. and LEUNG, C. W.: «Nonvolatile multilevel memory effect by resistive switching in manganite thin films». *J. Appl. Phys.*, 2008, **104(12)**, p. 123705.
http://dx.doi.org/10.1063/1.3043801

[97] LIU, S. Q.; WU, N. J. and IGNATIEV, A.: «Electric-pulse-induced reversible resistance change effect in magnetoresistive films». *Appl. Phys. Lett.*, 2000, **76(19)**, pp. 2749–2751.

[98] LOOS, J.: «The Art of SPM: Scanning Probe Microscopy in Materials Science». *Adv. Mater.*, 2005, **17(15)**, pp. 1821–1833.

[99] LU, C. J.: «Microstructure of epitaxial $La_{0.7}Ca_{0.3}MnO_3$ thin films grown on $LaAlO_3$ and $SrTiO_3$». *J. Appl. Phys.*, 2000, **88(7)**, p. 4032.

[100] LU, YAFENG; KLEIN, J.; HERBSTRITT, F.; PHILIPP, J. B.; MARX, A. and GROSS, R.: «Effect of strain and tetragonal lattice distortions in doped perovskite manganites». *Phys. Rev. B*, 2006, **73(18)**, pp. 184406–7.
http://link.aps.org/abstract/PRB/v73/e184406

[101] MAIGNAN, A.; SIMON, CH; CAIGNAERT, V. and RAVEAU, B.: «Size of the interpolated cation and hole: carrier density two key parameters for the optimisation of colossal magnetoresistive properties of Pr-based manganites». *Z. Phys. B*, 1996, **99(3)**, pp. 305–310.
http://dx.doi.org/10.1007/s002570050041

[102] MAURICE, J. L.; PAILLOUX, F.; BARTHELEMY, A.; DURAND, O.; IMHOFF, D.; LYONNET, R.; ROCHER, A. and CONTOUR, J. P.: «Strain relaxation in the epitaxy of $La_{2/3}Sr_{1/3}MnO_3$ grown by pulsed-laser deposition on $SrTiO_3$(001)». *Philos. Mag.*, 2003, **83(28)**, pp. 3201–3224.
http://dx.doi.org/10.1080/14786430310001603436

[103] MAURICE, J. L.; PAILLOUX, F.; BARTHELEMY, A.; ROCHER, A.; DURAND, O.; LYONNET, R. and CONTOUR, J. P.: «Strain and magnetism in $(La_{0.7}Sr_{0.3})MnO_3$ very thin films epitaxially grown on $SrTiO_3$». *Appl. Surf. Sci.*, 2002, **188(1-2)**, pp. 176–181.

[104] MEIJER, G. I.: «Materials science - Who wins the nonvolatile memory race?» *Science*, 2008, **319(5870)**, pp. 1625–1626.
http://dx.doi.org/10.1126/science.1153909

[105] MERCONE, S.; FRESARD, R.; CAIGNAERT, V.; MARTIN, C.; SAUREL, D.; SIMON, C.; ANDRE, G.; MONOD, P. and FAUTH, F.: «Nonlinear effects and Joule heating in I-V curves in manganites». *J. Appl. Phys.*, 2005, **98(2)**, p. 023911.
http://dx.doi.org/10.1063/1.1993750

[106] MEYER, E.; HUG, H. J. and BENNEWITZ, R.: *Scanning Probe Microscopy. The lab on a tip*. Springe-Verlag, 2004.

[107] Meyer, Gerhard and Amer, Nabil M.: «Optical-beam-deflection atomic force microscopy: The NaCl (001) surface». *Applied Physics Letters*, 1990, **56(21)**, pp. 2100–2101. doi: 10.1063/1.102985.
http://link.aip.org/link/?APL/56/2100/1

[108] Meyer, Gerhard and Amer, Nabil M.: «Simultaneous measurement of lateral and normal forces with an optical-beam-deflection atomic force microscope». *Applied Physics Letters*, 1990, **57(20)**, pp. 2089–2091. doi: 10.1063/1.103950.
http://link.aip.org/link/?APL/57/2089/1

[109] Millis, A. J.; Darling, T. and Migliori, A.: «Quantifying strain dependence in "colossal" magnetoresistance manganites». *J. Appl. Phys.*, 1998, **83(3)**, pp. 1588–1591.
http://link.aip.org/link/?JAPIAU/83/1588/1

[110] Moreo, Adriana; Yunoki, Seiji and Dagotto, Elbio: «Phase Separation Scenario for Manganese Oxides and Related Materials». *Science*, 1999, **283(5410)**, pp. 2034–2040.
http://www.sciencemag.org/cgi/content/abstract/283/5410/2034

[111] Morita, S.; Wiesendanger, v and Meyer, E.: *Noncontact Atomic Force Microscopy*. NanoScience and Technology, Springe-Verlag, 2002.

[112] Moshnyaga, V.; Damaschke, B.; Shapoval, O.; Belenchuk, A.; Faupel, J.; Lebedev, O. I.; Verbeeck, J.; van Tendeloo, G.; Mucksch, M.; Tsurkan, V.; Tidecks, R. and Samwer, K.: «Structural phase transition at the percolation threshold in epitaxial $(La_{0.7}Ca_{0.3}MnO_3)_{(1-X)}:(MgO)_{(X)}$ nanocomposite films». *Nat. Mater.*, 2003, **2(4)**, pp. 247–252.
http://dx.doi.org/10.1038/nmat859

[113] Nagaev, E. L.: «Colossal-magnetoresistance materials: manganites and conventional ferromagnetic semiconductors». *Phys. Rep.*, 2001, **346(6)**, pp. 388–531.

[114] nanotec:. «Nanotec Electronica. www.Nanotec.es». NOT IN FILE.

[115] Nian, Y. B.; Strozier, J.; Wu, N. J.; Chen, X. and Ignatiev, A.: «Evidence for an oxygen diffusion model for the electric pulse induced resistance change effect in transition-metal oxides». *Phys. Rev. Lett.*, 2007, **98(14)**, p. 146403.

[116] Nie J.C, Yamasaki H. Mawatari Y.: «Self-assembled growth of CeO_2 nanostructures on sapphire». *Phys. Rev. B*, 2007, **70**, p. 195421.

[117] Nonnenmacher, M.; O'Boyle, M. P. and Wickramasinghe, H. K.: «Kelvin probe force microscopy». *Appl. Phys. Lett.*, 1991, **58(25)**, pp. 2921–2923.

[118] Norton, David P.: «Synthesis and properties of epitaxial electronic oxide thin-film materials». *Materials Science and Engineering: R: Reports*, 2004, **43(5-6)**, pp. 139–247.
http://dx.doi.org/10.1016/j.mser.2003.12.002

[119] Odagawa, A.; Kanno, T. and Adachi, H.: «Transient response during resistance switching in $Ag/Pr_{0.7}Ca_{0.3}MnO_3/Pt$ thin films». *J. Appl. Phys.*, 2006, **99(1)**, p. 016101.

[120] OVSHINSK.SR: «Reversible Electrical Switching Phenomena in Disordered Structures». *Phys. Rev. Lett.*, 1968, **21(20)**, pp. 1450–1453.

[121] PALANISAMI, A.; WEISSMAN, M. B. and MATHUR, N. D.: «Nonlinear effects of current on transport in manganite films». *Phys. Rev. B*, 2005, **71(9)**, p. 094419.

[122] PARK, J. H.; VESCOVO, E.; KIM, H. J.; KWON, C.; RAMESH, R. and VENKATESAN, T.: «Direct evidence for a half-metallic ferromagnet». *Nature*, 1998, **392(6678)**, pp. 794–796.

[123] PERSHIN, Y. and DI VENTRA, M.: «Experimental demonstration of associative memory with memristive neural networks». *Nature Precedings*, 2009, p. hdl:10101/npre.2009.3258.1.
http://precedings.nature.com/documents/3258/version/1

[124] PHILLIPS, J. M.: «Substrate selection for high-temperature superconducting thin films». *Journal of Applied Physics*, 1996, **79(4)**, pp. 1829–1848.
http://link.aip.org/link/?JAPIAU/79/1829/1

[125] POMAR, A.; COLL, M.; CAVALLARO, A.; GAZQUEZ, J.; GONZALEZ, J. C.; MESTRES, N.; SANDIUMENGE, F.; PUIG, T. and OBRADORS, X.: «All-chemical high-J(c) $YBa_2Cu_3O_7$ multilayers with $SrTiO_3$ as cap layer». *J. Mater. Res.*, 2006, **21(5)**, pp. 1106–1116.

[126] PRAUS, R. B.; LEIBOLD, B.; GROSS, G. M. and HABERMEIER, H. U.: «Thickness dependent properties of $La_{0.67}Ca_{0.33}MnO_3$ thin films». *Appl. Surf. Sci.*, 1999, **139**, pp. 40–43.
http://dx.doi.org/10.1016/S0169-4332(98)00384-5

[127] PRELLIER, W.; LECOUER, PH. and MERCEY, B.: «Colossal-magnetoresistive manganite thin films». *J. Phys.: Condens. Matter*, 2001, **13**, pp. R915–R944.

[128] QUINTERO, M.; LEVY, P.; LEYVA, A. G. and ROZENBERG, M. J.: «Mechanism of electric-pulse-induced resistance switching in manganites». *Phys. Rev. Lett.*, 2007, **98(11)**, p. 116601.

[129] RAMIREZ, A. P.: «Colossal magnetoresistance». *J. Phys.: Condens. Matter*, 1997, **9(39)**, pp. 8171–8199.
Http://dx.doi.org/http://dx.doi.org/10.1088/0953-8984/9/39/005

[130] RANNO, L.; LLOBET, A.; TIRON, R. and FAVRE-NICOLIN, E.: «Strain-induced magnetic anisotropy in epitaxial manganite films». *Appl. Surf. Sci.*, 2002, **188(1-2)**, pp. 170–175.
http://dx.doi.org/10.1016/S0169-4332(01)00730-9

[131] RAO, R. A.; LAVRIC, D.; NATH, T. K.; EOM, C. B.; WU, L. and TSUI, F.: «Three-dimensional strain states and crystallographic domain structures of epitaxial colossal magnetoresistive $La_{0.8}Ca_{0.2}MnO_3$ thin films». *Appl. Phys. Lett.*, 1998, **73(22)**, pp. 3294–3296.

[132] REAGOR, D. W.; LEE, S. Y.; LI, Y. and JIA, Q. X.: «Work function of the mixed-valent manganese perovskites». *J. Appl. Phys.*, 2004, **95(12)**, pp. 7971–7975.

[133] ROSS, C. A.: «PATTERNED MAGNETIC RECORDING MEDIA». *Annu. Rev. Mater. Res.*, 2001, **31(1)**, pp. 203–235.

[134] ROSSEL, C.; MEIJER, G. I.; BREMAUD, D. and WIDMER, D.: «Electrical current distribution across a metal-insulator-metal structure during bistable switching». *J. Appl. Phys.*, 2001, **90(6)**, pp. 2892–2898.

[135] ROZENBERG, M. J.; INOUE, I. H. and SANCHEZ, M. J.: «Nonvolatile memory with multilevel switching: A basic model». *Phys. Rev. Lett.*, 2004, **92(17)**, p. 178302.

[136] RUDDLESDEN, S. N. and POPPER, P.: «The Compound $Sr_3Ti_2O_7$ and Its Structure». *Acta Crystallographica*, 1958, **11(1)**, pp. 54–55.
http://dx.doi.org/10.1107/S0365110X58000128

[137] SACANELL, J.; LEYVA, A. G. and LEVY, P.: «Electrical current effect in phase-separated $La_{5/8-y}Pr_yCa_{3/8}MnO_3$: Charge order melting versus Joule heating». *J. Appl. Phys.*, 2005, **98(11)**, p. 113708.

[138] SALAMON, M. B. and JAIME, M.: «The physics of manganites: Structure and transport». *Rev. Mod. Phys.*, 2001, **73(3)**, pp. 583–628.

[139] SARID, D.: *Scanning Force Microscopy*. Oxford University Press, New York, 1994.

[140] SAWA, A.: «Resistive switching in transition metal oxides». *Materials Today*, 2008, **11(6)**, pp. 28–36.

[141] SAWA, A.; FUJII, T.; KAWASAKI, M. and TOKURA, Y.: «Interface resistance switching at a few nanometer thick perovskite manganite active layers». *Appl. Phys. Lett.*, 2006, **88(23)**, p. 232112.

[142] SAWA, A.; YAMAMOTO, A.; YAMADA, H.; FUJII, T.; KAWASAKI, M.; MATSUNO, J. and TOKURA, Y.: «Fermi level shift in $La_{1-x}Sr_xMO_3$ (M=Mn, Fe, Co, and Ni) probed by Schottky-like heteroepitaxial junctions with $SrTi_{0.99}Nb_{0.01O3}$». *Appl. Phys. Lett.*, 2007, **90(25)**, p. 252102.

[143] SCHULZE, A. R. and MULLERBUSCHBAUM, H.: «Preparation and Investigation of the Metastable Compound Sr3La4O9». *Zeitschrift fur Anorganische und Allgemeine Chemie*, 1980, **471(12)**, pp. 59–63.
ISI:A1980KW71800005

[144] SCHWARTZ, R. W.; SCHNELLER, T. and WASER, R.: «Chemical solution deposition of electronic oxide films». *C. R. Chim.*, 2004, **7(5)**, pp. 433–461.
http://dx.doi.org/10.1016/j.crci.2004.01.007

[145] SEIFERT, A.; VOJTA, A.; SPECK, J. S. and LANGE, F. F.: «Microstructural instability in single-crystal thin films». *J. Mater. Res.*, 1996, **11**, p. 1470.

[146] SERGEI, V. KALININ; RUI, SHAO and DAWN, A. BONNELL: «Local Phenomena in Oxides by Advanced Scanning Probe Microscopy». *J. Am. Ceram. Soc.*, 2005, **88(5)**, pp. 1077–1098.
http://dx.doi.org/10.1111/j.1551-2916.2005.00383.x

[147] SESHADRI, R.; HERVIEU, M.; MARTIN, C.; MAIGNAN, A.; DOMENGES, B.; RAVEAU, B. and FITCH, A. N.: «Study of the layered magnetoresistive perovskite $La_{1.2}Sr_{1.8}Mn_2O_7$ by high-resolution electron microscopy and synchrotron X-ray powder diffraction». *Chem. Mater.*, 1997, **9(8)**, pp. 1778–1787.

[148] Seshadri, R.; Martin, C.; Hervieu, M.; Raveau, B. and Rao, C. N. R.: «Structural evolution and electronic properties of $La_{1+x}Sr_{2-x}Mn_2O_7$». *Chem. Mater.*, 1997, **9(1)**, pp. 270–277.

[149] Shchukin, V. A. and Bimberg, D.: «Spontaneous ordering of nanostructures on crystal surfaces». *Reviews of Modern Physics*, 1999, **71(4)**, pp. 1125–1171.

[150] Snyder, G. Jeffrey; Hiskes, Ron; DiCarolis, Steve; Beasley, M. R. and Geballe, T. H.: «Intrinsic electrical transport and magnetic properties of $La_{0.67}Ca_{0.33}MnO_3$ and $La_{0.67}Sr_{0.33}MnO_3$ MOCVD thin films and bulk material». *Phys. Rev. B*, 1996, **53(21)**, p. 14434.

[151] Song, H.; Tokunaga, M.; Imamori, S.; Tokunaga, Y. and Tamegai, T.: «Nonvolatile multivalued memory effects in electronic phase-change manganites controlled by Joule heating». *Phys. Rev. B*, 2006, **74(5)**, p. 052404.

[152] Steenbeck, K.; Habisreuther, T.; Dubourdieu, C. and Senateur, J. P.: «Magnetic anisotropy of ferromagnetic $La_{0.7}Sr_{0.3}MnO_3$ epitaxial thin films: Dependence on temperature and film thickness». *Appl. Phys. Lett.*, 2002, **80(18)**, pp. 3361–3363.
http://dx.doi.org/10.1063/1.1473870

[153] Steigmeier, E. F: «Field Effect on Cochran Modes in $SrTiO_3$ and $KTaO_3$». *Physical Review*, 1968, **168(2)**, pp. 523–530.

[154] Strukov, D. B.; Snider, G. S.; Stewart, D. R. and Williams, R. S.: «The missing memristor found». *Nature*, 2008, **453(7191)**, pp. 80–83.

[155] Strukov, D. B. and Williams, R. S.: «Exponential ionic drift: fast switching and low volatility of thin-film memristors». *Applied Physics a-Materials Science & Processing*, 2009, **94(3)**, pp. 515–519.

[156] Szewczyk, A.; Gutowska, M. and Dabrowski, B.: «Specific heat and phase diagram of heavily doped $La_{1-x}Sr_xMnO_3(0.45 \leq x \leq 1.0)$». *Phys. Rev. B*, 2005, **72(22)**, p. 224429.
http://link.aps.org/abstract/PRB/v72/e224429

[157] Szot, K.; Speier, W.; Bihlmayer, G. and Waser, R.: «Switching the electrical resistance of individual dislocations in single-crystalline $SrTiO_3$». *Nat. Mater.*, 2006, **5(4)**, pp. 312–320.

[158] Teichert, C.: «Self-organization of nanostructures in semiconductor heteroepitaxy». *Physics Reports-Review Section of Physics Letters*, 2002, **365(5-6)**, pp. 335–432.

[159] Tersoff, J. and Legoues, F. K.: «Competing Relaxation Mechanisms in Strained Layers». *Phys. Rev. Lett.*, 1994, **72(22)**, pp. 3570–3573.

[160] Thiele, C.; Dorr, K.; Bilani, O.; Rodel, J. and Schultz, L.: «Influence of strain on the magnetization and magnetoelectric effect in $La_{0.7}Sr_{0.3}MnO_3$/PMN-PT(001) (A = Sr,Ca)». *Phys. Rev. B*, 2007, **75(5)**, pp. 054408–8.
http://link.aps.org/abstract/PRB/v75/e054408

[161] Thiele, C.; Dorr, K.; Schultz, L.; Beyreuther, E. and Lin, W. M.: «Piezoelectrically induced resistance modulations in $La_{0.7}Sr_{0.3}MnO_3/Pb(Zr,Ti)O_3$ field effect devices». *Appl. Phys. Lett.*, 2005, **87(16)**, pp. 162512–3.
http://link.aip.org/link/?APL/87/162512/1

[162] TOKUNAGA, Y.; KANEKO, Y.; HE, J. P.; ARIMA, T.; SAWA, A.; FUJII, T.; KAWASAKI, M. and TOKURA, Y.: «Colossal electroresistance effect at metal electrode/ $La_{1-x}Sr_{1+x}MnO_4$ interfaces». *Appl. Phys. Lett.*, 2006, **88(22)**, p. 223507.
http://dx.doi.org/10.1063/1.2208922

[163] TOKURA, Y.: «Critical features of colossal magnetoresistive manganites». *Reports on Progress in Physics*, 2006, **69(3)**, pp. 797–851.

[164] TOKURA, Y. and TOMIOKA, Y.: «Colossal magnetoresistive manganites». *J. Mag. Mag. Mat.*, 1999, **200**, pp. 1–3.

[165] TSUI, S.; BAIKALOV, A.; CMAIDALKA, J.; SUN, Y. Y.; WANG, Y. Q.; YUE, Y. Y.; CHU, C. W.; CHEN, L. and JACOBSON, A. J.: «Field-induced resistive switching in metal-oxide interfaces». *Appl. Phys. Lett.*, 2004, **85(2)**, pp. 317–319.
http://dx.doi.org/10.1063/1.1768305

[166] URUSHIBARA, A.; MORITOMO, Y.; ARIMA, T.; ASAMITSU, A.; KIDO, G. and TOKURA, Y.: «Insulator-Metal Transition and Giant Magnetoresistance in $La_{1-x}Sr_xMnO_3$». *Phys. Rev. B*, 1995, **51(20)**, pp. 14103–14109.
http://link.aps.org/doi/10.1103/PhysRevB.51.14103

[167] VAECK, LUC VAN.; ADRIAENS, ANNEMIE. and GIJBELS, RENAAT: «Static Secondary ion mass spectrometry: (S-SIMS) Part 1. Methodology ans structural interpretation.» *Mass Spectrometry Reviews*, 199, **18**, pp. 1–47.

[168] VALENCIA, S.; GAUPP, A.; GUDAT, W.; ABAD, L.; BALCELLS, L.; CAVALLARO, A.; MARTINEZ, B. and PALOMARES, F. J.: «Mn valence instability in $La_{2/3}Ca_{1/3}MnO_3$ thin films». *Phys. Rev. B*, 2006, **73(10)**, p. 104402.

[169] VALENCIA, S.; GAUPP, A.; GUDAT, W.; ABAD, L.; BALCELLS, L. and MARTINEZ, B.: «Impact of microstructure on the Mn valence of $La_{2/3}Ca_{1/3}MnO_3$ thin films». *Phys. Rev. B*, 2007, **75(18)**, p. 184431.

[170] VAN TENDELOO, G.; LEBEDEV, O. I.; HERVIEU, M. and RAVEAU, B.: «Structure and microstructure of colossal magnetoresistant materials». *Reports on Progress in Physics*, 2004, **67(8)**, pp. 1315–1365.

[171] VAN TENDELOO, G.; LEBEDEV, O. I.; HERVIEU, M. and RAVEAU, B.: «Structure and microstructure of colossal magnetoresistant materials». *Reports on Progress in Physics*, 2004, **67(8)**, pp. 1315–1365.

[172] VENGALIS, B.; MANEIKIS, A.; ANISIMOVAS, F.; BUTKUTE, R.; DAPKUS, L. and KINDURYS, A.: «Effect of strains on electrical and optical properties of thin $La_{2/3}Ca_{1/3}MnO_3$ films». *J. Magn. Magn. Mater.*, 2000, **211(1-3)**, pp. 35–40.

[173] VENKATESAN, T.; RAJESWARI, M.; DONG, Z. W.; OGALE, S. B. and RAMESH, R.: «Manganite-based devices: opportunities, bottlenecks and challenges». *Philosophical Transactions of the Royal Society of London Series A-Mathematical Physical and Engineering Sciences*, 1998, **356(1742)**, pp. 1661–1678.

[174] VON HELMOLT, R.; WECKER, J.; HOLZAPFEL, B.; SCHULTZ, L. and SAMWER, K.: «Giant negative magnetoresistance in perovskitelike $La_{2/3}Ba_{1/3}MnO_x$ ferromagnetic films». *Phys. Rev. Lett.*, 1993, **71(14)**, p. 2331.
Http://dx.doi.org/10.1103/PhysRevLett.71.2331

[175] WALTHER, T.: «Electron energy-loss spectroscopic profiling of thin film structures: 0.39 nm line resolution and 0.04 eV precision measurement of near-edge structure shifts at interfaces». *Ultramicroscopy*, 2003, **96(3-4)**, pp. 401–411.

[176] WASER, R. and AONO, M.: «Nanoionics-based resistive switching memories». *Nat. Mater.*, 2007, **6(11)**, pp. 833–840.

[177] WILLIAMS, D. B.: *Transmission electron microscopy: a textbook for materials science*, 2009.

[178] WOLF, S. A.; AWSCHALOM, D. D.; BUHRMAN, R. A.; DAUGHTON, J. M.; VON MOLNAR, S.; ROUKES, M. L.; CHTCHELKANOVA, A. Y. and TREGER, D. M.: «Spintronics: A Spin-Based Electronics Vision for the Future». *Science*, 2001, **294(5546)**, pp. 1488–1495.

[179] WU, J. C.; SUN, H.; DA, H. X. and LI, Z. Y.: «Study of anomalous I-V characteristics in spatially confined manganite structures». *Appl. Phys. Lett.*, 2007, **91(10)**, p. 102501.

[180] XIE, Y. W.; SUN, J. R.; WANG, D. J.; LIANG, S. and SHEN, B. G.: «Reversible electroresistance at the $Ag/La_{0.67}Sr_{0.33}MnO_3$ interface». *J. Appl. Phys.*, 2006, **100(3)**, p. 033704.

[181] YAN, L.; KONG, L. B.; YANG, T.; GOH, W. C.; TAN, C. Y.; ONG, C. K.; RAHMAN, M. A.; OSIPOWICZ, T. and REN, M. Q.: «Enhanced low field magnetoresistance of $Al_2O_3 - La_{0.7}Sr_{0.3}MnO_3$ composite thin films via a pulsed laser deposition». *J. Appl. Phys.*, 2004, **96(3)**, pp. 1568–1571.

[182] YANG, J. J.; PICKETT, M. D.; LI, X. M.; OHLBERG, D. A. A.; STEWART, D. R. and WILLIAMS, R. S.: «Memristive switching mechanism for metal/oxide/metal nanodevices». *Nat. Nanotechnol.*, 2008, **3(7)**, pp. 429–433.

[183] YOSHIDA, C.; KINOSHITA, K.; YAMASAKI, T. and SUGIYAMA, Y.: «Direct observation of oxygen movement during resistance switching in NiO/Pt film». *Appl. Phys. Lett.*, 2008, **93(4)**, p. 042106.

[184] ZENER, C.: «Interaction Between the D-Shells in the Transition Metals». *Physical Review*, 1951, **81(3)**, pp. 440–444.

[185] ZHENG, H.; WANG, J.; LOFLAND, S. E.; MA, Z.; MOHADDES-ARDABILI, L.; ZHAO, T.; SALAMANCA-RIBA, L.; SHINDE, S. R.; OGALE, S. B.; BAI, F.; VIEHLAND, D.; JIA, Y.; SCHLOM, D. G.; WUTTIG, M.; ROYTBURD, A. and RAMESH, R.: «Multiferroic $BaTiO_3 - CoFe_2O_4$ nanostructures». *Science*, 2004, **303(5658)**, pp. 661–663.

[186] ZHENG, H. M.; STRAUB, F.; ZHAN, Q.; YANG, P. L.; HSIEH, W. K.; ZAVALICHE, F.; CHU, Y. H.; DAHMEN, U. and RAMESH, R.: «Self-assembled growth of $BiFeO_3 - CoFe_2O_4$ nanostructures». *Adv. Mater.*, 2006, **18(20)**, pp. 2747–2752.

[187] ZHENG, R. K.; WANG, Y.; CHAN, H. L. W.; CHOY, C. L. and LUO, H. S.: «Determination of the strain dependence of resistance in $La_{0.7}Sr_{0.3}MnO_3/PMN - PT$ using the converse piezoelectric effect». *Phys. Rev. B*, 2007, **75(21)**, pp. 212102–4.
`http://link.aps.org/abstract/PRB/v75/e212102`

[188] ZHU, Y. L.; WU, B.; MA, X. L.; LI, D. X.; LU, H. B.; CHEN, Z. H. and YANG, G. Z.: «Textured nano-agglomerates embedded in the thin film of $La_{0.8}Sr_{0.2}MnO_3$». *Appl. Phys. Lett.*, 2004, **85(16)**, pp. 3438–3440.

[189] ZHU, Y.L.; MA, X.L.; LI, D.X.; LU, H.B.; CHEN, Z.H. and YANG, G.Z.: «Highly dense and compositionally inhomogeneous nano-agglomerates in an epitaxial $La_{0.8}Sr_{0.2}MnO_3$ thin film». *J. Mater. Res.*, 2005, **20(3)**, pp. 571–579.

[190] ZIESE, M.; SEMMELHACK, H. C. and BUSCH, P.: «Sign reversal of the magnetic anisotropy in $La_{0.7}A_{0.3}MnO_3$ (A = Ca, Sr, Ba, rectangle) films». *J. Magn. Magn. Mater.*, 2002, **246(1-2)**, pp. 327–334.

Appendix A

Publications

A.1 Journal Articles

- Atomically flat MOD $La_{0.7}Sr_{0.3}MnO_3$ buffer layers for high critical current $YBa_2Cu_3O_7$ TFA films.
  Superconductor Science & Technology 20-9 S230-238 (2007)
  A. Hassini, A. Pomar, J. Gutierrez, M. Coll, N. Roma, **C. Moreno**, A. Ruyter, T. Puig and X. Obradors

- Conducting $La_{0.7}Sr_{0.3}MnO_3$-superconducting $YBa_2Cu_3O_7$ epitaxial bilayers grown by chemical solution deposition.
  Physica C-Superconductivity and its applications 460: 1357-1358 Part 2, Sep 2007
  A. Hassini, A. Pomar, **C. Moreno**, A. Ruyter, N. Roma, T. Puig and X. Obradors

- Anisotropic c-axis pinning in interfacial self-assembled nanostructured trifluoracetate-$YBa_2Cu_3O_{7-x}$ films.
  Applied Physics Letters 94(17), 172513-3 (2009)
  J. Gutierrez, T. Puig, M. Gibert, **C. Moreno**, N. Roma, A. Pomar and X. Obradors

- Relaxation of Self-nanostructured Solution Derived $La_{0.7}Sr_{0.3}MnO_3$ Films.
  Proceeding MRS Spring Meeting (2009)
  P. Abellan, F. Sandiumenge, **C. Moreno**, M. J. Casanove, T. Puig and X. Obradors

- Spontaneous Outcropping of Self-Assembled Insulating Nanodots in Solution-Derived Metallic Ferromagnetic $La_{0.7}Sr_{0.3}MnO_3$ Films.
  Advanced Functional Materials 19(13),2139-2146 (2009)
  Highlighted with a frontispiece cover
  C. Moreno, P. Abellan, A. Hassini, A. Ruyter, A.Perez del Pino, F. Sandiumenge, M.J. Casanove, J. Santiso, T. Puig and X. Obradors

- Absence of self-heated bistable resistivity in $La_{0.7}Sr_{0.3}MnO_3$ films up to high current densities.
  Physical Review B **80**, 094412 (2009)
  C. Moreno, C.Munuera, A.Perez del Pino, J. Gutiérrez, T. Puig, C.Ocal, and X. Obradors

A.2 Conference contributions

A.2.1 Oral presentations

- *Insulating nanodots in epitaxial $La_{0.7}Sr_{0.3}MnO_3$ films grown from chemical solutions*
  Red de nanoestructuración para materiales funcionales. Barcelona. Spain [23 March 07]
  C. Moreno, P. Abellán, A. Hassini, A. Ruyter, A. Pérez del Pino, F. Sandiumenge,T. Puig, X. Obradors
- *Lithography by local electrochemistry on $La_{1-x}Sr_xMnO_3$ thin films by C-AFM*
  Red de nanoestructuración a gran escala para materiales funcionales. Santiago de Compostela. [5 Feb.08]
  C. Moreno, A. Ruyter, N. Casañ, T. Puig, X. Obradors
- *Lithography on $La_{1-x}Sr_xMnO_3$ thin films by C-SFM*
  Nanoselect group meeting. Barcelona. Spain [13 May 08]
  C. Moreno, C. Munuera, T. Puig, X. Obradors and C. Ocal
- *Combined scanning probes investigation of functional oxide thin films*
  Challenges in Materials for Energy. XaRMAE. Barcelona. Spain [11-12 Dec 08]
  C. Moreno, M. Jaafar, A. Asenjo, X. Obradors and C. Ocal
- *Nanoscale Multilevel Reversible Resistive Switching in $La_{1-x}Sr_xMnO_{3-\delta}$ thin films*
  E-MRS Spring Meeting [9-10 July 09]
  C. Moreno, M. Jaafar, A. Asenjo, X. Obradors and C. Ocal
- *Nanoscale Multilevel Reversible Resistive Switching in $La_{1-x}Sr_xMnO_{3-\delta}$ thin films*
  Nanoselect Meeting. Sant Benet: Barcelona [8-12 June 09]
  C. Moreno, X. Obradors and C. Ocal
- *Multilevel resistive switching in $La_{0.7}Sr_{0.3}MnO_3$ thin films for high density non volatile memories.*
  16th International Workshop on Oxide Electronics. Tarragona. Spain [4-7 October 09]
  C. Moreno, C.Munuera, F. Kronast , S. Valencia, X. Obradors and C. Ocal

A.2.2 Posters presentations

- *$La_{0.7}Sr_{0.3}MnO_3$/$YBa_2Cu_3O_7$ multi-layers. An all chemical solution conductive architecture for coated conductors.*
  The Jan Evetts school of superconducting materials and aplications, Camerino, Italy. [17-29 July 06]
  C. Moreno, A. Hassini, A. Pomar, N. Roma, A. Ruyter, A. Perez del Piño, T. Puig and X. Obradors
- *AFM study of the nanostructure and local conductance of epitaxial $La_{0.7}Sr_{0.3}MnO_3$ thin films grown from chemical solutions*
  Nanotech Insight. Luxor. Egypt [10-17 May 07]
  C.Moreno, A. Hassini, A. Ruyter, A. Pérez del Pino, A. Pomar, P. Abellán, F. Sandiumenge, N. Romá, N. Mestres, T. Puig, X. Obradors
- *Epitaxial La_2O_3 nanodots on $La_{0.7}Sr_{0.3}MnO_3$ grown by chemical solution deposition*
  Thin Films for Novel Oxide Devices (THIOX). Sant Feliu de Guixols. Spain. [28-30 March 07]
  C. Moreno, P. Abellán, A. Hassini, A. Ruyter, A. Pérez del Pino, F. Sandiumenge,T. Puig, X. Obradors

- *Epitaxial* La_2O_3 *islands on* $La_{0.7}Sr_{0.3}MnO_3$ *: toward nanoscale control of the magnetic anisotropy.*
  E-MRS 2007 Spring Meeting, Strasbourg (France) [28 May-1 June 07]
  C.Moreno, P. Abellán, A. Hassini, A. Ruyter, A. Pérez del Pino, F. Sandiumenge,T. Puig, X. Obradors
- *Lithography by local electrochemistry on* $La_{1-x}Sr_xMnO_3$ *thin films by C-AFM*
  V Reunión del grupo especializado de física del estado sólido (GEFES). Santiago de Compostela. Spain [6-8 Feb.08]
  C.Moreno, C. Ocal, A. Ruyter, N. Casañ, T. Puig, X. Obradors
- *Local contact surface potential on switched states of* $La_{1-x}Sr_xMnO_{3-\delta}$ *thin films by scanning Kelvin probe force microscopy*
  Second Spanish Workshop on Nanolithography. Barcelona. Spain [10-13 Nov.08]
  C. Moreno, M. Jaafar, A. Asenjo, X. Obradors and C. Ocal
- *Local contact surface potential on switched states of* $La_{1-x}Sr_xMnO_{3-\delta}$ *thin films by scanning Kelvin probe force microscopy*
  Nanotech Insight. Barcelona. Spain [29 March-2 April 08]
  C. Moreno, M. Jaafar, A. Asenjo, X. Obradors and C. Ocal
- *Space resolved element-selective investigation of nanoscale resistive switch in manganite thin films*
  Nanoselect Meeting. Sant Benet: Barcelona. Spain [8-12 june 09]
  C. Moreno, S. Valencia, F. Kronast, A. Rzhevskiy, R. Ovsyannikov, J. Schlichting, H.A. Dürr, W. Eberhardt, X. Obradors and C. Ocal

Acknowledgements

A mis directores, Xavier Obradors y Carmen Ocal por haberme dado la oportunidad de llevar a cabo este trabajo de investigación en sus grupos.

A Carmenn Ocal por acogerme en co-dirección en su grupo en el ecuador de los cuatro años que comprenden esta tesis, así como el esfuerzo realizado con unos materiales tan complejos como son las manganitas.

A los miembros del tribunal, Pep Fontcuberta, Luis Hueso, Nicolás Agraït, Teresa Puig y Agustina Asenjo por su disposición para conformarlo.

A T.Puig por sus discusiones en las medidas de transporte y la guía inicial de este trabajo. Así como sus esfuerzos para coordinar e impulsar la investigación y el conocimiento científico del departamento de Materiales superconductores y nanoestructuración a gran escala.

A P.Abellán, F.Sandiumenge y M.-J. Casanove por su importante contribución en este trabajo a través de su estudio de la microscopia electrónica y técnicas relacionadas.

A A.Hassini por transferirme todo su conocimiento sobre la preparación de las láminas delgadas por métodos químicos.

A J.Gutiérrez por su inestimable ayuda con el proceso de litografía, medidas de transporte y con el maltrecho PPMS.

A J.M. Pérez por su disposición para las medidas de SQUID.

A J.Santiso y A.Crespi por su ayuda con la realización y tratamiento de datos de los mapas en el espacio recíproco obtenidos con difracción de rayos X.

A S.Valencia por su contribución con los análisis realizados con microscopía de fotoemisión de electrones en el Helmholtz-Zentrum-Berlin.

A N.Romá por la ayuda en el laboratorio para sintetizar las muestras.

A A.Ruyter (LEMA-Université de Tours-Francia) por la disposición prestada en la colaboración llevada a cabo tanto en Tours como en Barcelona. Merci bien.

A M.Jaafar y A.Asenjo (ICMM-CSIC) por su disponibilidad en mi estancia en Madrid y sus juicios críticos con la microscopía de fuerzas magnéticas.

A A.Pérez y M.Simón por su soporte desde el servicio de microscopias de proximidad del ICMAB.

A Alejandro Goñi, a Javier Palomares y Jordi Sort, por los esfuerzos y tiempo empleado en la caracterización usando espectroscopia Raman, fotoemisión de rayos-X y magnetoóptica de efecto Kerr, respectivamente.

Al equipo de SFM, los que siempre estarán, los que llegan y los que se han ido: Markos, Lucho, Carmen^2 y Esther.

A Robert por la ayuda en la elaboración de la portada publicada en Adv.Func.Mat.

A todos los miembros de los departamentos de Materiales superconductores y nanoestructuración a gran escala y de Materiales Nanoestructurados, así como al personal de soporte y de administración del ICMAB por su contribución clave al buen funcionamiento diario del ICMAB.

A mis compañer@s de "zulo" Patricia, Jone, Ingrid y Joffre.

To EU projects under contract No. NMP4-CT-2006-032109 (STREP "SURMOF") and (HIPERCHEM, NESPA), to the Spanish Ministery (grants No. MAT2007-62732, MAT2005-02047, NAN2004-09133-C03-01, MAT2006-26543-E, MAT2008.01022/NAN and CONSOLIDER CSD2007-00041 NANOSELECT), to the Spanish Council (CSIC mobility grants) and Generalitat de Catalunya (Pla de Recerca SGR-0029 and XaRMAE) for financial support.

A mis compañer@s y amig@s del ICMAB.

"Writing in English is the most ingenious torture ever devised for sins committed in previous lives."

James Joyce

This thesis was typeset in LaTeX